Spring 5-2016

Manipulation of Surface Plasmon Resonance in Metal and Alloy Thin Films Using Dielectric Media

Benjamin DuBray Hall
Rose-Hulman Institute of Technology

Manipulation of Surface Plasmon Resonance in Metal and Alloy Thin Films Using

Dielectric Media

A Thesis

Submitted to the Faculty

of

Rose-Hulman Institute of Technology

by

Benjamin DuBray Hall

In Partial Fulfillment of the Requirements for the Degree

of

Master of Science in Optical Engineering

May 2016

ROSE-HULMAN INSTITUTE OF TECHNOLOGY

Final Examination Report

Benjamin D. Hall

Name

Optical Engineering

Graduate Major

Thesis Title Manipulation of Surface Plasmon Resonance in Metal and Alloy Thin Films Using Dielectric

Media

DATE OF EXAM: April 29, 2016

EXAMINATION COMMITTEE:

	Thesis Advisory Committee	Department
Thesis Advisor:	Azad Siahmakoun	PHOE
	Maarij Syed	PHOE
	Daniel Morris	CHEM

PASSED ___X___   **FAILED** _____

ABSTRACT

Hall, Benjamin DuBray

M.S.O.E.

Rose-Hulman Institute of Technology

May 2016

Manipulation of Surface Plasmon Resonance in Metal and Alloy Thin Films Using Dielectric Media

Thesis Advisor: Dr. Azad Siahmakoun

Surface plasmon polaritons are coherent electron oscillations that propagate along an interface between a Drude metal and a dielectric medium. The excitation of polaritons is highly dependent on the dielectric properties of the metal, the thickness of the metal, and the optical properties of the dielectric material. First, plasmonic activity is assessed for several thicknesses of silver and nickel chromium under He-Ne incidence. Relationships between film thickness and metal dielectric function are explored in both cases. To manipulate the plasmonic activity at the silver surfaces, two methods are explored. Silver oxide was grown on the surface of the silver films, and the resulting reflection curves are compared to the curves of the metal silver film alone. Next, a polymer was added to the top of the silver films, and the reflection curves were compared. Poling of the polymer is also discussed and attempted as a means of dynamically modulating the reflection curves. A weak relationship between the dielectric function of silver and the plasmonic activity was found. No definite relationship between the dielectric function of

nickel chromium and plasmonic activity was found. Both dielectric media studied were found to alter the plasmonic activity at the metal-dielectric interface.

DEDICATION

I dedicate this thesis to my parents, whose love

and support have made it possible.

ACKNOWLEDGEMENTS

TABLE OF CONTENTS

LIST OF FIGURES

v

LIST OF TABLES

LIST OF ABBREVIATIONS

PMMA	Polymethyl methacrylate
PVD	Physical Vapor Deposition
SE	Spectroscopic Ellipsometry
SP	Surface Plasmon
SPP	Surface Plasmon Polariton
SPR	Surface Plasmon Resonance

LIST OF SYMBOLS

English Symbols

A	Wave amplitude
B	Magnetic induction
c	speed of light in vacuum
D	Dielectric displacement
E	Electric field
H	Magnetic field
I	Intensity
J	Current Density
Jext	External current density
K	Plane wave vector
k_0	Propagating wave vector in vacuum
m	Mass
n	Real component of refractive index
N	Number density of charge carriers
$\tilde{n}$	Complex refractive index
P	Electric dipole moment
R	Reflectance

Greek Symbols

α	absorption coefficient
β	Propagation constant
γ	Characteristic collison frequency
Δ	Phase
ε	Relative Permittivity
$\varepsilon(\omega)$	Complex dielectric function
ε'	Real component of dielectric function
ε''	Complex component of dielectric function
ε_0	Permittivity of free space
$\varepsilon_1(\omega)$	Dielectric function of metal
$\varepsilon_2(\omega)$	Dielectric function of insulator
η	Impedence
θ_p	Plasmon angle
κ	Extinction coefficient
λ	Wavelenght in vacuum
μ	Relative Permiability
μ_0	Permiability of free space
ρ	Ellipsometric reflection ratio
ρ_{ext}	External charge density
σ	Conductivity
σ_0	DC conductivity
τ	Relaxation time

χ	Dielectric susceptibility tensor
ψ	Magnitude of ellipsometric reflection ratio
ω	Angular frequency
ω_p	Plasma frequency of free electron gas
ω_{sp}	surface plasmon frequency

1   INTRODUCTION

1.1 Background of Plasmonics

        The field of plasmonics encompasses the interaction between an electromagnetic field and free electrons in a metal. Specifically, free electrons in a conducting medium can be induced to oscillate collectively by the electric component of an impinging wave. The plasmon is described classically as an oscillation of free electron density with respect to fixed positive ions in a metal. In the presence of a uniform electric field, the electrons surrounding each positive nucleus within a bulk metal will be displaced toward one side of the core until they cancel the field inside the metal. When the electric field is removed or simply shifts, the electrons move back toward the center of the core, then to the opposing side. The electrons will oscillate until the energy is lost due to resistance or damping. The natural harmonic frequency of this oscillatory motion is known as the bulk plasma frequency, and a plasmon is a quantization of this kind of oscillation. In order to excite and sustain plasmons, an electromagnetic wave with a driving frequency at or near the plasma frequency must be coupled to the free electrons within the bulk plasma. Noble metals are often used for the excitation of surface plasmons; however, other metals and alloys including NiCr have been used [1] [2] [3].

        Surface plasmons (SPs) are coherent delocalized electron oscillations that propagate along an interface between a Drude metal and a dielectric medium [4]. Essentially, they can be thought of as a type of surface wave, which is guided along the interface. The existence of surface plasmons was first predicted in 1957 by Rufus Ritchie. Much interest was generated, and SPs were studied extensively in the 1960s and 1970s. Notably, E. Kretschmann and A. Otto developed and tested SP excitation techniques involving prism coupling [5].

In general, SPs have lower energy than bulk plasmons which quantize the longitudinal electron oscillations about positive ion cores within the bulk electron plasma. However, because they are shorter in wavelength than the incident light that excites them, SPPs have tighter spatial confinement and higher field intensity at the interface. Figure 1.1 depicts the geometry of the electric field during SPR. The charge motion in SPs generates corresponding evanescent electromagnetic fields about the interface which decay exponentially in either direction, perpendicular to the interface [6]. When taken together, the charge motion and associated electromagnetic field is called a surface plasmon polariton (SPP). Although SPPs are highly confined to the surface, the existence of the evanescent field protruding into the metal results in considerable loss along the propagation length. The exponential decay length of the evanescent fields varies in order of magnitude from tens of nanometers in metals to hundreds of nanometers in dielectric media. The specific loss along a particular interface depends on several factors, including: device material, device geometry, frequency, and the quality of the surface.
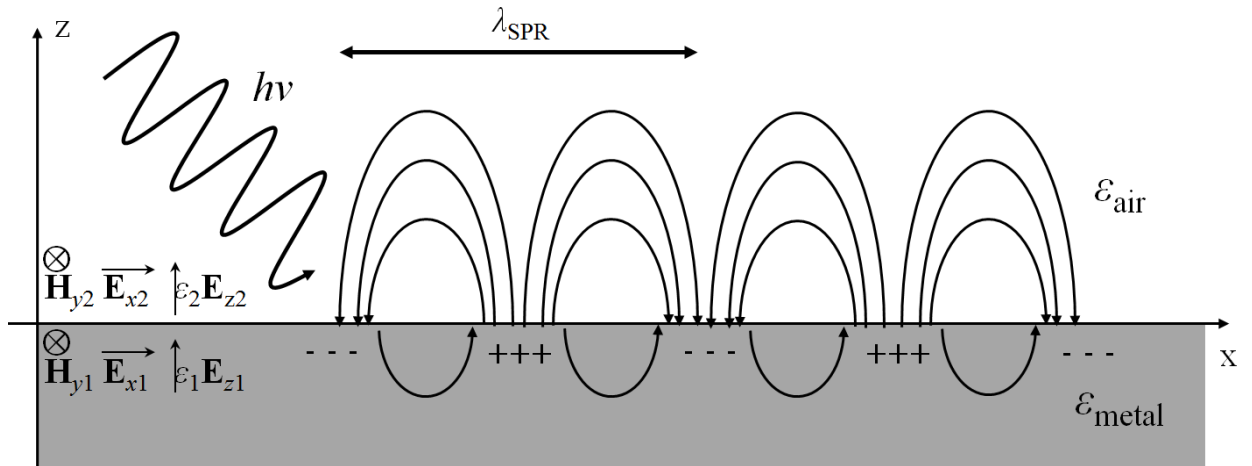
Figure 1.1: Surface Plasmon Resonance

1.2 Excitation of SPPs

SPPs propagating along an interface of a metal and a dielectric are essentially two-dimensional electromagnetic waves. Strong confinement to the interface is due to the fact that the propagation constant of the SPP is greater than the wave vector of propagating light within the dielectric medium. For this same reason, excitation of SPPs using propagating waves is impossible without implementing a phase-matching scheme [7]. Several methods have been explored to accomplish the desired phase matching between incident light and the SPP. These techniques include prism coupling, grating coupling, waveguide coupling and near-field evanescent excitation [8]. In this work, prism coupling is the preferred method for exciting SPPs.

1.3 Thesis Scope

The excitation of SPPs through prism coupling is highly dependent on the polarization of the incident wave, the dielectric properties of the metal, the thickness of the metal, the optical properties of the dielectric material, and the angle of incidence. In this work, a variety of interfaces are studied. First, plasmonic activity is assessed for several thicknesses of silver and nickel chromium under He-Ne incidence. Relationships between film thickness and metal dielectric function are explored in both cases. To alter the reflection curve of the silver surfaces, two methods were explored in which the optical properties of the external dielectric medium were altered. First, silver oxide was grown on the surface of the silver films, and the resulting reflection curves are compared to the curves of the metal silver film alone. Next, an electro-optic polymer was added to the top of the silver films, and the reflection curves were compared. Poling of the polymer is also discussed and attempted as a means of directly manipulating the reflection curves.

2   DESCRIPTION OF THE MODEL

2.1 Semi-Analytical Model

The behavior of electromagnetic fields within metallic media can, for most optical phenomena, be treated from the classical viewpoint of Maxwell's equations. The high density of free carriers within metals obviates any need to consider the discrete energy spacing of electrons within the metal. Metallic structures on the order of single nanometers can be described accurately without considering any quantum effects [9].

In treating the electromagnetic response of metals, there are three primary frequency regimes to consider. For frequencies in the infrared spectrum and the lower part of the visible spectrum, metals are highly reflective, with nearly perfect conductance. This idealized perfect conductor is suitable for most modelling purposes because only a small fraction of incident electromagnetic waves is present in the metal. Total field penetration increases markedly for frequencies in the near-infrared and visible portion of the spectrum, causing increased dissipation and limiting the scalability of some photonic devices. At ultraviolet frequencies, metals take on a dielectric character and allow the propagation of electromagnetic waves, with attenuation [10]. The complex dielectric function $\varepsilon(\omega)$ is used to describe dispersion within the metal and is sufficient in itself to describe the relevant plasmonic phenomena in this work. The strong frequency dependence of this parameter is caused by a change in the phase of the induced currents with respect to the driving field for frequencies approaching the reciprocal of the characteristic electron relaxation time τ of the metal.

The advantage of a phenomenological approach to the behavior of electromagnetics in metals is that the fundamental interactions between charged particles need not be considered. To

begin, Maxwell's equations of macroscopic electromagnetism are often written in the following form:

$$\nabla \cdot \mathbf{D} = \rho_{ext} \tag{2.1}$$

$$\nabla \cdot \mathbf{B} = 0 \tag{2.2}$$

$$\nabla \times \mathbf{E} = -\frac{\partial \mathbf{B}}{t} \tag{2.3}$$

$$\nabla \times \mathbf{H} = \mathbf{J}_{ext} + \frac{\partial \mathbf{D}}{\partial t}. \tag{2.4}$$

These four equations couple the dielectric displacement field $\mathbf{D}$, the electric field $\mathbf{E}$, the magnetic field $\mathbf{H}$, and the magnetic induction $\mathbf{B}$. External charge and current densities are also included respectively in ρ_{ext} and $\mathbf{J}_{ext}$. Further, the four macroscopic fields are linked through the polarization $\mathbf{P}$ and magnetization $\mathbf{M}$ respectively by

$$\mathbf{D} = \varepsilon_0 \mathbf{E} + \mathbf{P} \tag{2.5}$$

$$\mathbf{H} = \frac{1}{\mu_0} \mathbf{B} - \mathbf{M}. \tag{2.6}$$

Here, ε_0 is the permittivity of free space, and μ_0 is the permeability of free space. Since this work deals with nonmagnetic materials, the magnetic response $\mathbf{M}$ is ignored in favor of electric polarization effects characterized by $\mathbf{P}$. The polarization vector $\mathbf{P}$ describes the alignment of microscopic dipoles inside the material, which is termed the electric dipole moment per unit volume inside the material. Charge conservation further requires that the internal charge and current densities are linked via

$$\mathbf{J} = \frac{\partial \mathbf{P}}{\partial t}. \tag{2.7}$$

Since the materials used are limited to linear, homogenous, isotropic, and nonmagnetic media (LHI), (2.5) and (2.6) may be simplified to

$$\mathbf{D} = \varepsilon_0 \varepsilon \mathbf{E} \tag{2.8}$$

$$\mathbf{B} = \mu_0 \mu \mathbf{H} . \tag{2.9}$$

Here, ε is the relative permittivity and μ, unity in this case, is the relative permeability of the nonmagnetic medium. The linear relationship between $\mathbf{D}$ and $\mathbf{E}$ is also often defined using the dielectric susceptibility tensor χ, which describes the linear relationship between $\mathbf{P}$ and $\mathbf{E}$ as

$$\mathbf{P} = \varepsilon_0 \chi \mathbf{E} . \tag{2.10}$$

However, in isotropic media χ is symmetric and can be treated as a scalar in this work. The constitutive relations (2.8) and (2.9) are also related to each other through the material impedance given by

$$\eta = \sqrt{\frac{\mu_0 \mu_r}{\varepsilon_0 \varepsilon_r}} . \tag{2.11}$$

Finally, a constitutive relationship between internal current density $\mathbf{J}$ and the electric field $\mathbf{E}$, can be defined through the conductivity σ to be

$$\mathbf{J} = \sigma \mathbf{E} . \tag{2.12}$$

Ultimately, σ and the imaginary portion of ε carry identical information, and the preference for one over the other is largely due to historical perspective [11] [12]. Specifically, at low frequencies, preference is given to conductivity, while observations at optical frequencies are generally expressed in terms of the dielectric constant. When considering temporal or spatial dispersion, (2.8), and (2.12) must be generalized to

$$\mathbf{D}(\mathbf{r},t) = \varepsilon_0 \int dt' \mathbf{dr}' \varepsilon(\mathbf{r} - \mathbf{r}', t - t')\mathbf{E}(\mathbf{r}',t') \tag{2.13}$$

$$\mathbf{J}(\mathbf{r},t) = \int dt' \mathbf{dr}' \sigma(\mathbf{r} - \mathbf{r}', t - t')\mathbf{E}(\mathbf{r}',t'). \tag{2.14}$$

Here, $\varepsilon_0\varepsilon$ and σ describe the impulse response of the respective linear relationship. The critical assumption here is that all length scales are significantly larger than the lattice spacing of the material, ensuring homogeneity. Consequently, the impulse response functions are independent of any absolute spatial or temporal coordinates. Equations (2.13) and (2.14) can be simplified by Fourier transform with respect to

$$\int dt \mathbf{dr} e^{i(\mathbf{K}\cdot\mathbf{r} - \omega t)}, \tag{2.15}$$

which turns the convolutions into multiplications and leading to the new constitutive relations in the Fourier domain given by

$$\mathbf{D}(\mathbf{K},\omega) = \varepsilon_0 \varepsilon(\mathbf{K},\omega)\mathbf{E}(\mathbf{K},\omega) \tag{2.16}$$

$$\mathbf{J}(\mathbf{K},\omega) = \sigma(\mathbf{K},\omega)\mathbf{E}(\mathbf{K},\omega). \tag{2.17}$$

Implementing (2.5), (2.7), and (2.17), the fundamental relationship between relative permittivity and the conductivity is apparent as

$$\varepsilon(\mathbf{K},\omega) = 1 + \frac{i\sigma(\mathbf{K},\omega)}{\varepsilon_0 \omega}. \tag{2.18}$$

The interaction of electromagnetic waves within a metallic medium, known as the dielectric response, the general form $\varepsilon(\omega,\mathbf{K})$ can be simplified to the limit of a spatially local response via $\varepsilon(\mathbf{K}{=}0,\omega) = \varepsilon(\omega)$. This simplification is valid for wavelengths in the material significantly longer than all characteristic dimensions, and the result is referred to as the dielectric function of the metal, written as

8

$$\varepsilon(\omega) = \varepsilon'(\omega) + i\varepsilon''(\omega). \tag{2.19}$$

At optical frequencies, ε can be measured experimentally through spectroscopic ellipsometry, and the complex refractive index of the medium,

$$\tilde{n} = n(\omega) + i\kappa(\omega), \tag{2.20}$$

is defined as

$$\tilde{n} = \sqrt{\varepsilon}. \tag{2.21}$$

Some useful corollaries to (2.19) (2.20) and (2.21) include:

$$\varepsilon' = n^2 - \kappa^2 \tag{2.22}$$

$$\varepsilon'' = 2m\kappa \tag{2.23}$$

$$n^2 = \frac{\varepsilon'}{2} + \frac{1}{2}\sqrt{\varepsilon'^2 + \varepsilon''^2} \tag{2.24}$$

and

$$\kappa = \frac{\varepsilon''}{2n}. \tag{2.25}$$

The extinction coefficient κ determines the degree of optical absorption of electromagnetic waves in the medium. It is linked to the absorption coefficient α, by

$$\alpha(\omega) = \frac{2\kappa(\omega)\omega}{c}. \tag{2.26}$$

In turn, the absorption coefficient can be used to describe the attenuated intensity of a propagating beam through Beer's Law by,

$$I(x) = I_0 e^{-\alpha x} \tag{2.27}$$

Therefore, the real part n of the refractive index, which characterizes changes in phase velocity within the material, is primarily determined by ε' when $|\varepsilon'| >> |\varepsilon''|$. The absorption within the medium is determined by ε''.

2.2 The Dielectric Function of the Free Electron Gas

In the classical approach, a metal substrate can be treated as a gas or plasma of free electrons around a fixed lattice of positive ion cores. This approach is often called the plasma model for alkali metals, and is useful throughout the visible range into the ultraviolet range. However, the validity of this approach is limited at higher frequencies for noble metals due to the prevalence of interband transitions. The model is a mechanical one in which electrons of effective optical mass m oscillate in response to the applied electromagnetic fields, and their motion is damped by collisions with a characteristic frequency $\gamma = \dfrac{1}{\tau}$, where τ is the relaxation time of the free electron gas. The basic equation describing the motion of a single electron in a plasma sea under the influence of an external electric field **E** is

$$m\ddot{x} + m\gamma\dot{x} = -e\mathbf{E}. \qquad (2.28)$$

Assuming harmonic time dependence of the applied field, a particular solution of this equation is.

$$x(t) = \frac{e}{m(\omega^2 + i\gamma\omega)}\mathbf{E}(t). \qquad (2.29)$$

The displaced electrons give a macroscopic polarization P, which can be written as

$$\mathbf{P} = -\frac{ne^2}{m(\omega^2 + i\gamma\omega)}\mathbf{E}. \qquad (2.30)$$

After incorporating (2.30) into (2.5).the updated constitutive relation for the electric field becomes,

$$\mathbf{D} = \varepsilon_0 \left(1 - \frac{\omega_p^2}{\omega^2 + i\gamma\omega} \right) \mathbf{E} .$$

(2.31)

Here the plasmon frequency of the electron gas is determined by

$$\omega_p^2 = \frac{Ne^2}{\varepsilon_0 m},$$

(2.32)

where N is the number density of free electrons within the medium. From here, (2.19) is realized as

$$\varepsilon(\omega) = 1 - \frac{\omega_p^2}{\omega^2 + i\gamma\omega} .$$

(2.33)

Similarly, the components of (2.19) can be rewritten as

$$\varepsilon'(\omega) = 1 - \frac{\omega_p^2 \tau^2}{1 + \omega^2 \tau^2}$$

(2.34)

and

$$\varepsilon''(\omega) = 1 - \frac{\omega_p^2 \tau}{\omega\left(1 + \omega^2 \tau^2\right)} .$$

(2.35)

For metals to maintain their metallic behavior the applied frequency must be below the plasmon frequency $\omega < \omega_p$. At high frequencies close to ω_p, the product $\omega\tau \gg 1$, which leads to negligible damping. Consequently, $\varepsilon(\omega)$ is dominated by its real component. So, the dielectric function of the undamped free electron plasma is taken to be

$$\varepsilon(\omega) = 1 - \frac{\omega_p^2}{\omega^2} \tag{2.36}$$

In Figure 2.1, equations (2.34) and (2.35) are plotted over a spectrum of wavelengths about the visible spectrum. In the plot, the nominal bulk plasmon frequency ω_p, given by (2.32), is demarcated by the dashed vertical line. As another point of reference, the helium-neon wavelength ($\lambda = 632.8$ nm) is marked as well. For the visualization, a rough estimate for the number density of free carriers in a Drude metal is taken to be on the order of 10^{29} m^{-3}, and the relaxation time is estimated to the order of 10^{-14} s [13]. From this plot, it is clear that more absorption loss is expected for longer wavelengths in the infrared regime, while ultraviolet waves experience values of ε'' near zero. It should be noted that ε_1 is predicted to become positive at precisely the bulk plasmon frequency and for all greater frequencies. Additionally, in the free-electron model, $\varepsilon = 1$ at $\omega \gg \omega_p$. In reality, however, noble metals will experience such a high number of interband transitions at these frequencies, that the real component of the dielectric function never actually becomes positive. These transitions will also predictably inflate the value of ε'' at optical frequencies. Specifically, silver is known to experience interband transitions throughout the visible spectrum. For the noble metals (e.g. Au, Ag, Cu), an extension to this model is required for frequencies greater than the plasmon frequency, where the response is dominated by free electrons. However, it is important to note that for other Drude metals, the real component of the dielectric function is predicted to be positive for He-Ne light. Essentially, Figure 2.1 serves as a qualitative guide for the optical properties of conductive materials. Measured data for all metal samples is expected to exhibit similar trends.
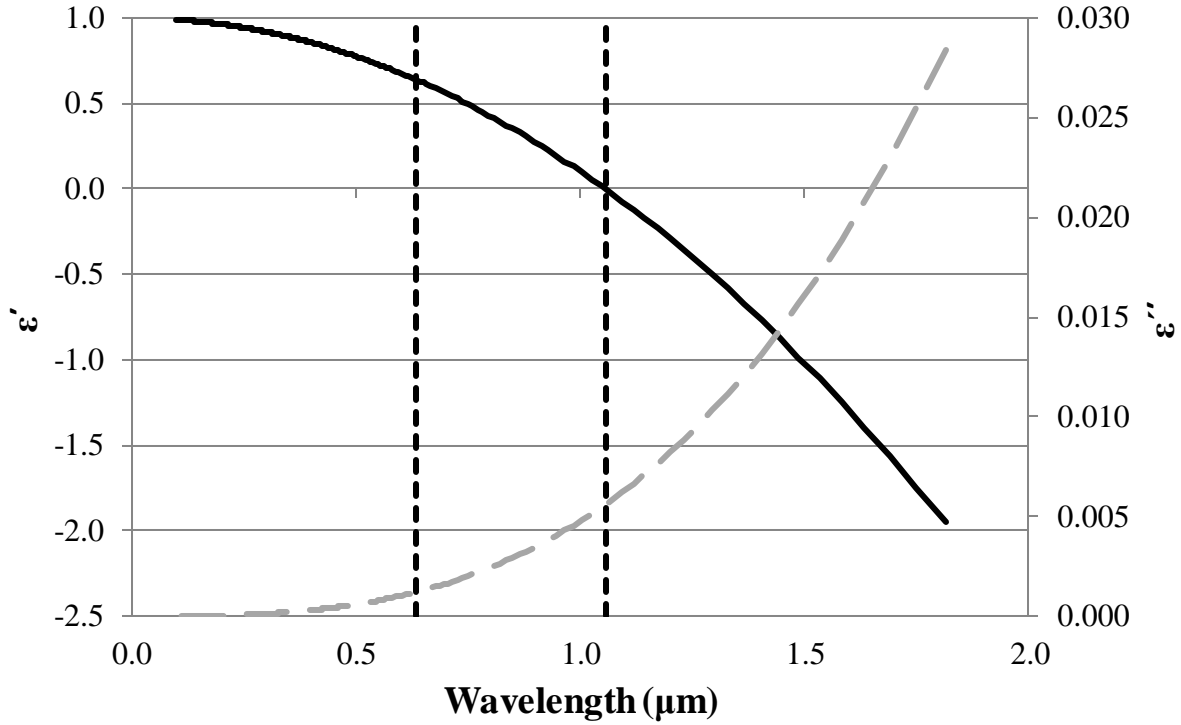
Figure 2.1: Predicted curves for the real component (black/left axis) and imaginary component (dashed/right axis) of a Drude metal

2.3 Surface Plasmon Polaritons at Metal/Dielectric Interfaces

SPPs are resonances that are excited through the coupling of electromagnetic fields to oscillations within an electron plasma cloud. These excitations occur at the interface between a dielectric and a conductor and are evanescently confined in the perpendicular direction. To treat SPPs in a classical sense, (2.1) - (2.4) are applied to a flat interface between a metal and a dielectric. In the absence of external charge and current densities, the curl equations can be combined into a wave equation given by

$$\nabla \times \nabla \times \mathbf{E} = -\mu_0 \frac{\partial^2 \mathbf{D}}{\partial t^2} \, .$$

(2.37)

In the absence of external stimuli, this can be rewritten as

$$\nabla\left(-\frac{1}{\varepsilon}\mathbf{E}\cdot\nabla\varepsilon\right)-\nabla^2\mathbf{E}=-\mu_0\varepsilon_0\varepsilon\left(\frac{\partial^2\mathbf{E}}{\partial t^2}\right). \tag{2.38}$$

For homogeneous material in which ε does not vary on the order of a the optical wavelength being considered, (2.38) simplifies to

$$\nabla^2-\frac{\varepsilon}{c}\frac{\partial^2\mathbf{E}}{\partial t^2}=0. \tag{2.39}$$

To characterize the surface plasmon response, (2.39) must be solved for each region of constant ε, and the solutions have to be matched using appropriate boundary conditions. When considering confined propagating waves, two assumptions are made to simplify the expression. First, harmonic time dependence is assumed within the electric field to give the Helmholtz equation

$$\nabla^2\mathbf{E}+k_0^2\varepsilon\mathbf{E}=0, \tag{2.40}$$

where $k_0=\dfrac{\omega}{c}$ is the wave vector of the propagating wave in a vacuum. Incorporating the propagation constant yields

$$\frac{\partial^2\mathbf{E}(z)}{\partial z^2}+\left(k_0^2\varepsilon-\beta^2\right)\mathbf{E}=0. \tag{2.41}$$

For harmonic time dependence, we arrive at the set of coupled equations (2.42)-(2.47).

$$\frac{\partial E_z}{\partial y}-\frac{\partial E_y}{\partial z}=i\omega\mu_0 H_x \tag{2.42}$$

$$\frac{\partial E_x}{\partial z}-\frac{\partial E_z}{\partial x}=i\omega\mu_0 H_y \tag{2.43}$$

$$\frac{\partial E_y}{\partial x} - \frac{\partial E_x}{\partial y} = i\omega\mu_0 H_z \tag{2.44}$$

$$\frac{\partial H_z}{\partial y} - \frac{\partial H_y}{\partial z} = -i\omega\mu_0 E_x \tag{2.45}$$

$$\frac{\partial H_x}{\partial z} - \frac{\partial H_z}{\partial x} = -i\omega\mu_0 E_y \tag{2.46}$$

$$\frac{\partial H_y}{\partial x} - \frac{\partial H_x}{\partial y} = -i\omega\mu_0 E_z \tag{2.47}$$

For propagation in the x-direction and homogeneity in the y-direction, these equations can be simplified as shown in (2.48)-(2.53).

$$\frac{\partial E_y}{\partial z} = -i\omega\mu_0 H_x \tag{2.48}$$

$$\frac{\partial E_x}{\partial z} - i\beta E_z = i\omega\mu_0 H_y \tag{2.49}$$

$$i\beta E_y = i\omega\mu_0 H_z \tag{2.50}$$

$$\frac{\partial H_y}{\partial z} = i\omega\varepsilon_0\varepsilon E_x \tag{2.51}$$

$$\frac{\partial H_x}{\partial z} - i\beta H_z = -i\omega\varepsilon_0\varepsilon E_y \tag{2.52}$$

$$i\beta H_y = -i\omega\varepsilon_0\varepsilon E_z \tag{2.53}$$

TM mode can be reduced to

$$E_x = -i\frac{1}{\omega\varepsilon_0\varepsilon}\frac{\partial H_y}{\partial z} \tag{2.54}$$

$$E_z = -\frac{\beta}{\omega\varepsilon_0\varepsilon}H_y. \tag{2.55}$$

Now the wave equation for the TM mode is given by

$$\frac{\partial^2 H_y}{\partial z^2} + \left(k_0^2 - \beta^2\right)H_y = 0.$$ (2.56)

The TE modes can be reduced to

$$H_x = i\frac{1}{\omega\mu_0}\frac{\partial E_y}{\partial z}$$ (2.57)

$$H_z = \frac{\beta}{\omega\mu_0}E_y.$$ (2.58)

And the TE wave equation is written as

$$\frac{\partial^2 E_y}{\partial z^2} + \left(k_0^2\varepsilon - \beta\right)E_y = 0.$$ (2.59)

Accommodating the geometry for SPPs can most easily be realized through a planar interface between a dielectric, non-absorbing half space with positive real dielectric constant ε_2, and a conducting region of complex dielectric character $\varepsilon_1(\omega)$. Figure 2.2 depicts the relevant geometry. The assumed quality of metallic character implies that $\text{Re}[\varepsilon_1] < 0$. This condition is met for metals under the influence of frequencies below the bulk plasmon frequency ω_p. Surface plasmon solutions will exhibit evanescent decay in the perpendicular z-direction.
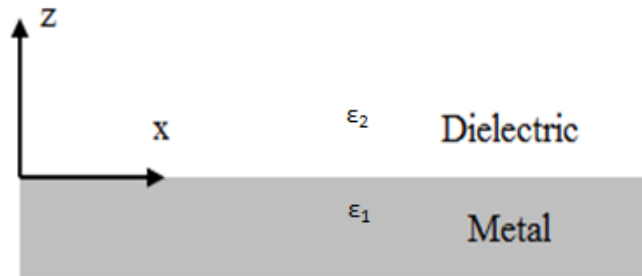
Figure 2.2: Geometry for SPP propagation at a single interface

Using the above equation set in both half spaces, the TM solutions are

$$H_y(z) = A_2 e^{i\beta x} e^{-k_2 z} \tag{2.60}$$

$$E_x(z) = iA_2 \frac{1}{\omega\varepsilon_0\varepsilon_2} k_2 e^{i\beta x} e^{-k_2 z} \tag{2.61}$$

$$E_z(z) = -A_1 \frac{\beta}{\omega\varepsilon_0\varepsilon_2} e^{i\beta x} e^{-k_2 z} \tag{2.62}$$

for $z > 0$ and

$$H_y(z) = A_1 e^{i\beta x} e^{k_1 z} \tag{2.63}$$

$$E_x(z) = -iA_1 \frac{1}{\omega\varepsilon_0\varepsilon_1} k_1 e^{i\beta x} e^{k_1 z} \tag{2.64}$$

$$E_z(z) = -A_1 \frac{\beta}{\omega\varepsilon_0\varepsilon_1} e^{i\beta x} e^{k_1 z} \tag{2.65}$$

for $z < 0$.

The condition for continuity is given by

$$\frac{k_2}{k_1} = -\frac{\varepsilon_2}{\varepsilon_1}. \tag{2.66}$$

Further, the wave vectors must maintain a relationship given by

$$k_1^2 = \beta^2 - k_0^2\varepsilon_1 \tag{2.67}$$

$$k_2^2 = \beta^2 - k_0^2\varepsilon_2. \tag{2.68}$$

This leads to the dispersion relation of the surface SPP, written as

$$\beta = k_0 \sqrt{\frac{\varepsilon_1 \varepsilon_2}{\varepsilon_1 + \varepsilon_2}} \ . \tag{2.69}$$

The TE surface modes are then written as

$$E_y(z) = A_2 e^{i\beta x} e^{-k_2 z} \tag{2.70}$$

$$H_x(x) = -iA_2 \frac{1}{\omega \mu_0} k_2 e^{i\beta x} e^{-k_2 z} \tag{2.71}$$

$$H_z(z) = A_2 \frac{\beta}{\omega \mu_0} e^{i\beta x} e^{-k_2 z} \tag{2.72}$$

for $z > 0$ and

$$E_y(z) = A_1 e^{i\beta x} e^{k_1 z} \tag{2.73}$$

$$H_x(z) = iA_1 \frac{1}{\omega \mu_0} k_1 e^{i\beta x} e^{k_1 z} \tag{2.74}$$

$$H_z(z) = A_1 \frac{\beta}{\omega \mu_0} e^{i\beta x} e^{k_1 z} \tag{2.75}$$

for $z < 0$.

Figure 2.3 shows plots of (2.69) for a Drude metal with negligible damping described by the real Drude dielectric function (2.36) for air ($\varepsilon = 1$) and fused silica ($\varepsilon = 2.25$) interface. In this plot, the frequency ω is normalized to the bulk plasma frequency ω_p, and the real component of β is plotted for both air and fused silica as solid curves. The imaginary components of β are plotted as dashed curves. Since SPPs are bound modes, excitations are expected to correspond to the portion of the dispersion curves lying to the right of the respective light lines of air and silica. Radiation into the metal occurs in the transparency regime $\omega > \omega_p$ as indicated by the portion of β

that occurs to the left of the light lines. Between the bound and radiative modes, a frequency game exists in which β is purely imaginary.

For small wave vectors corresponding to low (mid-infrared or lower) frequencies, the SPP propagation constant is close to k_0 at the light line, and waves extend over many wavelengths into the dielectric space. In the opposite regime of large wave vectors, the frequency of the SPPs approaches the characteristic surface plasmon frequency given by

$$\omega_{sp} = \frac{\omega_p}{\sqrt{1 + \varepsilon_2}} \; . \tag{2.76}$$
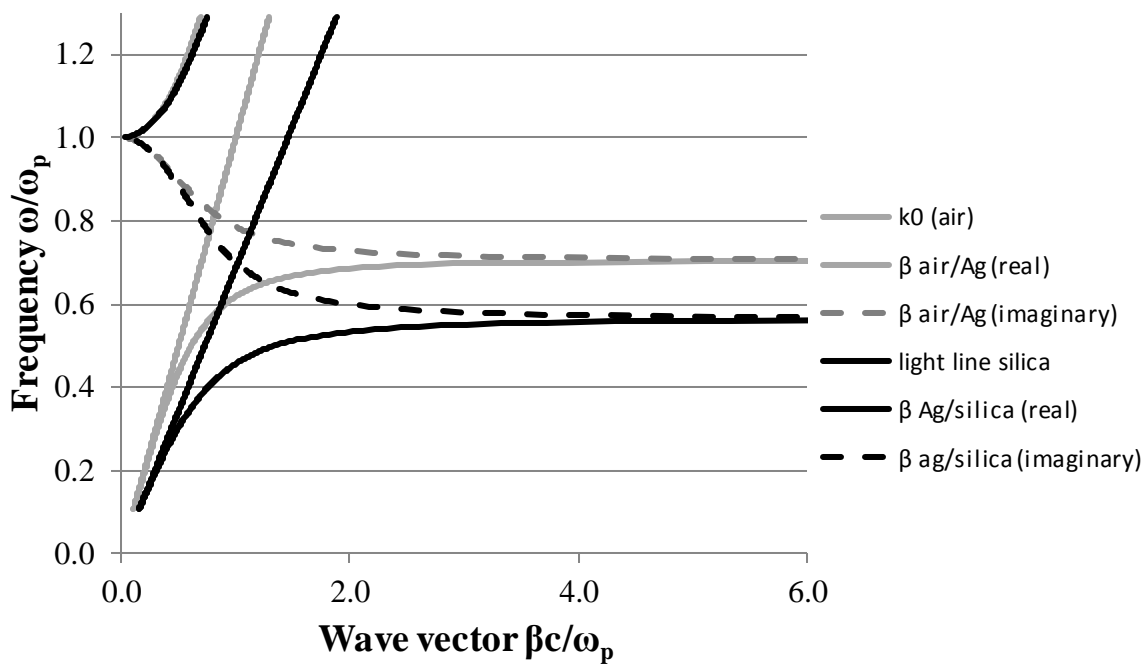
Figure 2.3: Dispesion relation of SPPs at the interface between a Drude metal with negligible colision frequency and air

2.4 Prism Coupling

In the system so far described, the momentum of an electromagnetic wave propagating in air is actually not sufficient, at any angle of incidence, to match the momentum of the SPP in a

metal. Consequently, a phase matching technique is necessary to excite the plasmon at a planar

metal/dielectric interface. This is because $\beta > k$, where k is the wave vector of light on the

dielectric side of the interface. Since there is no angle θ for which the momentum condition

$k_x = k \sin \theta$ matches or exceeds the SPP propagation constant β, even grazing incidence will not

excite SPPs. However, such phase matching can be realized in a three layer system of a thin

metal film between two dielectric media of differing dielectric constants. Typically the

surrounding medium is air, while a glass prism is used for the incident medium. When an

incident beam is reflected at the interface between the prism and the metal, the resulting in-plane

momentum is modified to $k_x = k \sqrt{\varepsilon} \sin \theta$, which is sufficient to excited SPPs with propagation

constants β between the light lines of air and the higher-index dielectric. These bound modes are

depicted to exist, for certain IR wavelengths, by the region confined by the light cone in

Figure 2.3.
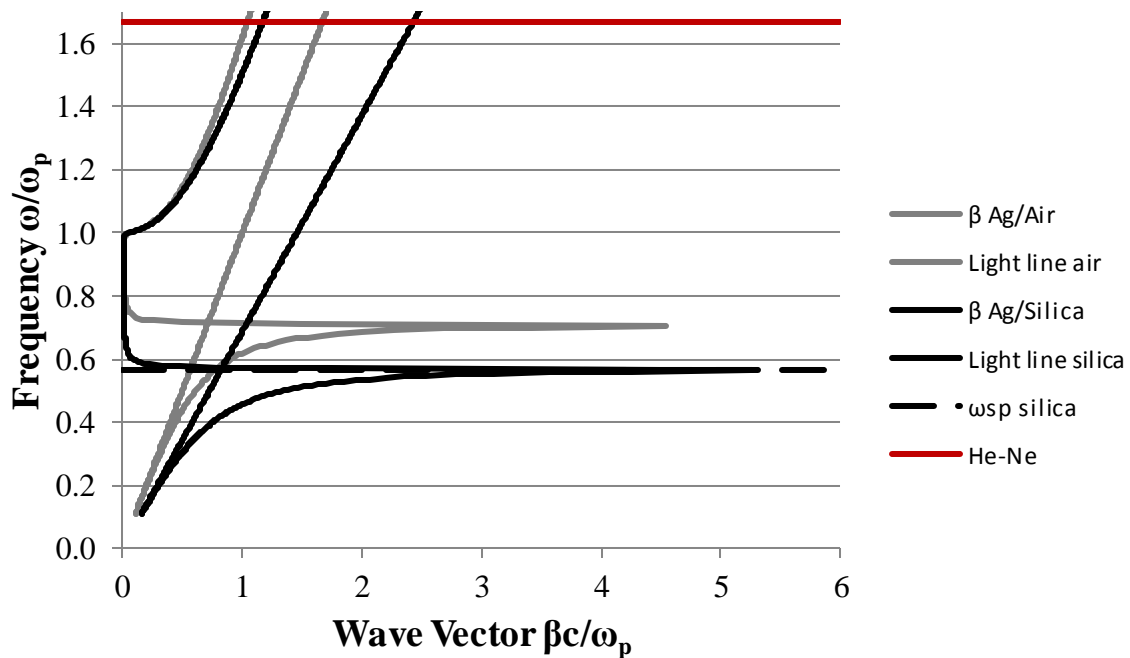
Figure 2.4: Dispersion relation

As energy is coupled from the propagating applied wave to the SPP in this process, the excitation can be observed readily as a minimum in the reflected beam intensity. This coupling scheme, which has been well documented in literature, is known as attenuated total internal reflection. Two common geometries that are used to achieve this coupling are the Kretschmann and the Otto configurations, which are illustrated in Figure 2.5. In the Kretschmann configuration, a thin film of metal is deposited onto the hypotenuse of the prism. Photons from radiation from the glass side at an angle greater than the critical angle of total internal reflection tunnel through the metal film and excite SPPs at the metal/air interface. In the Otto configuration the prism and metal are separated by an air gap, which is often desirable when measurements of surface quality are needed. In this case, total internal reflection still occurs at the prism/air interface, which excites SPPs at the metal/air interface via tunneling.
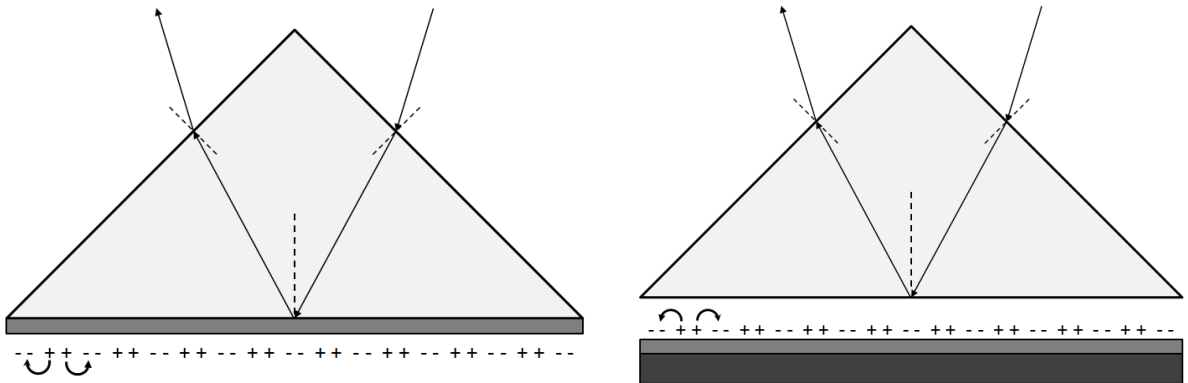
Figure 2.5: Prism coupling to SPPs using attenuated total internal reflection in the Kretschmann (left) and Otto (right) configuration.

Preliminary modelling indicated similar reflectance profiles for both geometries for the relevant materials and wavelengths to be considered. Consequently, the Kretschmann configuration was used exclusively in this work due to its relative ease and precision of

construction. In the Kretschmann geometry, the metal is in direct contact with the face of the

glass prism as shown in Figure 2.6. To describe geometry of the beam propagation within this

structure, the layers of glass, metal, and air have been labelled one, two, and three respectively.

The refractive index of glass is taken to be n(ω), while the complex dielectric function of the

metal is taken as before to be $\varepsilon_1 = \varepsilon(\omega)$.
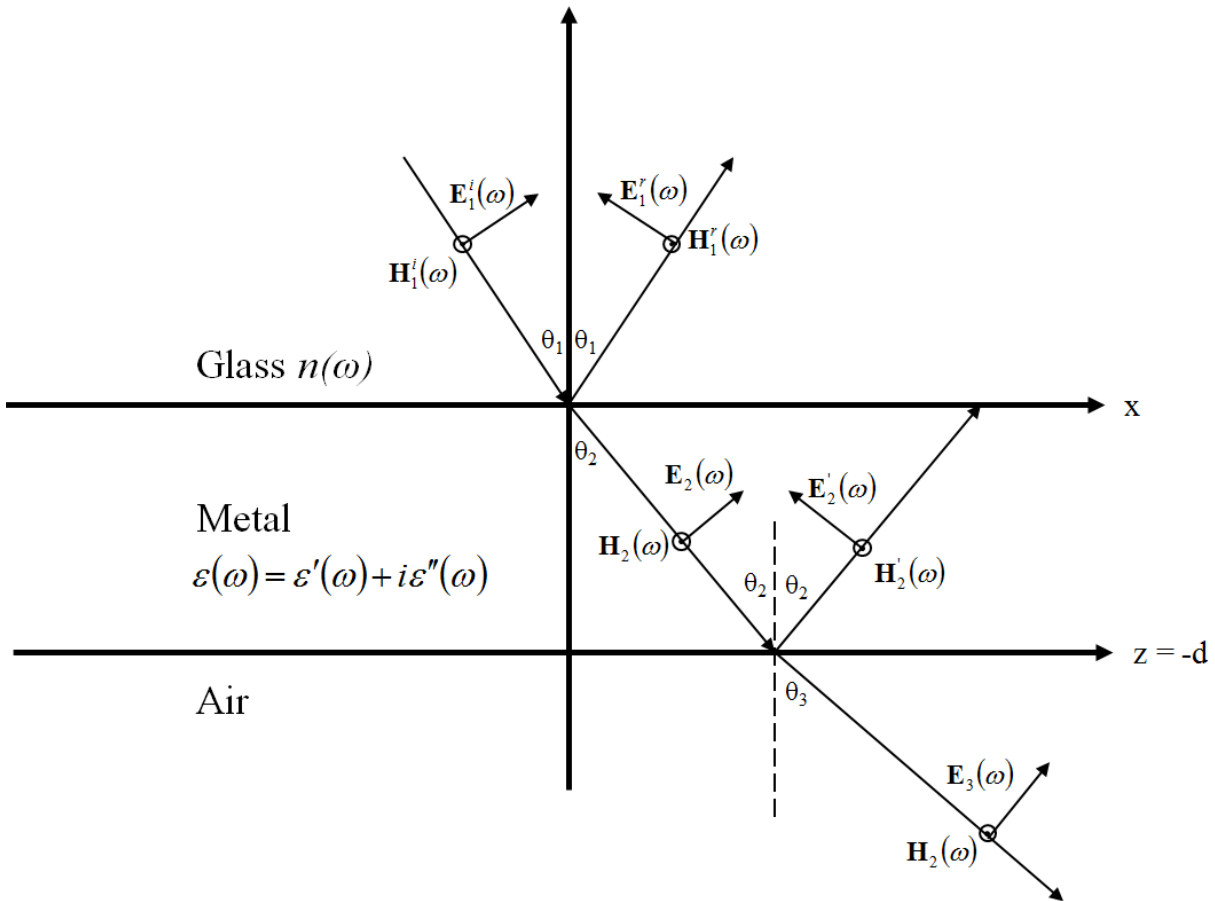
Figure 2.6: Attenuated total internal reflection geometry for a thin metal film between a glas prism and air.

In analyzing the Kretschmann configuration, (2.64) and (2.65) can be rewritten to

represent the electric field within the metal as

$$E_{metal} = E_2 e^{i\frac{\omega}{c}nx\sin\theta_1} e^{kz} + E_2' e^{i\frac{\omega}{c}nx\sin\theta_1} e^{-kz}.$$

(2.77)

Here, k is the absorption coefficient at non-normal incidence, given by,

$$k = -\frac{\omega}{c}\sqrt{\varepsilon(\omega) - n^2 \sin^2\theta_1} \, .$$

(2.78)

The unknown amplitudes can be related to the incident amplitude through the boundary

conditions. The continuity of the tangential components of **E** and **H** at the $z = 0$ and $z = -d$

boundaries gives the required equations. The amplitude of the fields in the metal at $z = 0$ are

$$E_2 = E_1^i \frac{t_{12}}{1 + r_{12}r_{23}e^{-2kd}}$$

(2.79)

and

$$E_2' = E_1^i \frac{t_{12}r_{23}e^{-2kd}}{1 + r_{12}r_{23}e^{-2kd}} \, .$$

(2.80)

The Fresnel reflection and transmission amplitude factors are given by

$$t_{12} = \frac{2n\cos\theta_1}{\varepsilon^{1/2}\cos\theta_1 + n\cos\theta_2}$$

(2.81)

$$r_{12} = \frac{\varepsilon^{1/2}\cos\theta_1 - n\cos\theta_2}{\varepsilon^{1/2}\cos\theta_1 + n\cos\theta_2}$$

(2.82)

and

$$r_{23} = \frac{\cos\theta_2 - \varepsilon^{1/2}\cos\theta_3}{\cos\theta_2 + \varepsilon^{1/2}\cos\theta_3} \, .$$

(2.83)

The angles θ_2 and θ_3 in the metal and air, respectively are defined by

$$\cos\theta_2 = \sqrt{1 - \frac{n^2 \sin^2\theta_1}{\varepsilon}}$$

(2.84)

and

$$\cos\theta_3 = \sqrt{1 - n^2 \sin^2\theta_1}\,. \tag{2.85}$$

The angles are complex values, indicating the real exponential decay of the fields in the metal and air media. Now, the ratio of the reflected optical power to the incident optical power is given by

$$R = \left|\frac{r_{12} + r_{23}e^{-2kd}}{1 + r_{12}r_{23}e^{-2kd}}\right|^2. \tag{2.86}$$

The critical factor in (2.86) is r_{23}, which can be rewritten as

$$r_{23} = \frac{\sqrt{n^2 \sin^2\theta_1 - \varepsilon} - \varepsilon\sqrt{n^2 \sin^2\theta_1 - 1}}{\sqrt{n^2 \sin^2\theta_1 - \varepsilon} + \varepsilon\sqrt{n^2 \sin^2\theta_1 - 1}}. \tag{2.87}$$

For an ideal Drude metal, the denominator of (2.87) vanishes at the plasmon angle θ_p given by,

$$n\sin\theta_p = \sqrt{\frac{\varepsilon}{(\varepsilon + 1)}} \tag{2.88}$$

Figure 2.7 shows a plot of R about θ_p for the interface between a fused silica prism of refractive index n = 1.457 and a 50 nm thick layer of metal with arbitrary dielectric function $\varepsilon(\omega) = -18.3 + 0.48$. The plasmon angle is plotted as a vertical gray line according to (2.88), and the critical angle is plotted as a dashed vertical line. The critical angle for total internal reflection for the prism in air is given by

$$\theta_c = \arcsin\left(\frac{n_{air}}{n_{prism}}\right). \tag{2.89}$$

In the plot, it is clear that the greatest contrast is achieved at or near the plasmon angle predicted by (2.88). Also the typical behavior is apparent near the critical angle for a normal interface between silica and air predicted by (2.89).
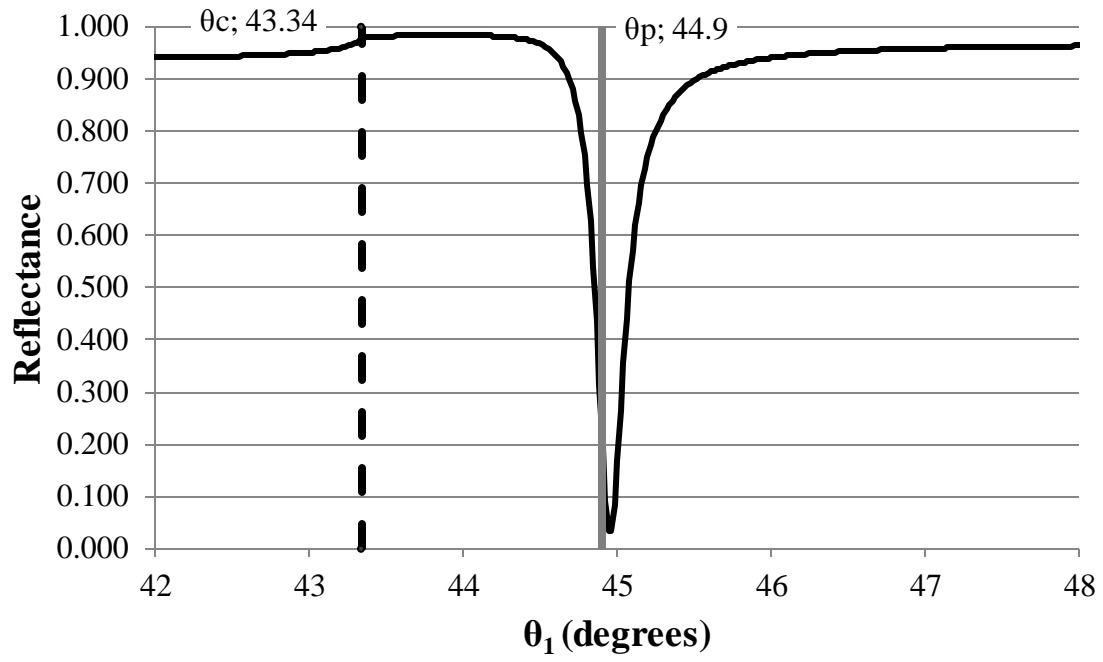
Figure 2.7: Example reflectance profile for 50 nm metal film on a fused silica prism

3   EXPERIMENT

3.1 Overview

A monochromatic, TM-polarized beam of light is directed through a triangular silica prism onto a thin film of metal. An evanescent field is generated through the reflection of the light from the prism surface that permeates the metal and the dielectric material beyond. Electron oscillations that result from this changing evanescent field result in the excitation of a surface plasmon wave between the metal and external dielectric.

3.2 Sample Preparation: Deposition of Metals and Alloys

The primary samples were prepared on triangular fused silica prisms, and the control samples were prepared in tandem on soda lime glass slides. The glass slide measured 75mm by 25 mm and 1 mm thick (Cat. No. 16004-422). The prisms, purchased from Thorlabs (PS 608), where right angle prisms of refractive index 1.457 measuring 20mm on a side. The prism surfaces were polished to $\lambda/10$ at 632.8 nm, and angle tolerances were ± 3 arcmin. Because only five prisms were used, each was initially stripped and cleaned of any prior sample residue before the fabrication process began. The principle used for determining the order of cleaning steps for a given sample was to remove the last layer applied first and then work backwards toward the first layer. When polymers were present, acetone was used to dissolve and remove any debris. In this process, an acetone bath was heated to 70° C before the prism was submerged. In order to avoid reapplication of the diluted polymer upon removal of the prism, the volume of acetone bath was many times that of the originally applied polymer. In addition, the prism was rinsed with acetone at room temperature upon removal from the bath. This was followed immediately by an ethanol rinse. To remove silver thin films, a short bath in a 1:2 nitric acid and water solution was sufficient to strip the metal from the glass. For the samples with nickel chromium

thin films, a solution of ceric ammonium nitrate in perchloric acid was needed. This solution was composed, by weight, of 10.9% ceric ammonium nitrate, 4.25% perchloric acid, and 84.85% water. Following the removal of all layers, the prisms were rinsed in deionized water and dried using pressurized nitrogen gas. To avoid damage to the prism surface, no abrasives were used at any point during the cleaning process. Control samples were prepared in tandem on soda lime glass slides. Because the control slides were used only once each, no cleaning or preparation was necessary.

Metal thin films were deposited onto the substrates via argon magnetron sputtering as shown in Figure 3.1. Ion sputtering is a physical vapor deposition (PVD) method in which gas ions, under the influence of a bias voltage, are induced to collide with a metal target. Momentum exchange between the ions and particles in the target causes material to be ejected from the target. Atoms which are expelled from the target move away in straight lines toward the substrate. Due to this kinematic nature of the material ejection, the deposition rate is highly specific to the target material. Magnetron sputtering is unique in that electric and magnetic fields are used to confine electrons in helical paths near the target metal. The result is that the gaseous ion bombardment can be sustained at relatively low temperatures and high deposition rates. In addition, this method provides better step coverage than evaporation and is thus superior for fabricating compound layers of material. For metals, a simple DC bias voltage is sufficient for sputtering, while insulating materials require RF signals in reactive gases to prevent charge buildup on the target.
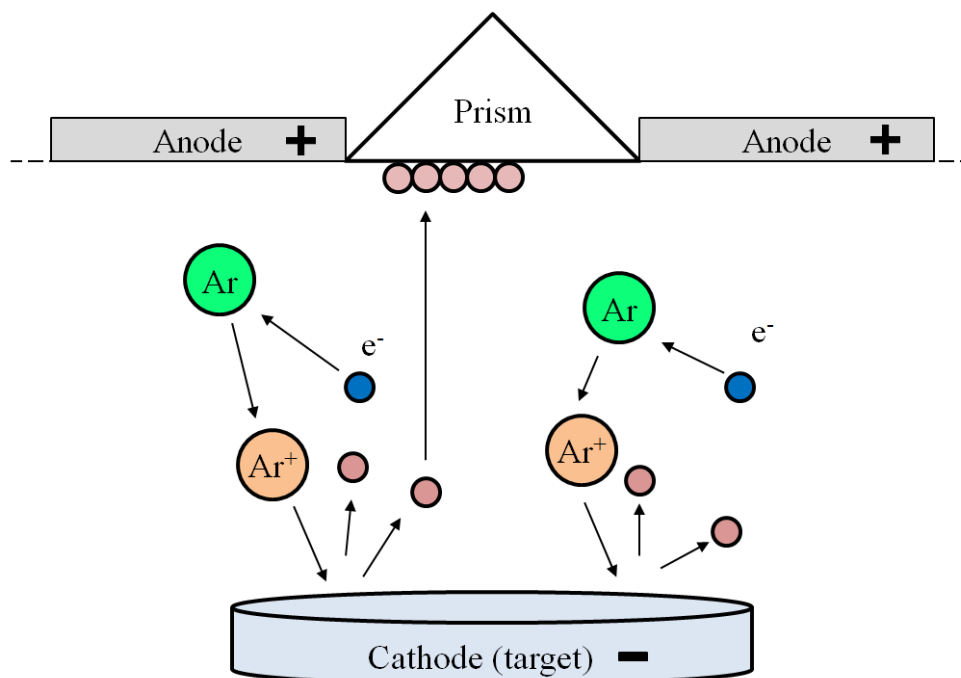
Figure 3.1: Schematic of argon ion bombardment

The sputtering system used to create the samples for this work is shown in Figure 3.2. For each trial, a single blank prism was loaded into a stage along with a corresponding control slide as shown in Figure 3.3. Then the sample was placed in the loading chamber while the system was prepared. Before introducing the argon into the sputtering system, a series of vacuum pumps were used to reduce the chamber pressure below 10 μTorr. Lower pressure between the target and substrate prevents unwanted collisions between the argon ions and ambient gas molecules, which reduces the total time of the deposition and increases the material efficiency of the target. The film thickness throughout the deposition process was nominally given by the dedicated monitoring software, which was set for each metal or alloy prior to deposition. Nominal thicknesses between 15nm and 50nm were obtained. These thicknesses, along with pressure, ambient temperature, humidity, duration, and flow rate, were recorded. The sputtering target metals used throughout the work were Ag and 80/20 NiCr alloy. The silver target was a 2.00"

diameter by 0.250" thick disk of 99.99% silver, made by Kurt J. Lesker Corb, and the second

target was an 80/20 NiCr alloy of similar specifications.
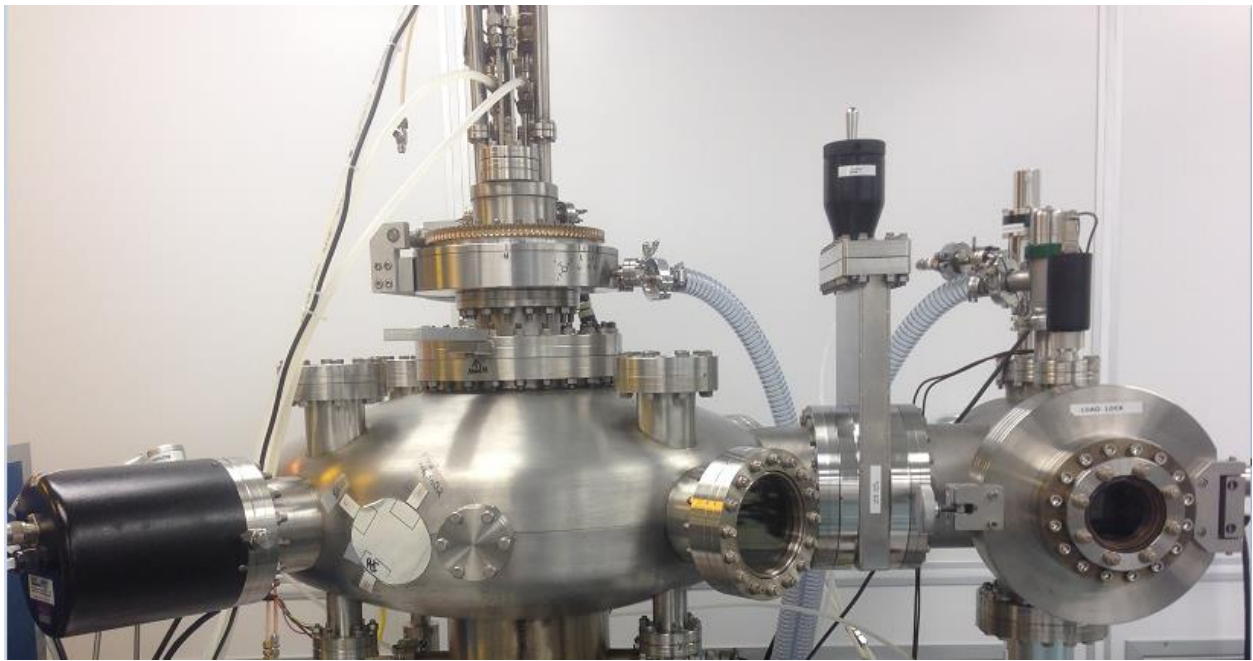
Figure 3.2: Magnetron sputtering system—Kurt J. Lesker Corp.
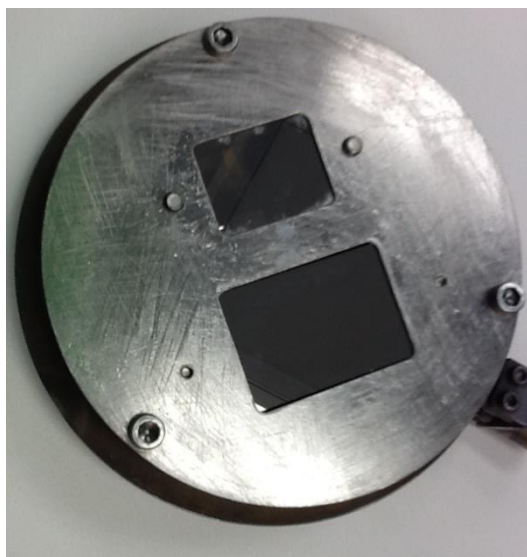
Figure 3.3: Sputtering mount with samples

Figure 3.4 shows an example of a prism and a slide sputtered with a 40nm thick layer of silver. A section of the slide was covered with thermal tape so that a profile measurement could be obtained. The silver samples were prone to oxidation, a problem which was exacerbated for thinner samples on which all of the deposited metal might be oxidized in a couple of hours. Consequently, all work on these samples was done as quickly as possible after sputtering. The NiCr samples were alternatively very stable, even over a period of months.
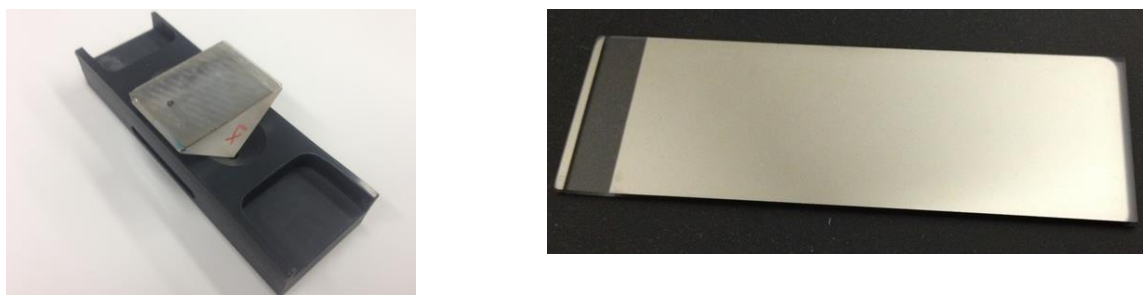
Figure 3.4: Prism sample (left) and control sample (right)

3.3 Characterization of film thickness

Several aspects of each sample were measured before any investigation of plasmonic activity. First, profile measurements were recorded for each metal sample at several points over the surface. This was done to verify that the real film thickness was within a reasonable range of the nominal thickness given by the sputtering monitor. The instrument used for thickness determination was the KLA-Tencor AlphaStep Development Series Stylus Profiler, which is capable of measuring step heights from under 10 Å to as large as 1.2 mm. Figure 3.5 depicts the instrument and its operation. The mechanism of measurement is an optical deflection height measurement device with a magneto static force control system that allows for a low force and low inertia stylus assembly. This is especially useful for measuring soft metallic films without causing damage to the surface.
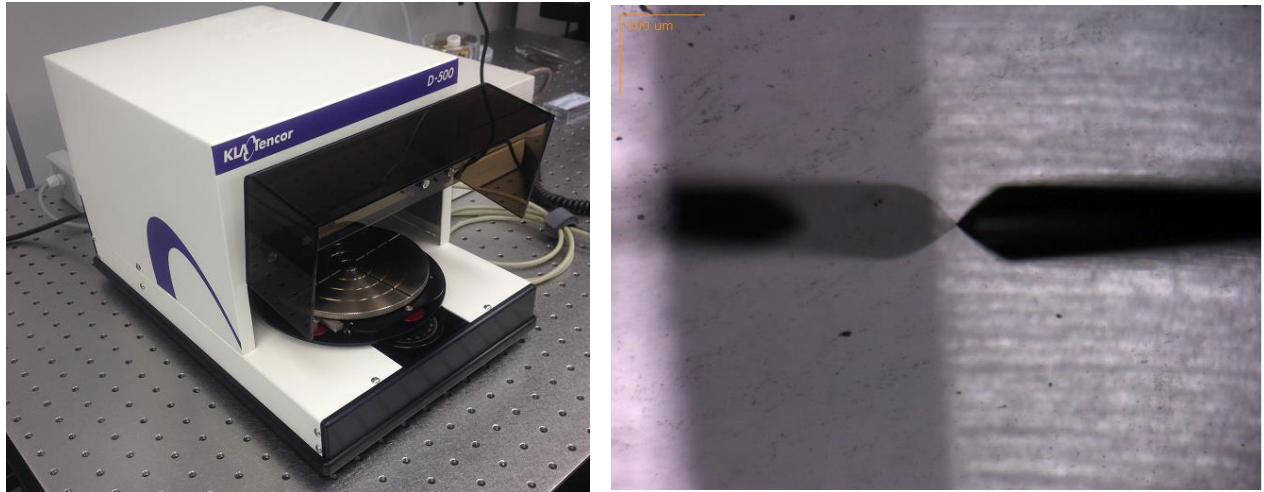
Figure 3.5: Profilometer system: Image of desktop profilometer (left) and camera image for sample measurement (right)

The software that accompanies the apparatus records both the measured step height as well as the surface roughness over the scan range. Figure 3.6 shows an example thickness measurement for a nominally 27nm thick layer of silver. In this case, two pieces of vacuum tape were placed on the slide about 0.5 cm apart to create a step during the sputtering process that would have zeroes on both sides. Ranges were selected on either side of the step to be averaged and defined as ground. The step profile is then fit by the software, and the height is displayed. A second example is shown in Figure 3.7 for a nominally 30nm thick layer of silver. For both measurements, substantial variation is present in the step surface.
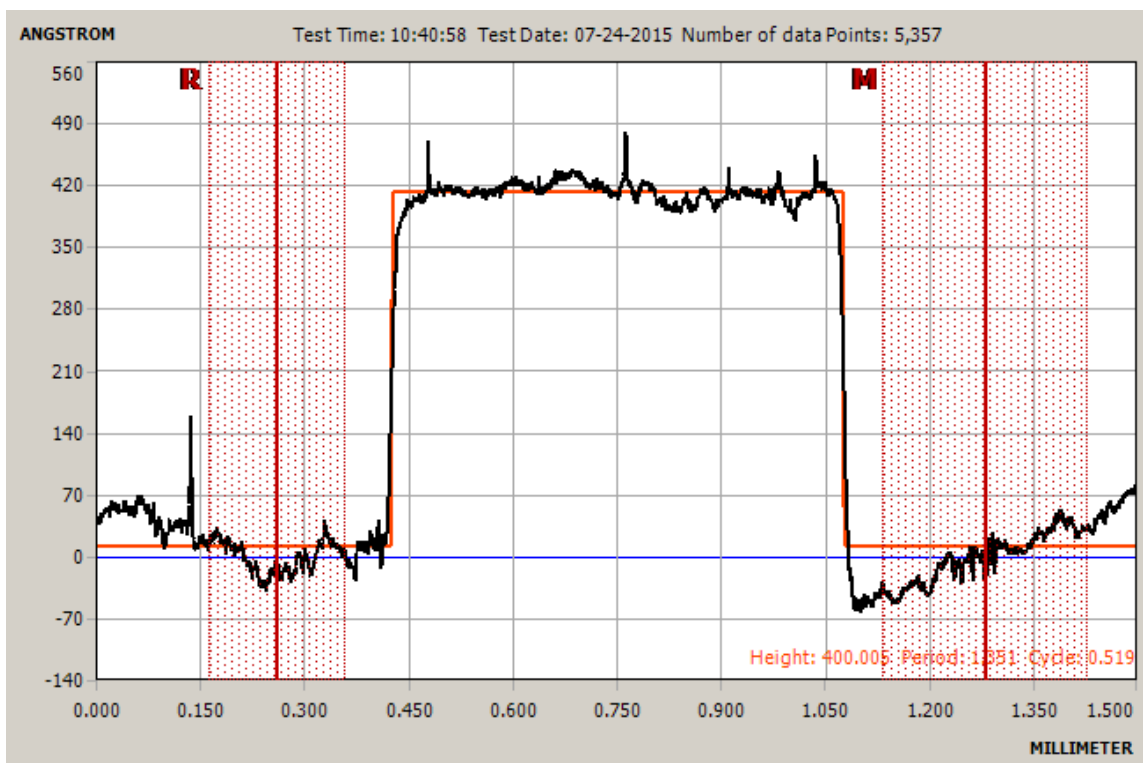
Figure 3.6: Profilometer step for a nominally 27nm thick Ag sample
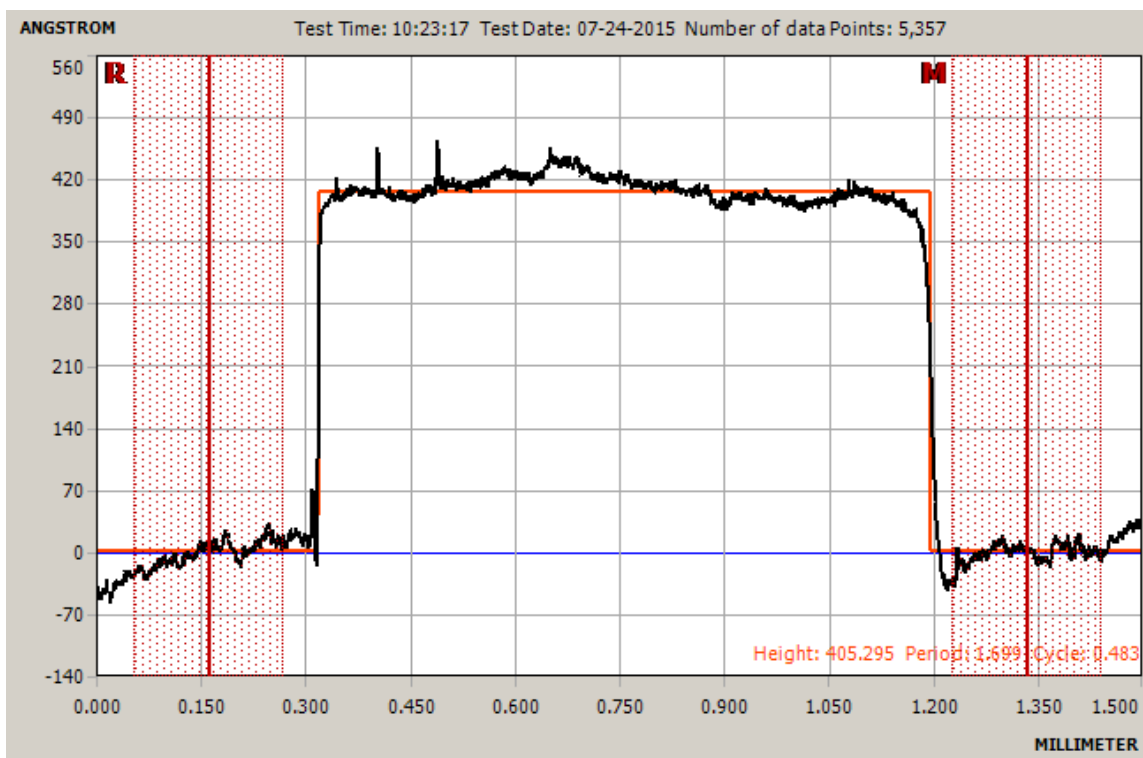
Figure 3.7: Profilometer step for a nominally 30nm thick Ag sample

In Figure 3.8, thickness measurements for various silver samples are plotted with respect to their nominal thicknesses as recorded at the time of sputtering. The specific thicknesses involved are detailed in Table 1 along with their uncertainties. The reported measurements and uncertainties each represent averages of five thicknesses measurements at different points on the sample. The reported errors are the standard errors derived from this data. Although there is some variation, the overall trend is highly linear, with measured thickness consistently about 40% larger than nominal thicknesses. This consistency helps to establish the reliability of both the sputtering system and the profilometer.
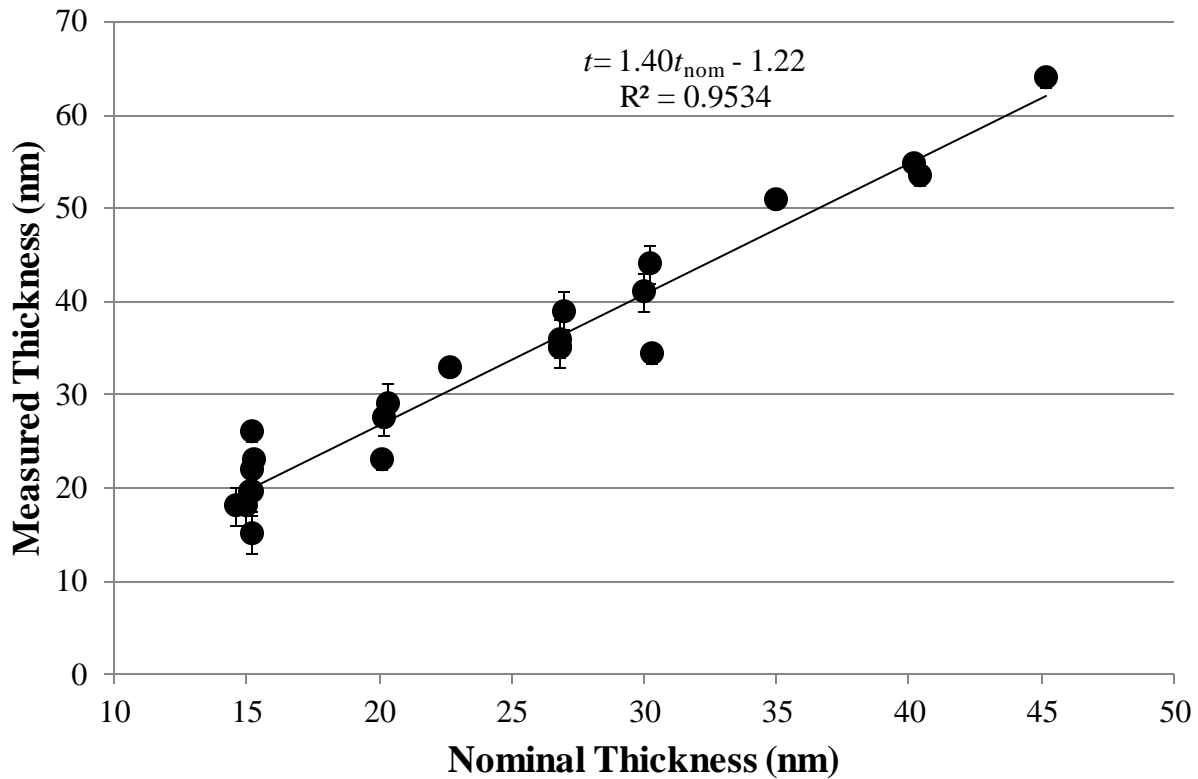
Figure 3.8: Nominal film thickness vs. measured film thickness for Ag

Table 1: Sputtering thickness accuracy measurments

nominal (nm)	measured (nm)	nominal (nm)	measured (nm)	nominal (nm)	measured (nm)
15	18 ± 2	15.3	23 ± 1	22.7	33 ± 1
14.6	18 ± 2	15.2	15 ± 2	35	51 ± 1
15.1	19.5 ± 2	20.1	23 ± 1	27	39 ± 2
15.2	19.5 ± 2	40.2	54.7 ± 1	30	41 ± 2
30.2	44 ± 2	40.4	53.4 ± 1	26.8	35 ± 2
45.2	64 ± 1	20.2	27.5 ± 2	26.8	36 ± 2
15.2	26 ± 1	30.3	34.4 ± 1	26.8	35 ± 2
15.2	22 ± 1	20.3	29.1 ± 2		

3.4 Spectroscopic Ellipsometer:

After the thickness measurement, spectroscopic ellipsometry was used to determine the dielectric function of each sample. The ellipsometric apparatus used is depicted in Figure 3.9. The ellipsometric technique is a non-destructive one in which the sample is illuminated with a beam of polarized light. The change in polarization state of the measurement beam induced by the reflection is measured as a function of wavelength.
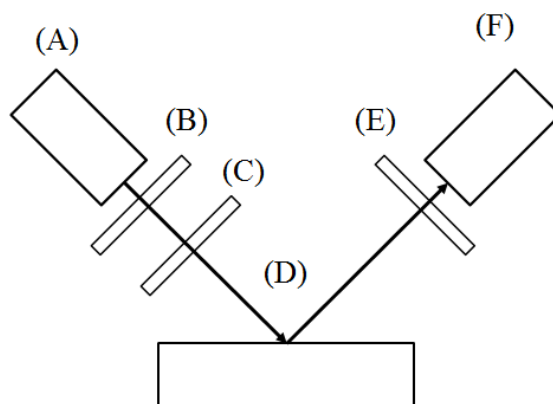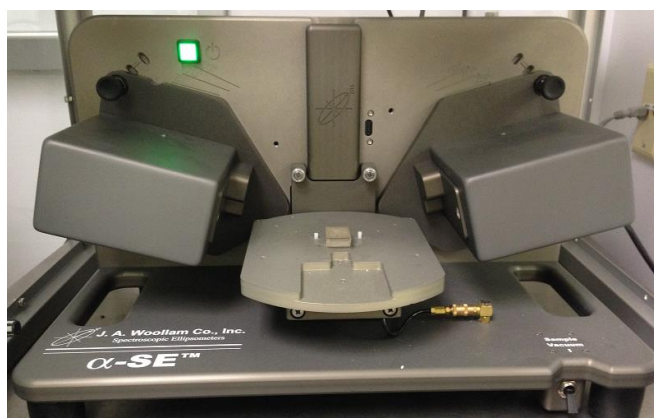
Figure 3.9 :Spectroscopic ellipsometr photo (left) and schematic (right) with components (A) light source (B) polarizer (C) wave plate (D) sample (E) analyzer (F) photodetector

The linearly polarized input beam is reflected with an elliptical polarity that is commonly characterized by the Ψ and Δ parameters as defined by

$$\tan(\Psi) \cdot e^{i\Delta} = \rho = \frac{r_p}{r_s} \ . \tag{3.1}$$

In this equation, ρ is defined as the ratio of the reflectivity for p-polarized light (r_ρ) divided by the reflectivity for s-polarized light (r_s). ρ is a complex number, and the ellipsometric parameters report this value in polar form: $\tan(\Psi)$ is the magnitude of the reflectivity ratio, and Δ is the phase term. Because the change in polarization state is defined by a ratio, ellipsometry precision is not dependent on the absolute intensity of the measurement beam [14]. Further, the ellipsometric Δ parameter is sensitive to sub-nanometer thicknesses [15]. Because this technique measures two values at each wavelength, the information gained is twice that which would be given by an intensity reflection or transmission measurement [16]. This allows for simultaneous acquisition of multiple sample parameters. With the optical properties of the substrate, and the measured thickness of the metallic film, the optical properties of the film can be obtained directly through this method.

In spectroscopic ellipsometry (SE), Ψ and Δ are acquired as a function of wavelength [17]. This information in the data determines the sample characteristics. The film thickness, film surface roughness, substrate material, substrate thickness, and optical model all need to be accounted for in the software before the software can optimize a fit for the optical properties of the film. The CompleteEASE software provided a graphical user interface for building models and displaying measured data. For a given value of ρ at a angle of incidence φ, there is an exact solution for the corresponding dielectric function of many isotropic materials given by

$$\varepsilon = \sin^2(\phi)\left\{1 + \left[\frac{1-\rho}{1+\rho}\right]^2 \tan^2(\phi)\right\}. \tag{3.2}$$

The completeEASE software allows for transformations between the raw values Δ and ψ and ε.

In Figure 3.10, a dielectric curve obtained through spectroscopic ellipsometry is shown for a sample of nominally 15nm thick silver. The real component of the dielectric function is plotted in black along the left axis, while the imaginary component is plotted in grey on the right axis. The dielectric constant at He-Ne wavelength is also denoted by the dashed black line to be $\varepsilon_{He-Ne} = -16.9 +3.3i$. The quantitative similarity to Figure 2.1 is readily apparent. Both plots depict dielectric curves of uniformly decreasing real components and of uniformly increasing imaginary components.
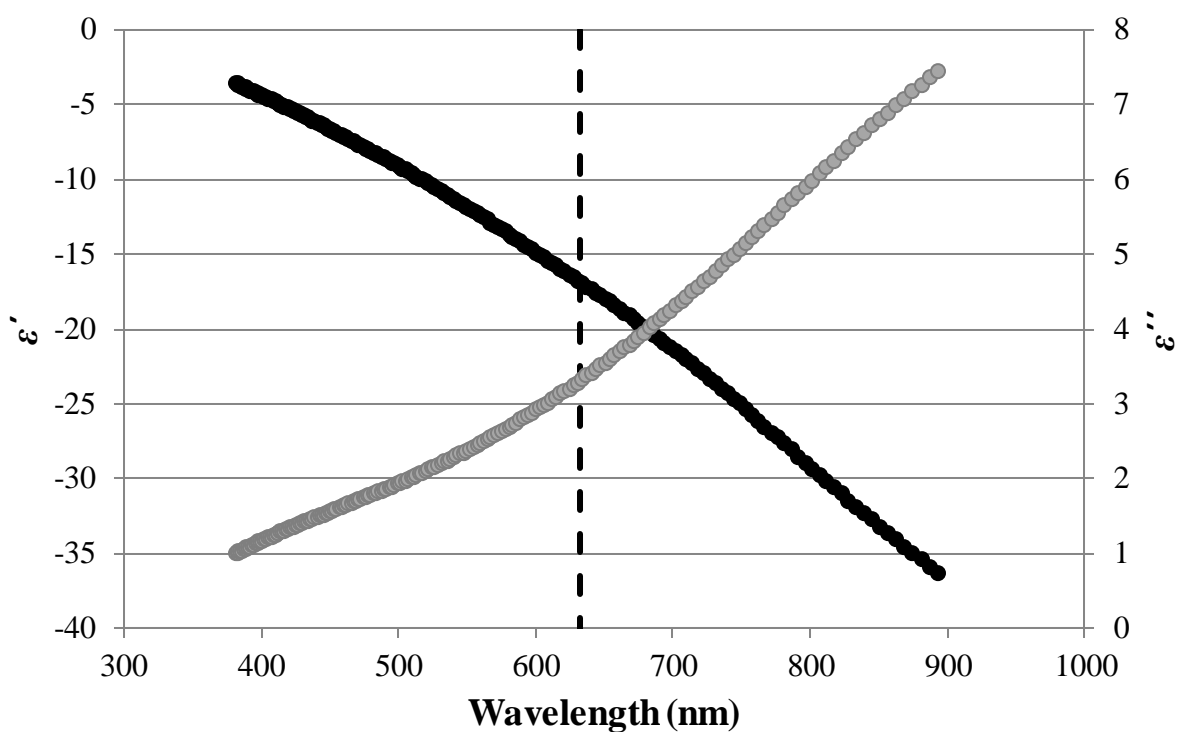
Figure 3.10: Measured curves for the real (black) and imaginary (grey) components of the dielectric function of a nominally 15nm thick Ag film

Figure 3.11 depicts a dielectric curve similar to Figure 3.10 for a sample of nominally 50nm thick silver. While the qualitative behavior of this curve is again what is expected for a highly

conductive medium, the values plotted differ. At the He-Ne wavelength, the value of this

dielectric function is $\varepsilon_{He-Ne} = -19.5 + 0.47i$.
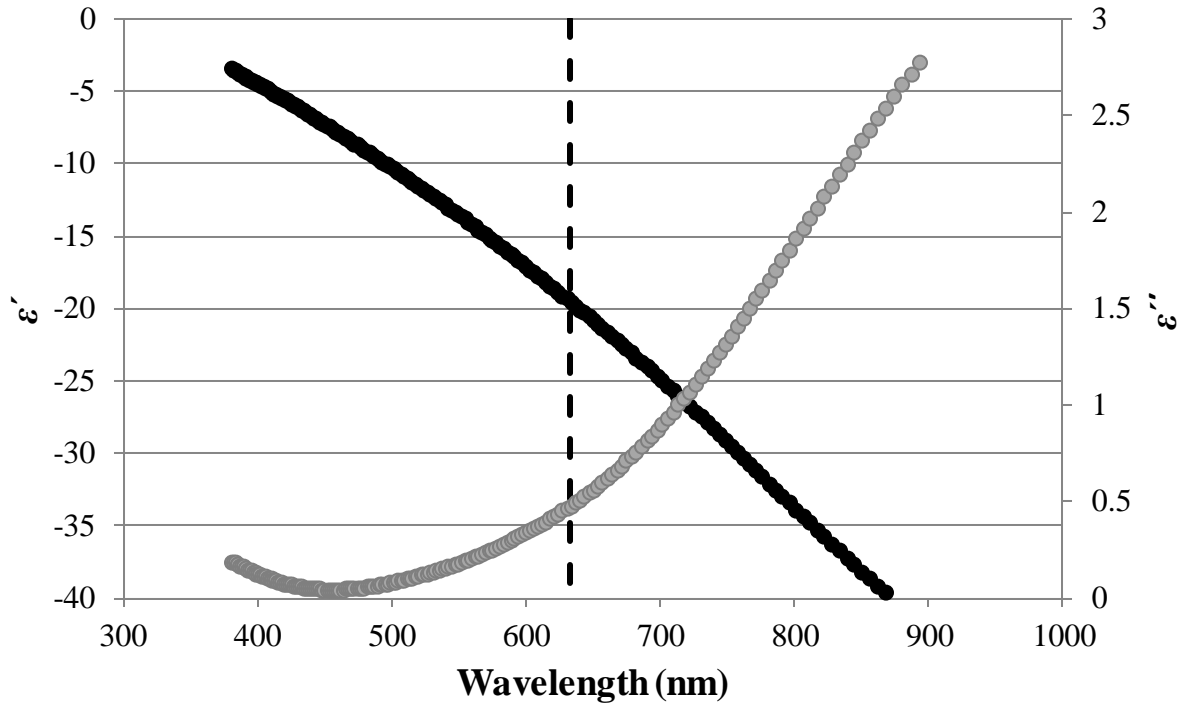
Figure 3.11: Measured curves for the real (black) and imaginary (grey) components of the dielectric function of a nominally 50nm Ag film

Table 2 details the measured dielectric constants for all silver film samples measured.

Figure 3.12 shows a plot of the real components of these dielectric constants with respect to

nominal film thickness. Here there is a clear trend toward lower dielectric values with thicker

films. Figure 3.13 shows a plot of the imaginary components of these dielectric constants with

respect to nominal film thickness. Aside from one main outlier, there is a trend shown here

toward higher dielectric values for thicker films.

Table 2: Dielectric constants for various thicknesses of silver under He-Ne incidence

Thickness (nm)	ε'	ε''
15	-16.3	0.02
15	-16.9	3.31
15.2	-18.4	0.64
23.4	-19.4	-0.04
23.5	-16.9	-0.26
23.5	-18.6	-0.11
23.9	-17.4	-0.59
24.4	-17.2	0.00
24.7	-16.8	-0.19
30	-17.9	0.60
30.2	-18.5	1.13
39.6	-19.0	-0.05
40	-19.5	0.47
45.2	-19.1	1.85
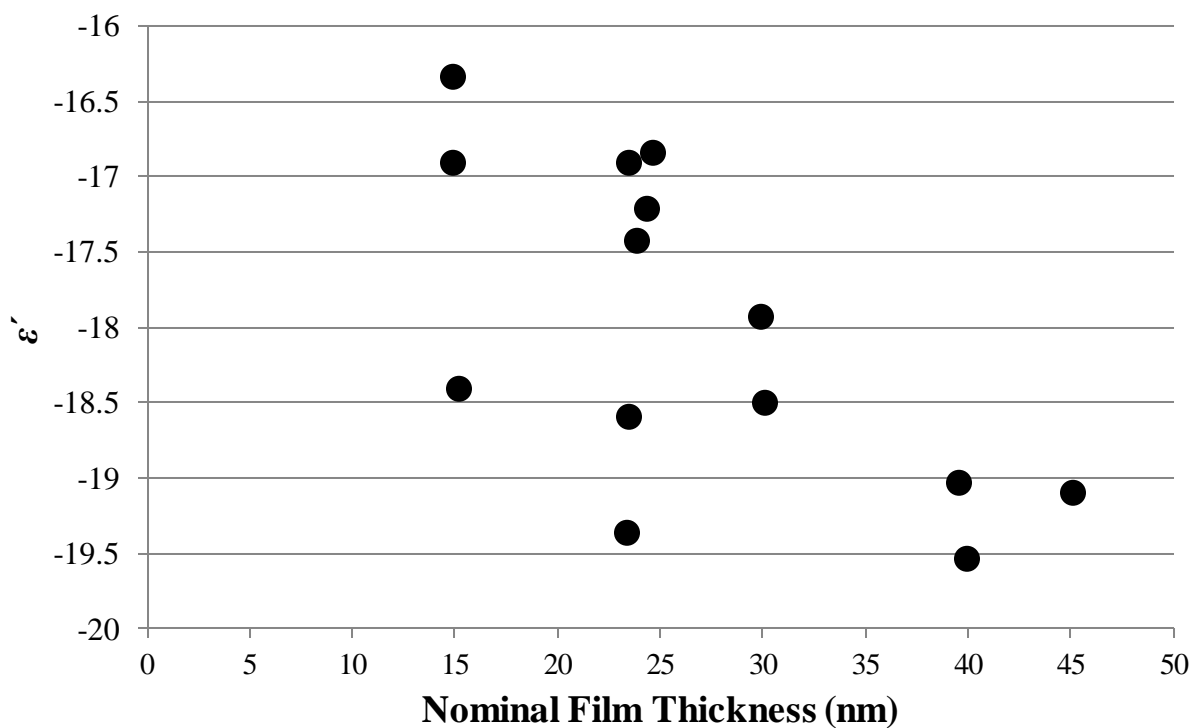
Figure 3.12: Real component of the dielectric constant for Ag at λ = 632.8 nm plotted with respect to nominal film thickness

Figure 3.13: Imaginary component of the dielectric constant for Ag at $\lambda = 632.8$ nm plotted with respect to nominal film thickness

Figure 3.14 shows a dielectric curve obtained through spectroscopic ellipsometry for a sample of nominally 18nm thick NiCr. The real component of the dielectric function is plotted in black along the left axis, while the imaginary component is plotted in grey on the right axis. Again, the dielectric constant at He-Ne wavelength is also denoted by the dashed black line to be $\varepsilon_{He\text{-}Ne} = 0.50 + 15.6i$. This plot does not behave like a Drude metal in either its qualitative properties or its qualitative properties. Both the real and imaginary components of the dielectric function increase uniformly of the working range of the ellipsometer. Figure 3.15 depicts a dielectric curve similar to Figure 3.14 for a sample of nominally 30nm thick NiCr. Again, the behavior is not what is expected for a metal. At the He-Ne wavelength, the value of this dielectric function is $\varepsilon_{He\text{-}Ne} = 2.57 + 14.86i$.
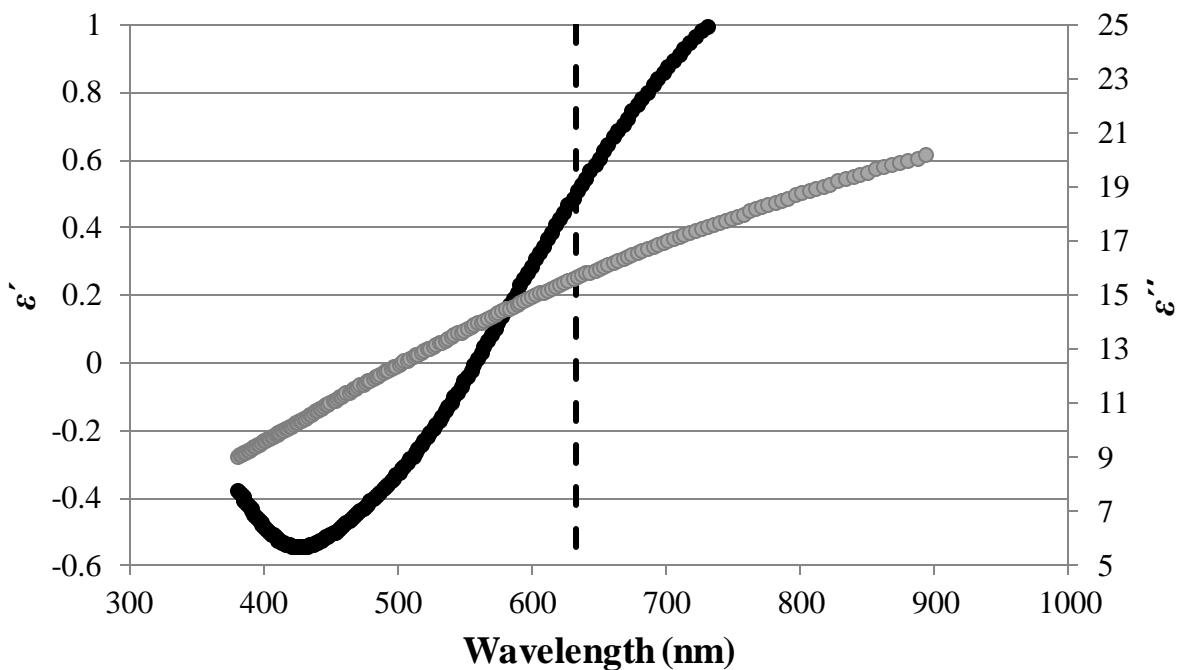
Figure 3.14: Measured curves for the real (black) and imaginary (grey) components of the dielectric function of a nominally 18nm NiCr film
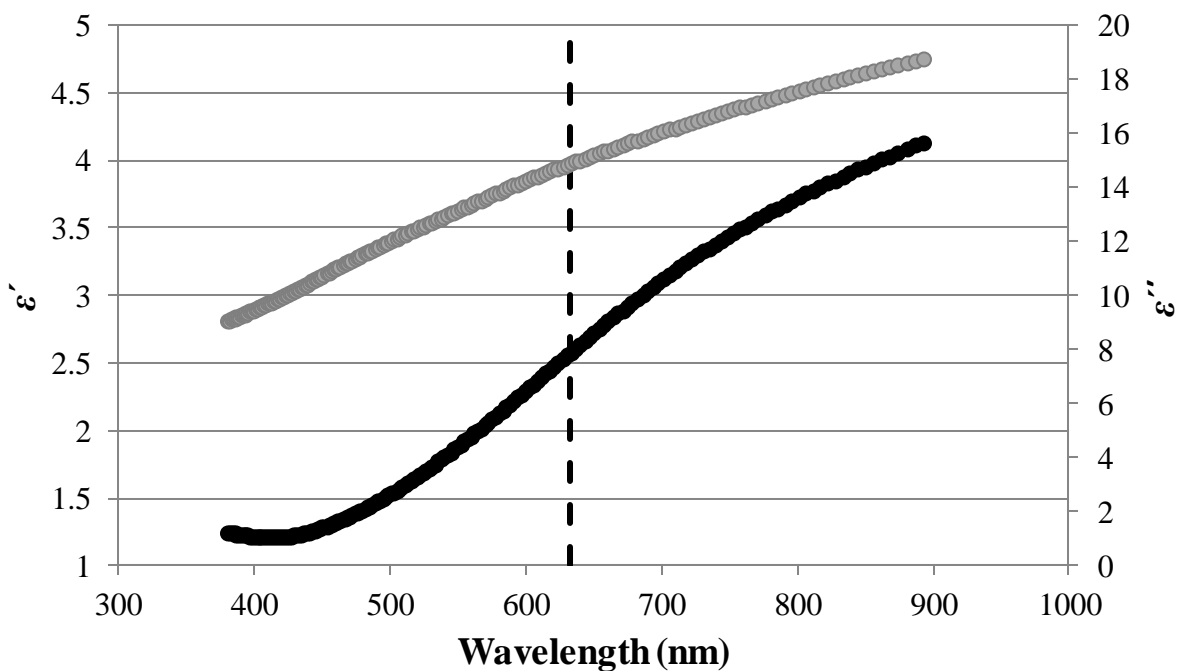
Figure 3.15: Measured curves for the real (black) and imaginary (grey) components of the dielectric function of a nominally 30nm NiCr film

Table 3 details the measured dielectric constants for all NiCr film samples measured. Figure 3.16 shows a plot of the real components of these dielectric constants with respect to the nominal film thickness. Here there is no discernable trend among the data. Figure 3.17 shows a plot of the imaginary components of these dielectric constants with respect to the nominal film thickness. Aside from one main outlier, there is a trend shown here toward higher dielectric values for thicker films.

Table 3: Dielectric constants for various thicknesses of NiCr under He-Ne incidence

Thickness (nm)	ε'	ε''
18	0.49898	15.6332
30	2.57034	14.8594
30	-1.0057	15.9456
40	0.08957	19.0559
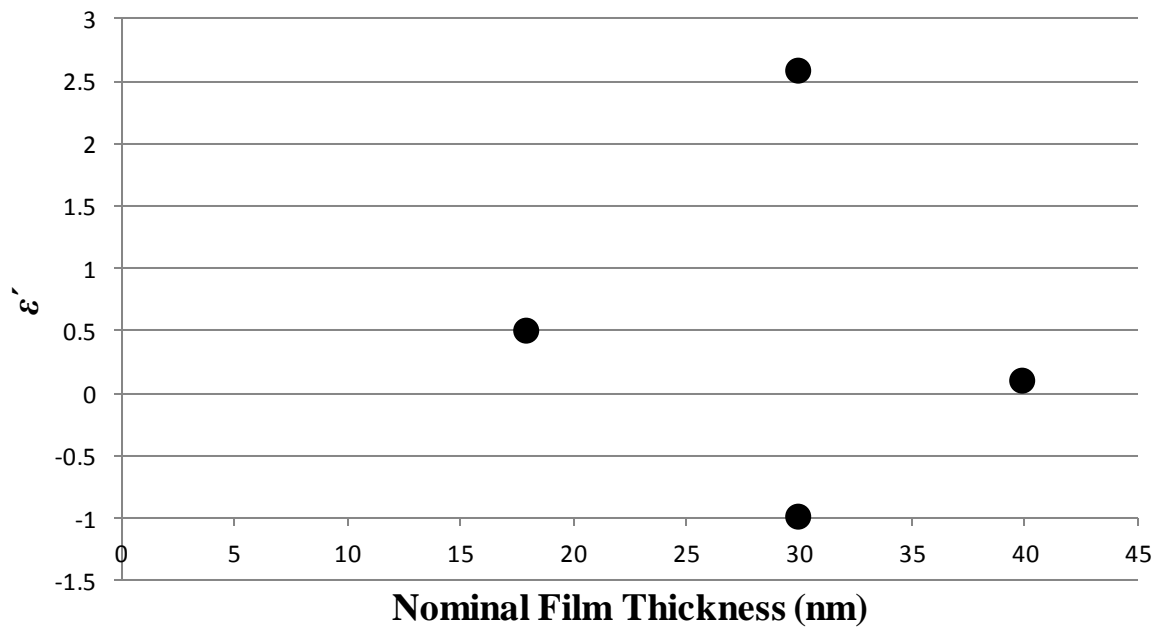
Figure 3.16: Real Component of Dielectric Function Plotted with Respect to Nominal Film Thickness of NiCr
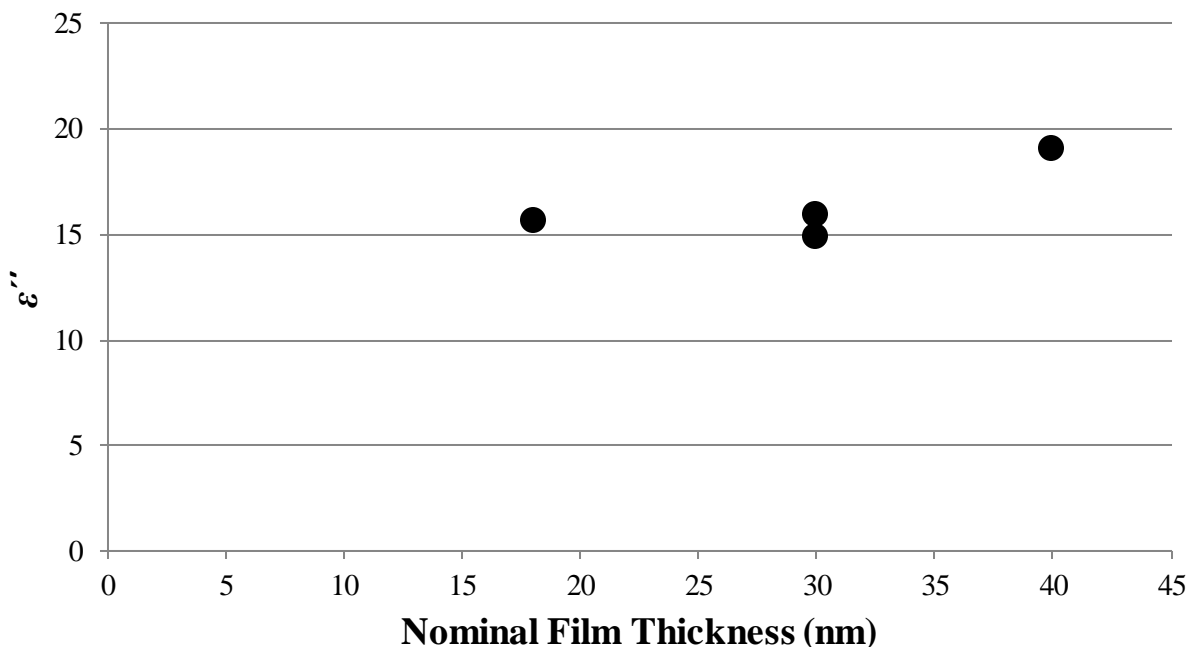
Figure 3.17:Imaginary component of dielectric function plotted with respect to nominal film thickness of NiCr

3.5Polymer Synthesis and Application

Several of the samples used included a polymer layer on top of the sputtered metal thin film. The polymers varied in concentration and preparation, but all were solutions of solid polymethyl methacrylate (PMMA) dissolved into a mixture of butanol and chlorobenzene. Additionally, an electro-optically active dye called disperse red was included in the mixture for use in poling the polymer layer later. To prepare the mixtures, solid polymer was weighed and added to measured portions of the solvents along with the dye. In order to ensure complete dissolution of the solutes, a magnetic spinner was added to the beaker and the container was gently heated while mixing for a period of one to ten hours. Prepared mixtures were reliably consistent for a period of one week.

A photoresist spinner was used to apply the polymer uniformly onto the sample surfaces. Two drops were deposited onto each sample near its center. The sample was then spun for a time

and speed respective of the viscosity of the polymer mixture used. It is important to note that the samples were not covered entirely due to the thickness unreliability that resulted from the surface tension at the edge of the samples. After being spun, the samples were placed in an oven at 90 $^{\circ}$C for an hour to set the polymer. When a third layer was needed, the sample was returned to the sputtering machine to accept more metal, and appropriate masks were added to utilize all three layers.

The SPR modulation is proposed by the introduction of an electro-optic polymer to the active silver interface. To provide the necessary bias voltage for modulation, a second layer of silver is also added over the polymer to act as an electrode. In this geometry, the base layer of silver acts both as the active plasmonic interface and as the second electrode.

The polymer chosen was a solution ranging between 2% and 6% by weight of solid polymethyl methacrylate (PMMA) in 3:7 ratio of butanol and chlorobenzene by volume. Added to the solution was a quantity of electro-optic disperse red dye. To mix the polymer, the dry components were first weighted and manually mixed separately. In a separate beaker, the butanol and chlorobenzene were measured and combined. After a brief period of stirring and resting, the solvent was heated to 60 $^{\circ}$C while a magnetic stirrer, set to low, kept the contents moving. Next, the bulk PMMA and dye were slowly incorporated into the solvent. Time was allowed for complete dissolution of the solute material before more was added. After the entire mass of solute was added to the solution, the magnetic stirrer was increased slightly, and the mixture was left covered to fully homogenize for a period of 2 hours. After the mixing period, the polymer solution was removed from heat and allowed to cool to room temperature before being bottled. Figure 3.18 shows each of these bottled solutions. For prolonged storage, a tendency was noticed

for the PMMA to fall out of solution. For this reason, the polymer was mixed in small batches that were disposed of after one week.
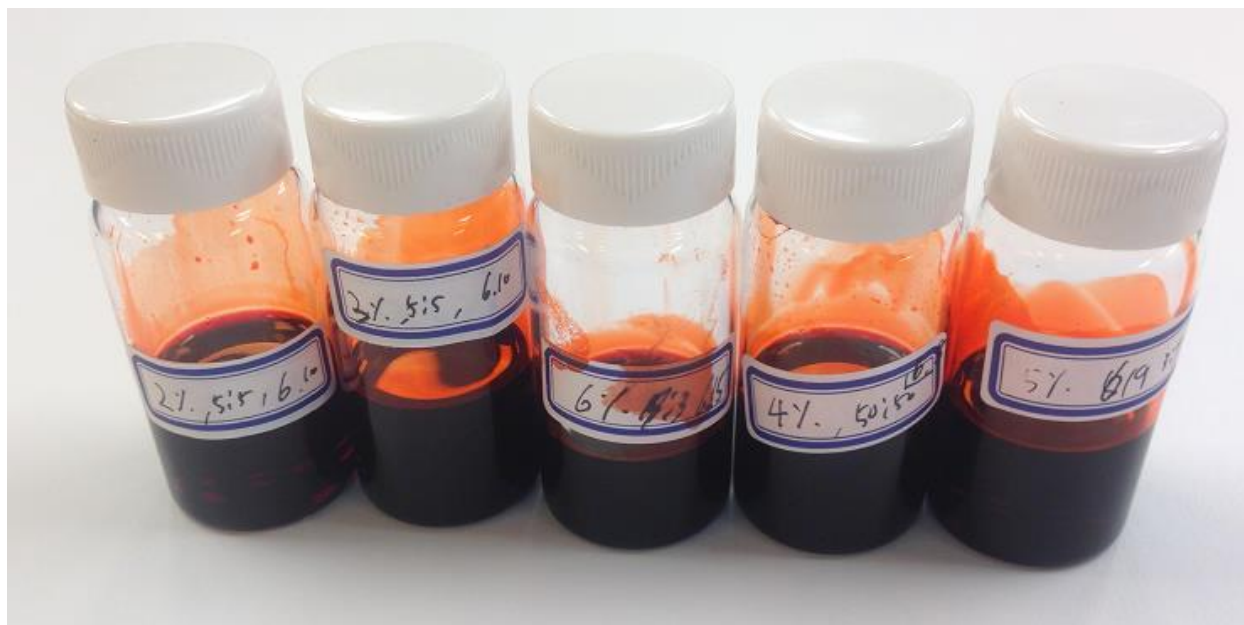
Figure 3.18: PMMA solutions used in this work

The refractive index of the mixed polymer was n = 1.489 at a wavelength of 632.8 nm. Fused silica was again used as a prism substrate. If the thickness of the initial silver layer is chosen correctly, all the incident light will again be coupled into the SPW at the resonance angle θ_{SPR}. If the angle of incidence is then fixed at θ_{SPR}, and the index of refraction of the polymer is changed by the application of a bias voltage across the silver electrodes, the light will no longer be absorbed by the SPW. Consequently, the output light that is reflected off the hypotenuse of the prism will be modulated in its intensity as the index of refraction is modulated.

The first layer of silver was determined from previous trials to be ideal at 50nm. Preliminary conductivity tests with a multimeter indicated that this thickness would be sufficient to ensure equal potential across the surface of the film once voltage was applied. The film was deposited onto the hypotenuse of the prism using argon sputtering. The PMMA solution was

then applied on top of the silver with a spin coater at 2500 rpm for 30s to yield a film of 250 nm. This thickness was chosen because it was expected to encompass the interaction depth of the evanescent tails produced upon reflection of the incident wave. A thicker film would not be expected to affect the behavior of the reflection significantly, but would require a greater bias voltage for effective poling. Figure 3.19 shows the spinning apparatus and chuck. Two layers of PMMA were used, each comprising half of the total desired thickness. This was done to reduce the risk of gaps in the layer that could potentially lead to a short.
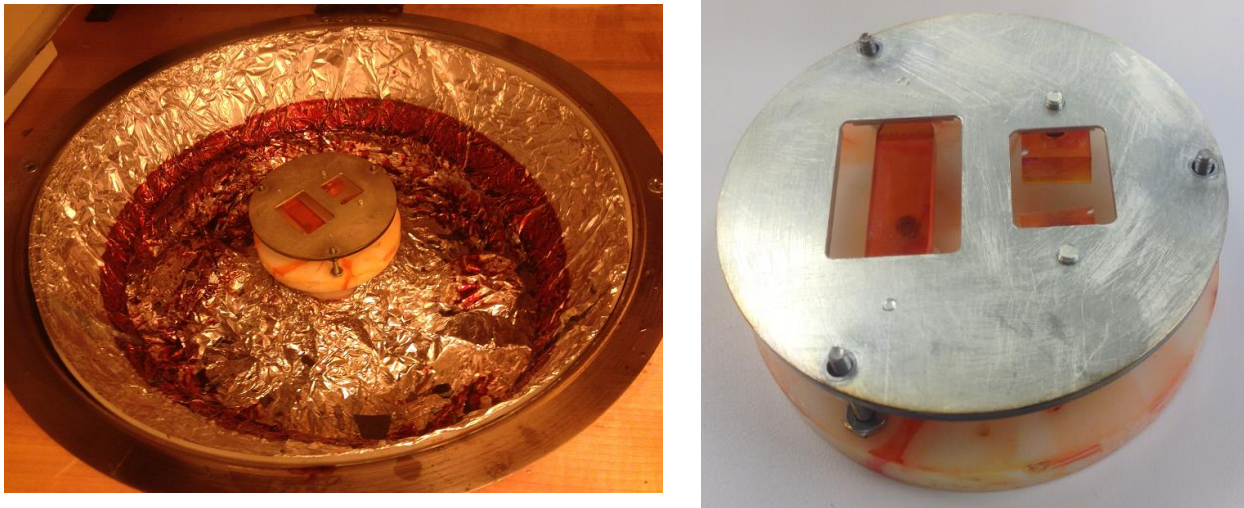
Figure 3.19: Photoresist spinning apparatus and spinning chuck with sample stage

3.6 Poling the polymer

The intended purpose for the disperse red dye in the PMMA mixture was to allow for poling to take place within the polymer under the influence of a DC bias voltage. The poling process removes the symmetric structure of the nonlinear molecules in the polymer. After the nonlinear molecules in the polymer have been aligned by the electric field, the PMMA is an

electro-optic medium. As a result, the index of refraction is expected to change when a voltage is reapplied according to

$$\Delta n = \frac{n_0^3 rE}{2}.$$

(3.3)

Here, n_0 is the index of refraction of the polymer in the absence of an applied field, r is the electro-optic coefficient, and E is the applied field. Since the PMMA lay between two layers of silver, the bias applied to the electrodes was assumed to result in an electric field that pervaded the polymer normal to the planar interface. This is because the two conductive layers should act like a capacitor since they should each be of equal potential across their entire surface. To pole the samples, an electric field of 30 V/μm was applied across the silver electrodes at a temperature of 140^0C for 5 min. The sample was then removed from the heat and allowed to cool to room temperature for a period of 30 min. During this time, the voltage was maintained to cement the molecules in their new orientation.

3.7 Oxidation of silver films

A second method for manipulating the optical properties of the dielectric potion of the plasmonic interface was oxidation of the metal film. Due to the stable nature of NiCr, this was only attempted for the silver samples. The premise here is that the oxide itself is a dielectric medium of variable thickness. The thickness of the oxide can be varied according to the oxidation temperature and duration. Oxide was grown in a conventional oven at temperatures between 150 ^{o}C and 300 ^{o}C. The oven used is shown in Figure 3.20. Given the susceptibility of silver to natural oxidation, significant films were grown over relatively short time intervals ranging from 5 min. to 45 min.

Figure 3.20: Oven used for oxidizing samples

<u>3.8Light Probe</u>

To quantify surface plasmon activity in each sample at a given angle, a linear, s-polarized light probe was introduced to one leg of the prism such that it was reflected off the hypotenuse to exit through the opposite leg. Figure 3.21 depicts the experimental setup for the light probe, and Figure 3.22 shows a close-up view of the rotation stage. The probe was a 30 mW, continuous wave, 632.8nm He-Ne laser (Melles Griot) In front of the laser, a linear polarizer was placed to ensure that the polarization of the incident beam was in the plane of incidence at the hypotenuse of the triangular prism. An additional polarization rotator was placed down axis from the linear polarizer to ensure the accuracy of the polarization. Due to the geometry of the optical table used, an adjustable mirror was placed in front of the polarization rotator to reflect the incoming wave onto the prism. This mirror served a secondary purpose of allowing for subtle adjustment of the beam onto the center of the prism. A minor inconvenience of including the mirror in the setup is that it rotates the polarization of the incoming beam by 90^0. A Newport power meter was used to measure the input intensity as well as the output intensity of the laser, and the total internal

reflection was determined using (2.87). Two linear translation motors were coupled to corresponding rotation stages, onto which were mounted the prism and the power meter in a *θ-2θ* configuration.
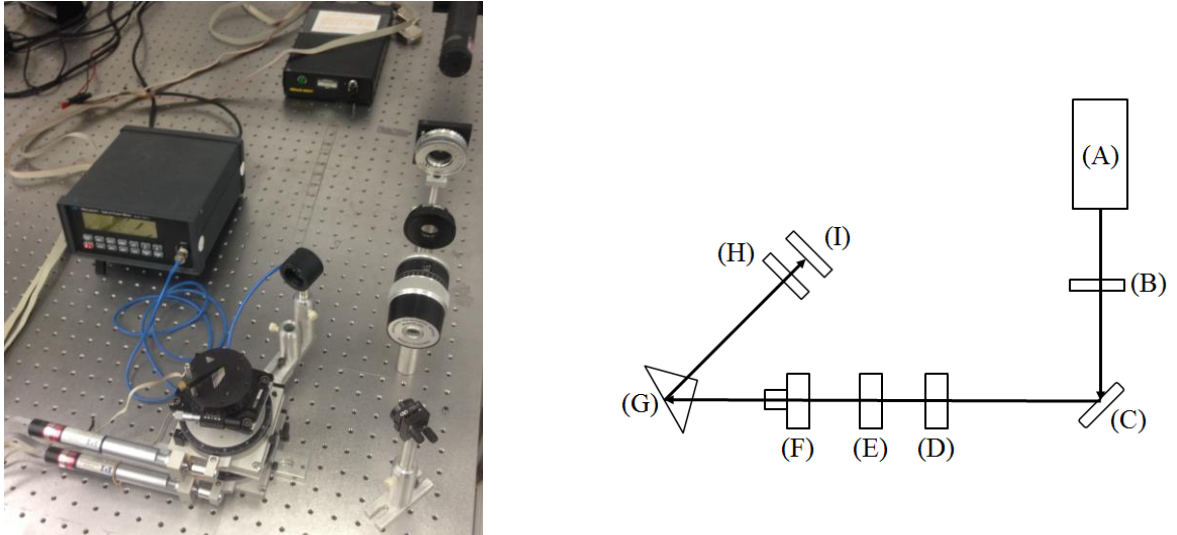
Figure 3.21: Light probe setup (left) and schematic (right) with components (A) source (B) iris (C) mirror (D) iris (E) linear polarizer (F) polarization rotator (G) coated prism on rotation state (H) iris (I) power meter
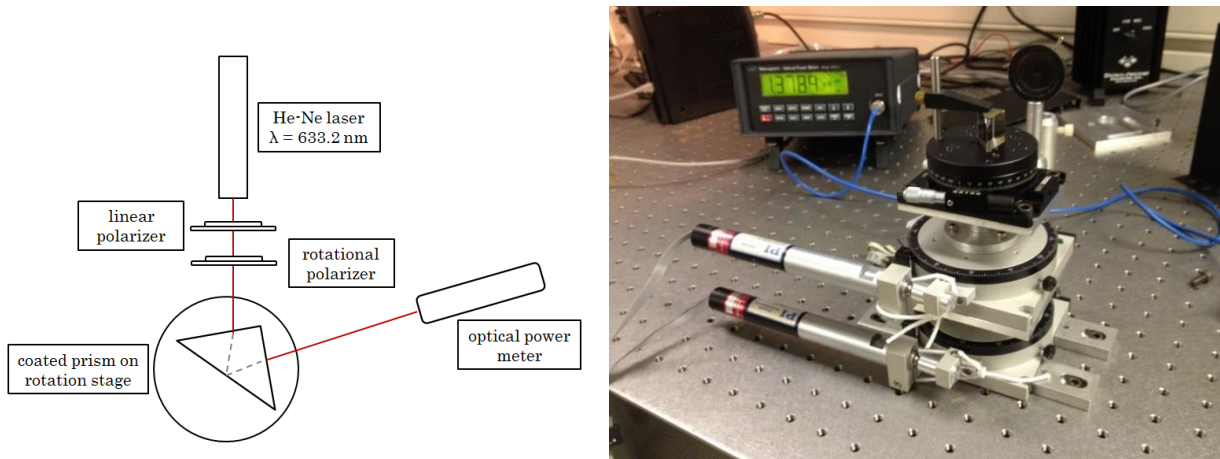
Figure 3.22: Rotation Stage

It is important to stress that only p-polarized light satisfies the boundary conditions for surface plasmon resonance, making the polarization of the input wave of supreme importance. The optimum polarization angle was determined by incrementally rotating the polarization and recording the power after the beam had passed through a third polarizer. This data was then fitted to Malus's Law given by,

$$I = I_0 \cos^2 \theta . \tag{3.4}$$

This allowed for the determination of the cross polarization angle and therefore the polarization offset. Figure 3.23 depicts the polarization data fitted to (3.4) to indicate an ideal offset value of 3.7^0.
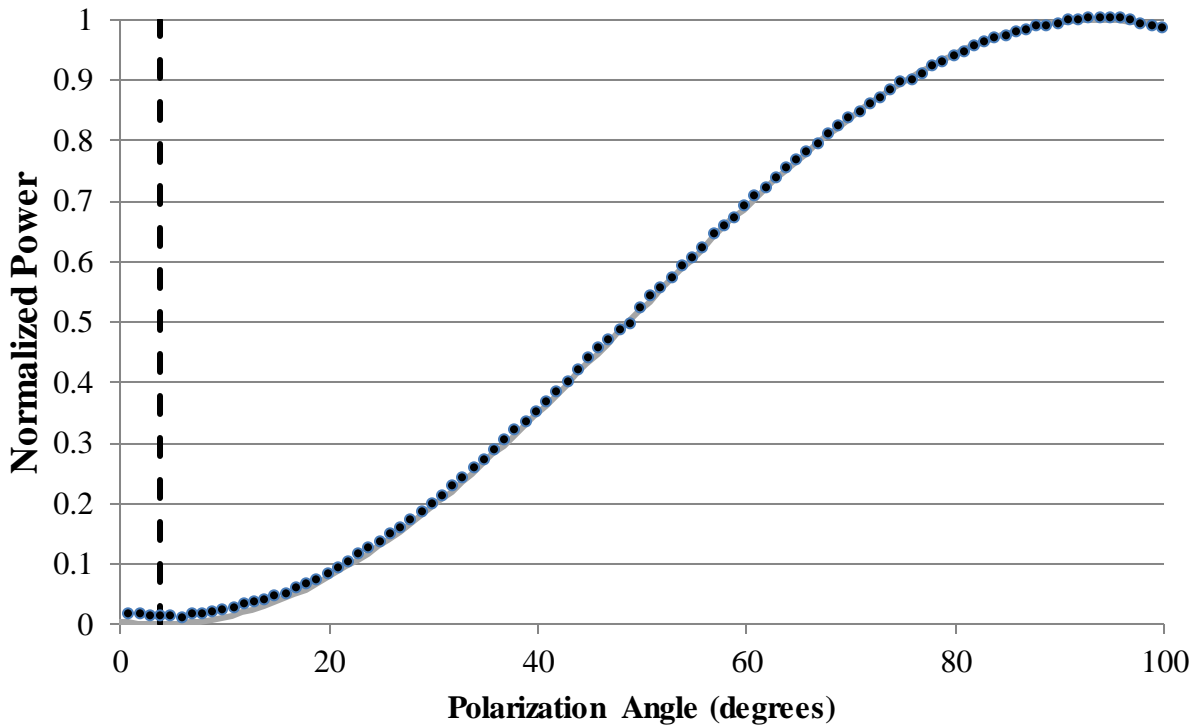
Figure 3.23: Malus's Law Angle Calibration

Physik Instrumente software, which was dedicated to the translation motors, was used to program the course of a scan about the expected plasmon angle. The linearity between the translation motors (Physik Instrumente) and the rotation stage was verified, as shown in Figure 3.24 and Table 4. The motors used were high precision Physik Instrumente translation motors, capable of accurate movements on the order of 0.1μm. The motor controlling the prism stage was programmed to extend in 61 increments of 208.28μm to 12.535mm corresponding to $\theta=0.182^0$, while the motor controlling the power meter was programmed to extend in increments of 415.56μm to 25.7mm, corresponding to $2\theta=0.364^0$. This was done to compensate for the fact that the input source was stationary.
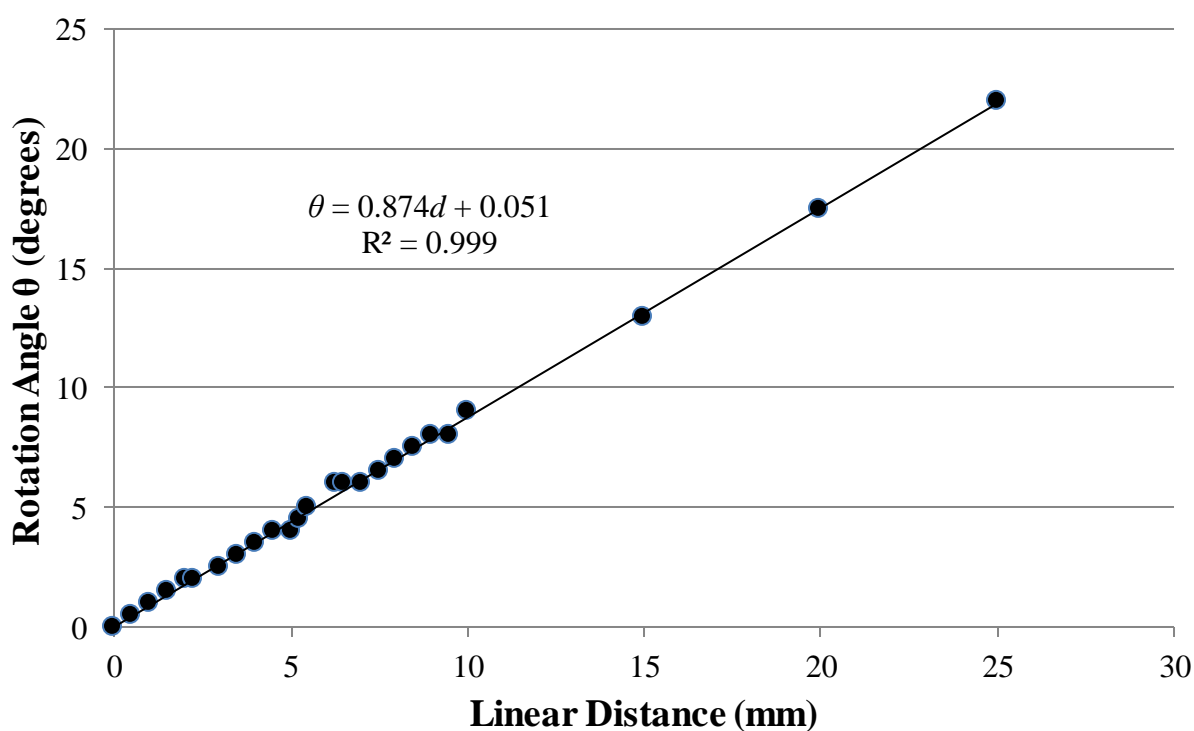
Figure 3.24: Linearity of Stage

Table 4: Rotational stage linearity

Linear distance (mm)	Δθ (degrees)	Linear distance (mm)	Δθ (degrees)	Linear distance (mm)	Δθ (degrees)
0	0	4.5	4	8.5	7.5
0.5	0.5	5	4	9	8
1	1	5.25	4.5	9.5	8
1.5	1.5	5.5	5	10	9
2	2	6.25	6	15	13
2.25	2	6.5	6	20	17.5
3	2.5	7	6	25	22
3.5	3	7.5	6.5		
4	3.5	8	7		

A LabPro analyzer was connected to the power meter to convert the power reading to a voltage, which is compatible with LabPro software. For analysis, the voltage was normalized with respect to the uninterrupted source beam. Because the LabPro software, was not directly integrated into the motorized system, some consideration was made for the data collection program. First, a rest period of 250µs was included between each movement of the motor. This rest provided a stable period, free of vibrations, for each datum to be collected. Also, in the event that the data collection program and the motor macro were slightly out of sync with each other, the rest period would act as a buffer to prevent data from being inadvertently collected while the system was in motion. The second issue presented in reliable data collection was the problem of reconciling the data collection frequency of the LabPro software with the motorized movements. Although the velocity of each motor could be specified within the software, the acceleration was found to be difficult to predict. In determining the number of data points to be collected and the rate at which they were to be collected, the translation motors were allowed to run for the duration of the macro and the script was timed. Initially, the run time was simply divided by the number of movements, and data values were collected for voltage at that period. However, data

recorded under this scheme was prone to oscillation due to asynchronous macros. Ultimately, data was recorded with deliberate oversampling of about 20%, and multiple trials were averaged before each reflection profile was analyzed.

After processing the data, the total internal reflection was plotted as a function of the angle of reflection about the hypotenuse normal. The criterion used to identify the plasmonic activity in this plot was the attenuation of the total internal reflection near the plasmon angle. Greater attenuation indicates more efficient plasmonic coupling, while less attenuation approaches the behavior of normal Fresnel reflection. To test the system, a blank prism was inserted into the system and the data was recorded. Figure 3.25 shows the data for a blank prism fitted to the curve predicted by (2.87) for an interface of silica and air. The MATLAB script used for generating the theoretical curve is shown in Appendix C. The qualitative behavior between the data and the plot match, but there is about 5% loss which is unaccounted for. A likely source of this loss is on the detector head of the power meter, which had minor scratches on its surface.
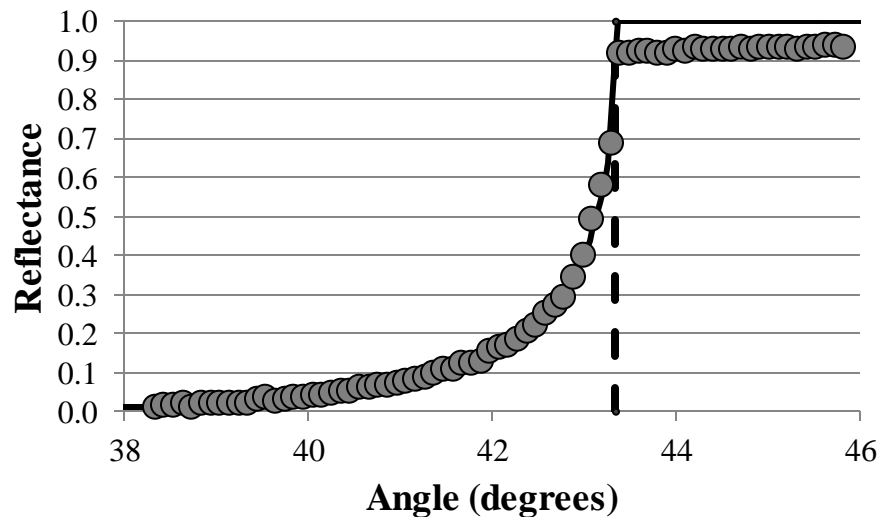
Figure 3.25:Reflectance profile of blank silica prism fitted to fresnel internal reflection

4   RESULTS

The results are presented in four sections. The reflectance curves of single layer silver are presented for five thicknesses. Similar results are presented for single layer nickel chromium at five thicknesses. Then silver is revisited to address modulation of the plasmon angle through the addition of dielectric media to the plasmonic interface. First, reflectance curves for oxide growth on single layer silver are compared. Next, reflectance curves for silver are exhibited for showing the change upon application of PMMA to the interface.

<u>4.1 Silver Results</u>

Figure 4.1 through Figure 4.5 are reflectance plots for five samples of single layer silver of thicknesses between 23.5 nm and 50 nm. The data was fitted to (2.86) and the results are compared to the measured values in Table 5. For all plots, the fitted reflectance curve is plotted in black, the plasmon angle is marked in grey, and the critical angle is indicated for reference by a dashed line.
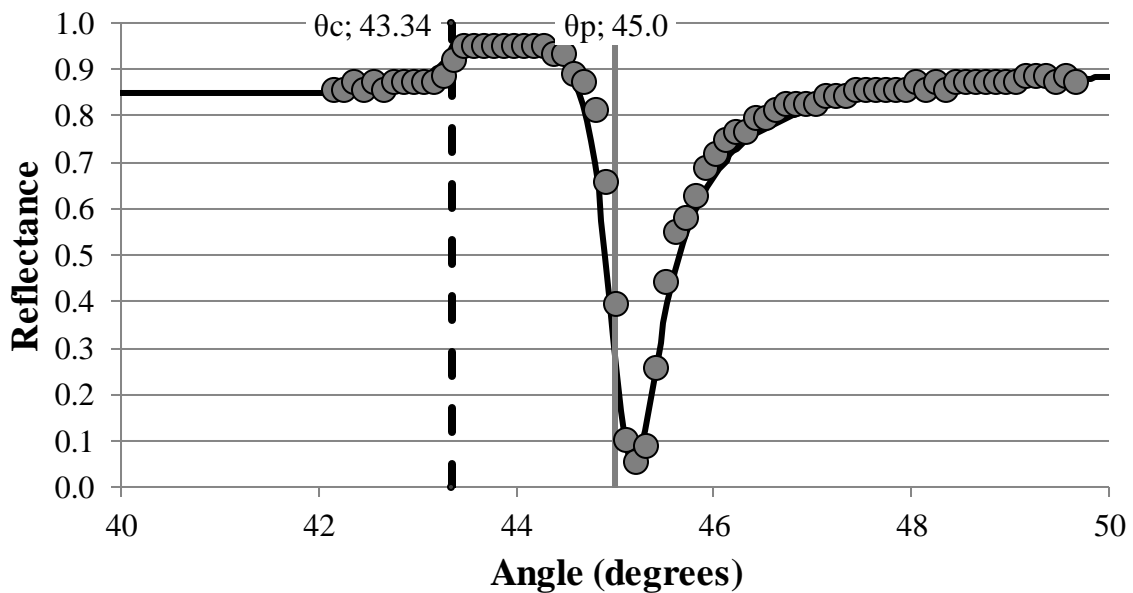
Figure 4.1: Reflectance profile of 23.5 nm Ag on fused silica with fitted curve
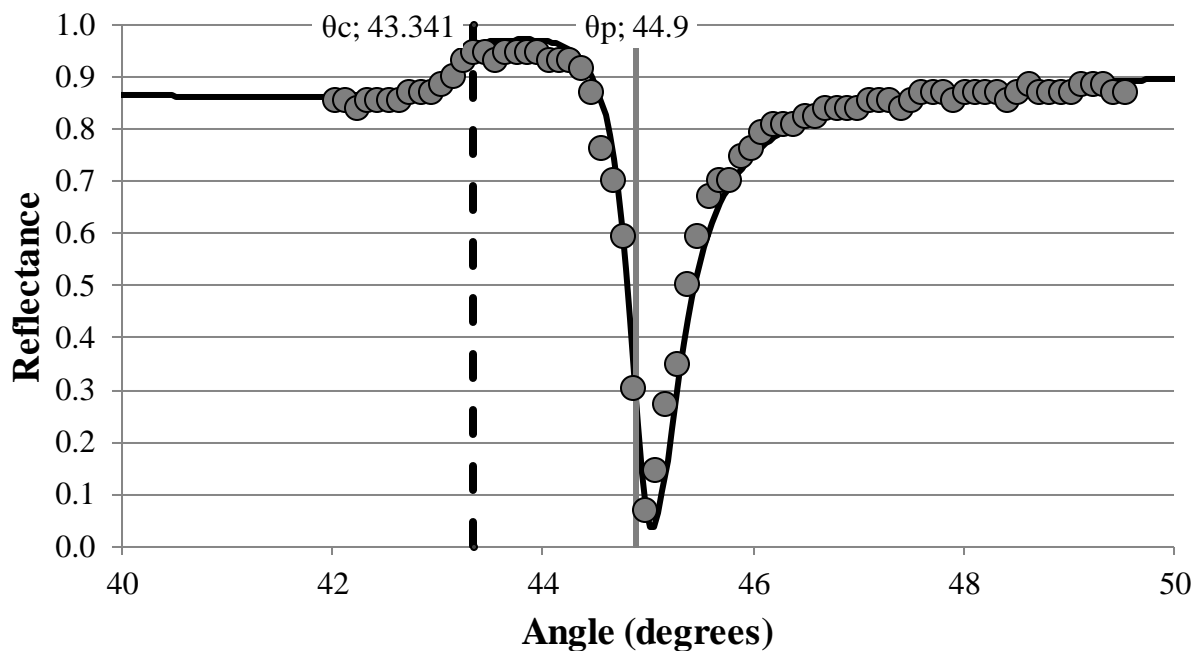
Figure 4.2: Reflectance profile of 23.5 nm Ag on fused silica with fitted curve
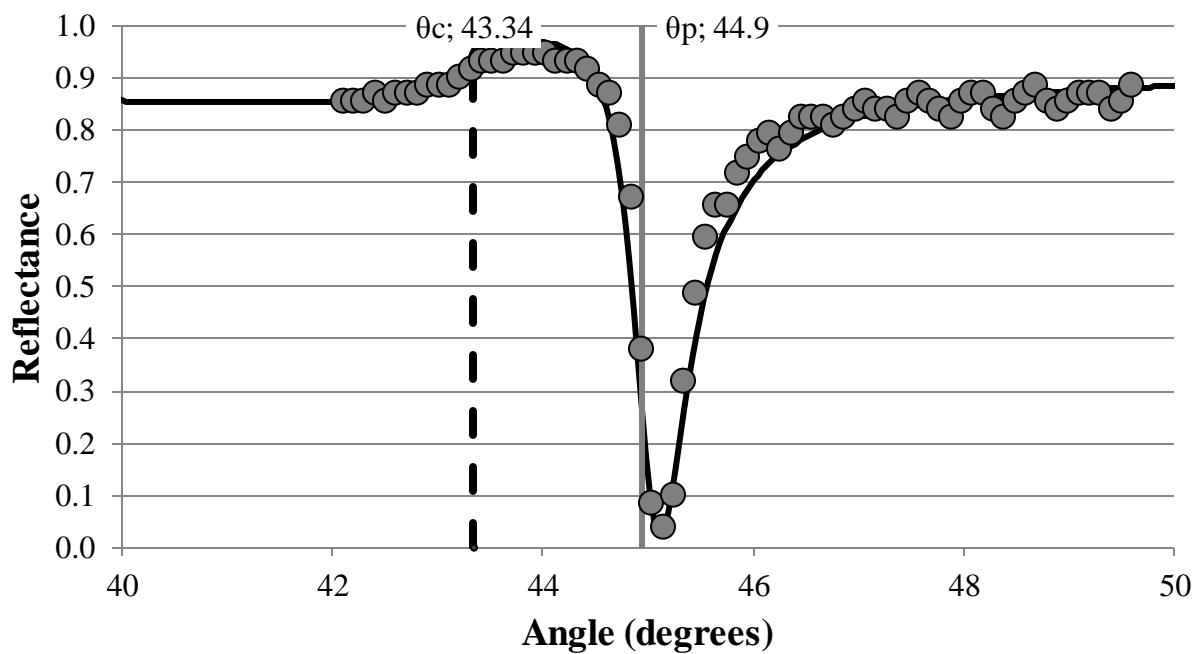
Figure 4.3: Reflectance profile of 24.4 nm Ag on fused silica with fitted curve
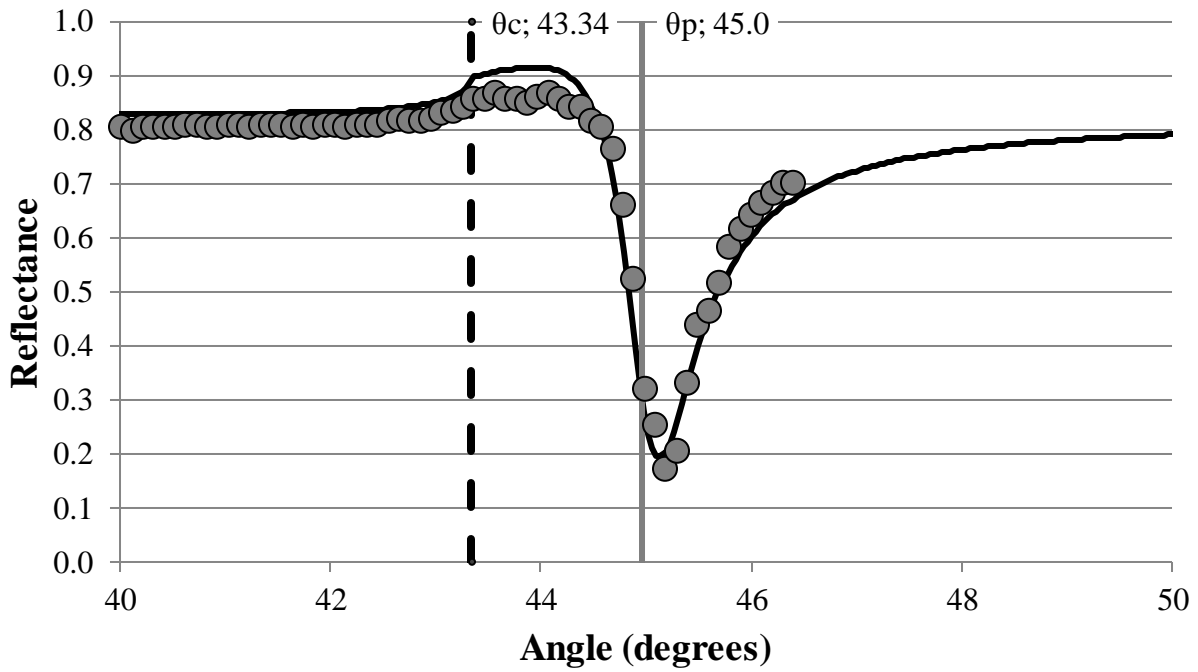
Figure 4.4: Reflectance profile of 30.0 nm Ag on fused silica with fitted curve
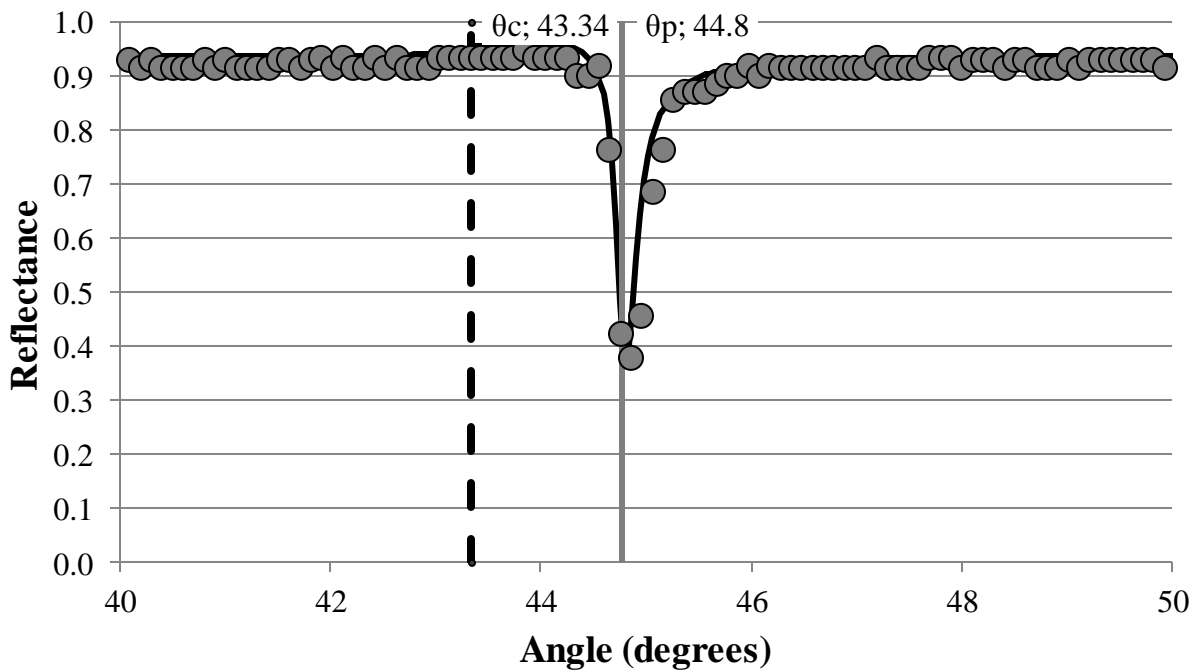
Figure 4.5: Reflectance profile of 45.2 nm Ag on fused silica with fitted curve

Table 5: Semi-Analytical Model Data

Thickness (nm)	ε'	ε''	θ_p	Fit thickness (nm)	ε' (fit)	ε'' (fit)	θ_p (fit)
23.5	-16.9	-0.26	45.04	37.5	-17.96	1.18	44.93
23.5	-18.6	-0.11	44.88	39	-18.36	1.14	44.89
24.4	-17.2	0.00	45.01	39	-17.16	1.1	45
30	-17.9	0.60	44.94	46	-17.16	2.72	44.97
45.2	-19.1	1.85	44.82	58	-19.76	1.26	44.77

4.2Nickel Chromium Results

Figure 4.6 through Figure 4.9 are reflectance plots for five samples of single layer nickel chromium of thicknesses between 20.0nm and 40 nm. The data was fitted to (2.86) and the results are compared to the measured values in Table 6. Again, the fitted reflectance curve is plotted in black, the plasmon angle is marked in grey, and the critical angle is indicated for reference by a dashed line.
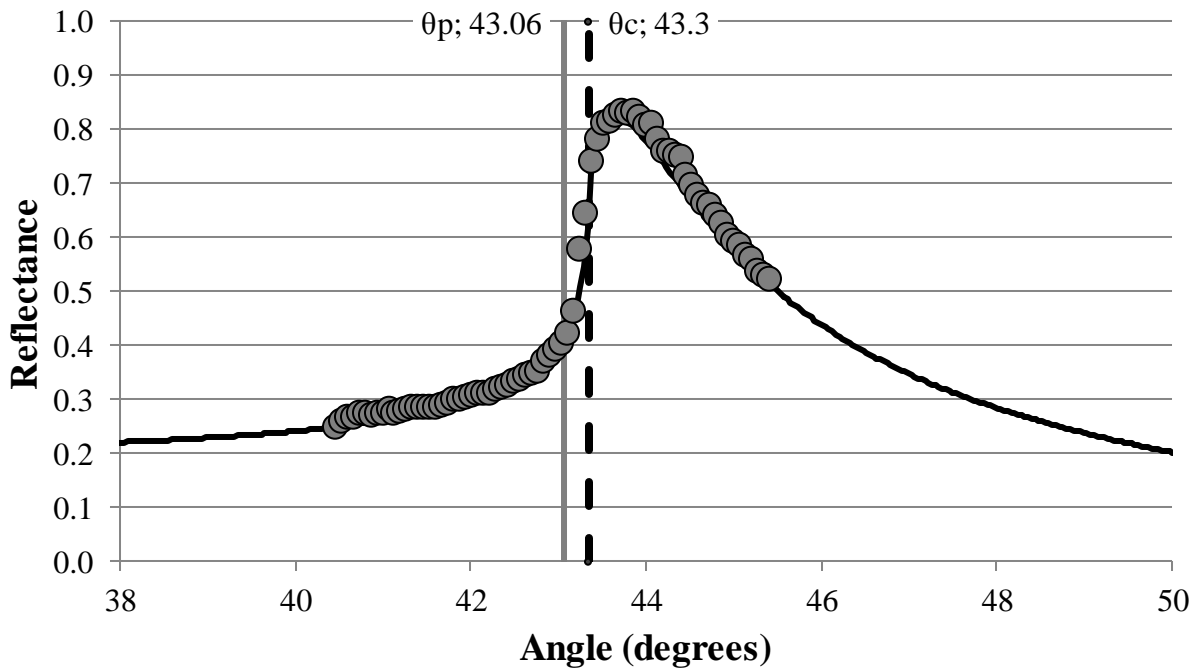
Figure 4.6: Reflectance profile of 18.0 nm NiCr on fused silica with fitted curve
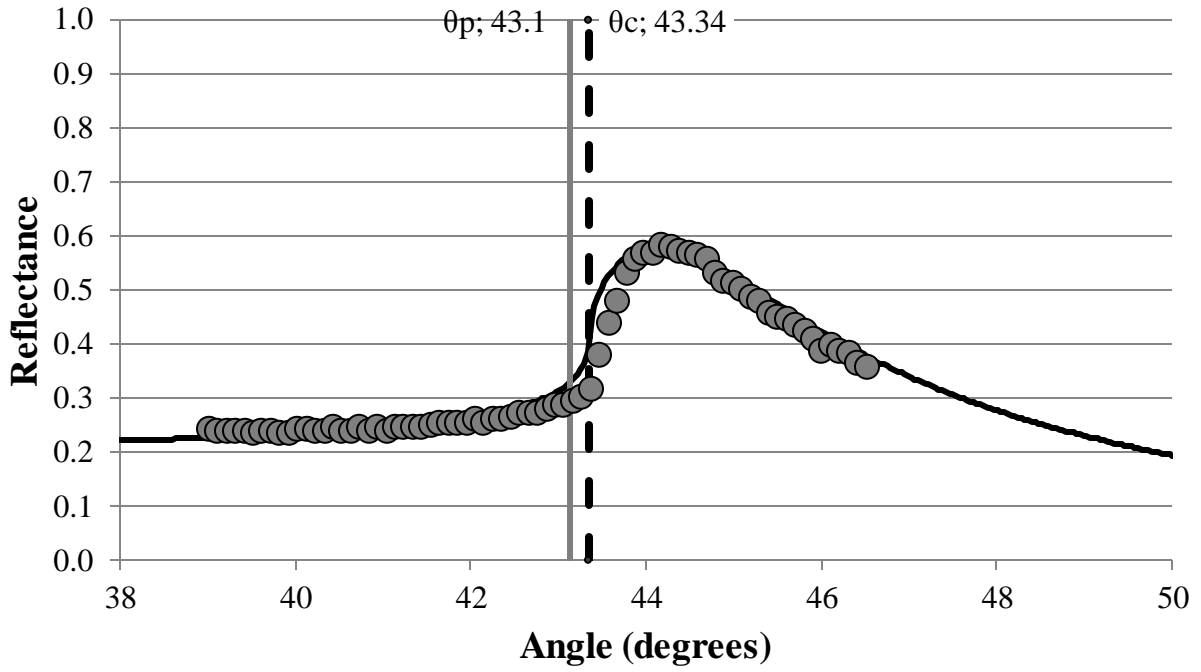
Figure 4.7: Reflectance profile of 30 nm NiCr on fused silica with fitted curve
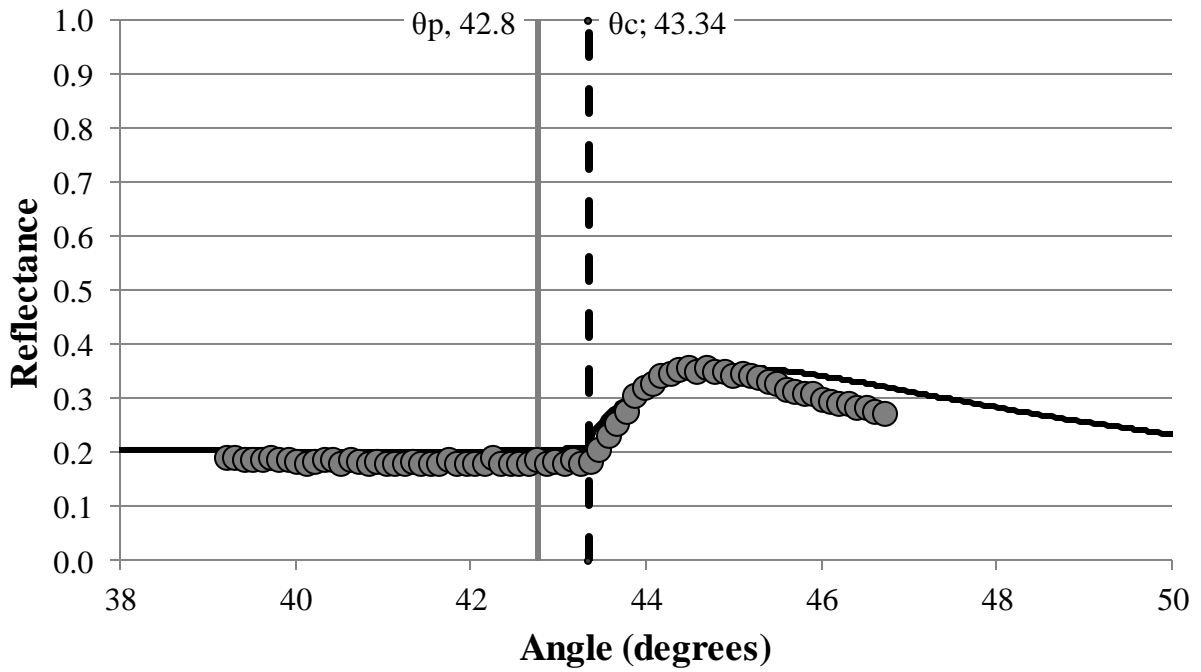
Figure 4.8: Reflectance profile of 30.0 nm NiCr on fused silica with fitted curve
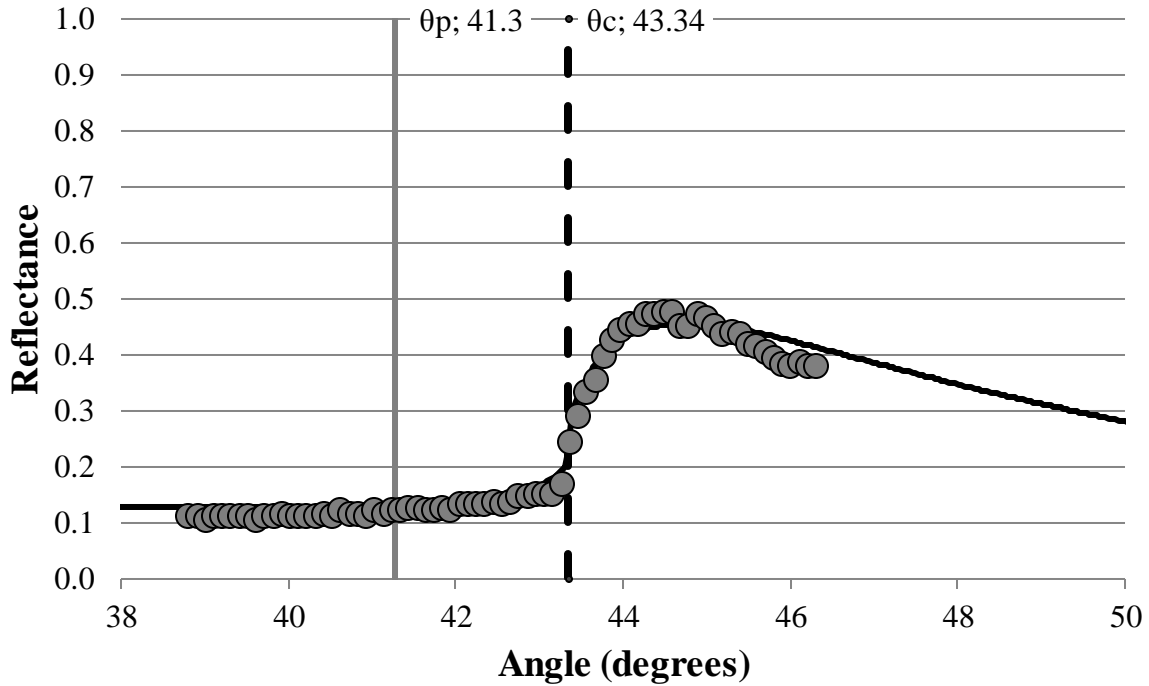
Figure 4.9: Reflectance profile of 40.0 nm NiCr on fused silica with fitted curve

Thickness (nm)	ε'	ε''	θ_p	Fit thickness (nm)	ε' (fit)	ε'' (fit)	θ_p (fit)
18	0.50	15.6	43.18	39	0.48	15.62	43.18
30	2.6	14.9	42.93	35	1.5	15.32	42.77
30	-1.01	15.9	43.34	48.5	2.78	8.78	43.06
40	0.09	19.1	43.26	48.6	3.56	6.22	41.34

Table 6: Semi-Analytical Model Data

4.3 Oxidation of Silver

To test the effects of oxide growth as a variable dielectric material, a nominally 24.4 nm thick film of silver was evaporated onto five samples, and the resulting film thicknesses were measured to be 30 nm. Three of the samples were then oxidized for five minutes at 150 °C, 200 °C, and 300 °C, respectively. The fourth sample was then oxidized at 150 °C for 45 min. Reflectance profiles were then measured for each of the samples with the fifth sample being the control. Figure 4.10 shows the reflectance profiles of all five samples.
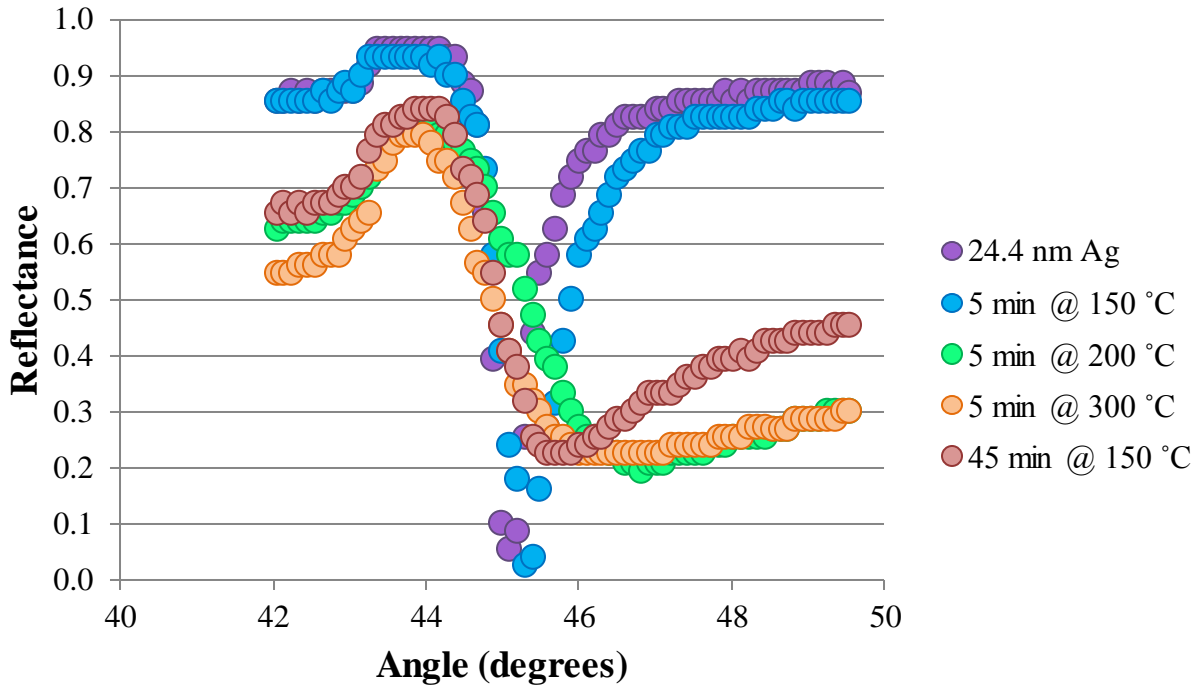
Figure 4.10: Reflectance profiles of 24.4 nm Ag oxidized under various conditions

4.4 Introduction of polymer

To test the effects of the PMMA as a variable dielectric material, a nominally 250 nm thick film of PMMA was spin-coated onto the prism face, after the metal was deposited. This was done for two samples, one with a 15 nm thick layer of silver and one with a 30 nm thick layer. Control samples of equal silver thicknesses were also fabricated for use as controls. Reflectance profiles were then measured for each of the four samples. Figure 4.11 shows the reflectance profile for the 15 nm single layer control sample (circles) and its corresponding test sample with added PMMA (triangles). For reference, the critical angle is indicated in the plots by a black line, and the plasmon angle for the control sample is shown in blue. Similarly, Figure 4.12 shows the reflectance profile for the 30 nm single layer control sample and its corresponding test sample with added PMMA.
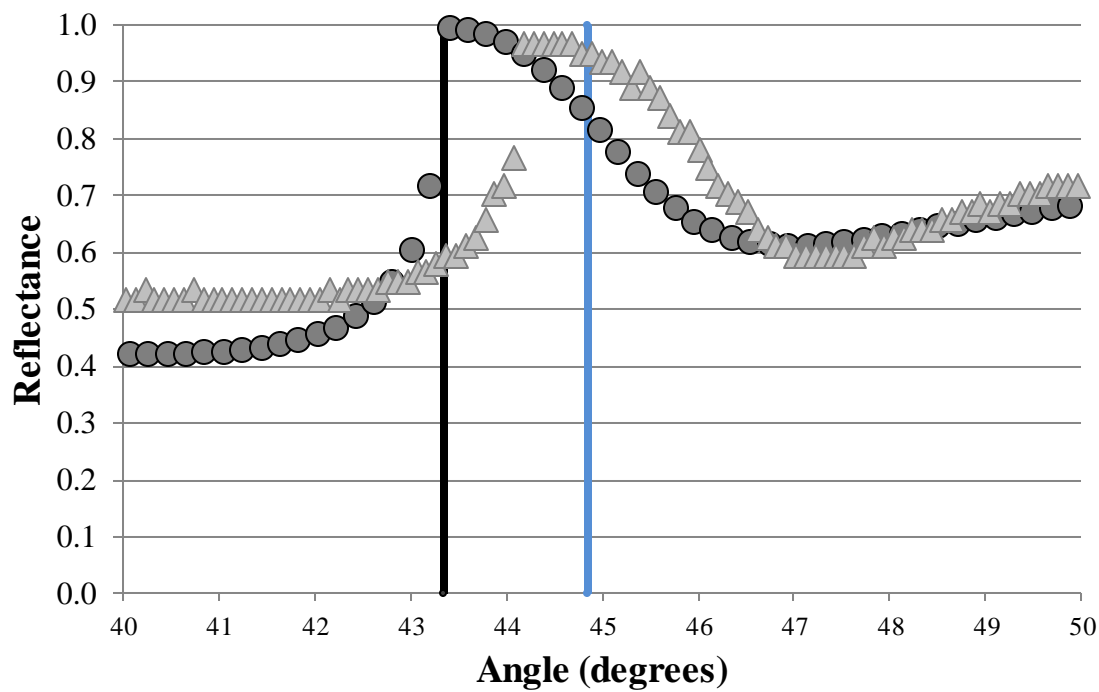
Figure 4.11: Reflectance profiles of 15 nm Ag and (circles) and 15 nm Ag with 500 nm PMMA (triangles)
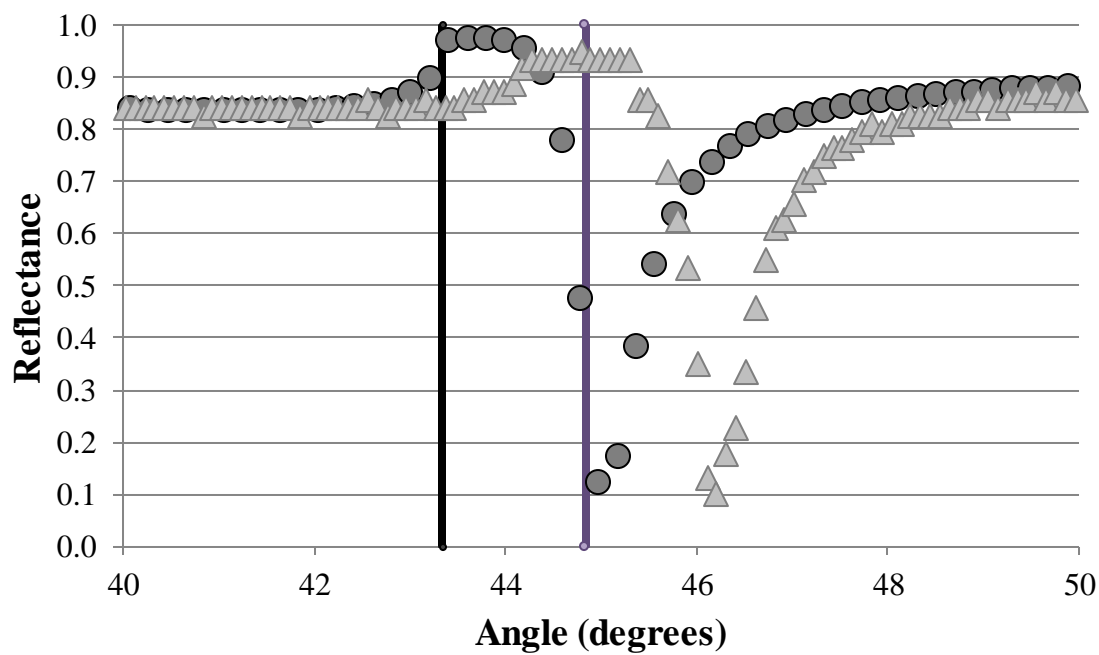
Figure 4.12: Reflectance profiles of 30 nm Ag and (circles) and 30 nm Ag with 500 nm PMMA (triangles)

Poling of the polymers was attempted for both the 15nm silver sample shown in Figure 4.11 and the 30 nm sample shown in Figure 4.12. After poling, a bias voltage was applied to each sample in increments of 10V from 0V to 100V, and reflectance curves were measured. Since no change was apparent after the voltage was applied, the data has not been included.

5   LIMITATIONS

The initial choice to use fused silica prisms as a substrate material was made based on several considerations including the material transmission spectrum, thermal properties, and price. However, for the He-Ne wavelength used in the Kretschmann configuration, this choice resulted in plasmonic activity which occurred very close to the critical angle of total internal reflection in some samples. While these samples exhibited reflectance profiles within the range of acceptability, it is conceivable that similar samples would not. A better choice of substrate at the He-Ne wavelength would be N-BK7 or perhaps SF 59. The higher indices of these glasses would also allow for a more diverse pool of possible dielectric media for opposing surfaces of the Kretschmann interface.

The model used, while well suited for the characterization of single layer thin film interfaces, is not well suited in the form presented to dealing with more complex geometry. It is sometimes generalized to include multiple stacked interfaces, but this approach is unnecessarily cumbersome and rigid, both in terms of analysis and computation. Even in its expanded form, the presented model is not well suited to dynamic simulations. A scattering matrix approach holds some advantage in that it can be easily augmented for multiple layers of different materials once implemented. Appendix E presents a MATLAB script of the scattering matrix method for the geometry discussed in this work. While this method succeeds in predicting the plasmonic behavior of the bound modes of longer wavelength in the infrared spectrum, it fails to predict the radiative modes produced by the He-Ne wavelength. This is likely a byproduct of the two dimensional nature of the model.

A more rigorous approach to predicting plasmonic activity in this work is to solve Maxwell's equations using finite differences in the frequency domain. This method holds major advantages in that it can be expanded to three dimensions and also allows for visualization of the modes being studied. Appendix F exhibits a MATLAB program for modelling Maxwell's equations via finite differences.

In the attempted poling of the electro-optic PMMA, several limiting factors are worth considering. Since no shift in the plasmon angle was observed after the poling process, one of two situations is likely. One cause could be that the poling was entirely unsuccessful. In this case, the process of poling should be reexamined, possibly with a commercial electro-optic polymer in place of the synthesized PMMA solution. Another cause could be that the poling process was partially successful, but only weakly. If this is the case, the temperature, applied voltage, or dye concentration may have been insufficient for complete poling.

6   CONCLUSIONS

For single layer silver, five films were studied at thicknesses between 20nm and 50nm. In all five samples, the plasmonic effect is clearly visible, and the plasmon angle in the fitted plots varies less than 0.2^o for all thicknesses. The depth of the reflectance minimum varied from 0.04 in the thinnest sample to 0.38 in the thickest. These values correspond to a range of dielectric constants for the He-Ne wavelength between $\varepsilon_{He-Ne} = -17.76 + 1.18i$ and $\varepsilon_{He-Ne} = -19.76 + 1.26i$, respectively. As a point of reference, the critical angle for total internal reflection is 43.34^o. This feature is clearly visible in all but the 45.2 nm sample, where it is washed out due to the high base-line reflection of the thicker metal.

While both 23.5 nm silver samples were measured to have negative imaginary dielectric components, these values are close to zero. Specifically, $\varepsilon'' = -0.26$, for the first sample, and $\varepsilon'' = -0.11$ for the second. Since the RMSE value for the ellipsometric fit function is calculated based on all measured wavelengths, it is not unreasonable to obtain some values which are slightly deviant from what is expected. Further, since the qualitative behavior of both plots shown in Appendix A is consistent with the Drude model, and since $\varepsilon'' = 0.00$ for the 24.0 nm thick sample of silver, both deviant measurements can be considered acceptably close to the null absorption value of $\varepsilon'' = 0$.

For single layer nickel chromium, five films were studied at thicknesses between 20nm and 40nm. In these samples, the plasmonic activity is more difficult to parse through inspection, which is due primarily to the location of the plasmon angle. The plasmon angle was located very close to or at a smaller angle than that of total internal reflection for the prism. This indicates that the He-Ne spectral line might reside outside of the metallic regime for NiCr. Still, the reflectance

plots fit the model well, even though they indicate negative real components of their dielectric constants. There is a clear trend toward lower plasmon angles for thicker samples.

The reflectance curves for oxidized silver were shifted with respect to the control sample of single layer silver. As the temperature of the oxidation environment was increased for equal time intervals from 150°C to 200 ^{o}C and 300 ^{o}C, the samples exhibited reflectance profiles that were progressively more deviant from the control. This is consistent with the expectation that higher temperatures will hasten the oxidation process, leaving more dielectric oxide on the plasmonic interface. Because the difference between oxidation at 150°C and 200 ^{o}C is more substantial than the difference between oxidation at 200°C and 300 ^{o}C it can be determined that the oxidation approaches saturation quickly at high temperatures. A relationship is also apparent between the interval of time a sample was in the oven at 150°C and the deviation from the control. For a longer interval in the oxidation environment, the reflectance profile approaches that of the higher temperatures. Again, the sample is approaching saturation.

The reflectance curve of the sample comprised of a 15nm thick silver layer and PMMA coating shifted substantially from the control sample profile. Both the plasmon angle and the critical angle were shifted. The total deviation of the plot minimum was 0.3^{o} and the deviation of the critical angle was 0.8^{o}. The reflectance curve of the sample comprised of a 30nm thick silver layer and PMMA coating also shifted with respect to its control sample profile. The total deviation of the plot minimum was 1.2^{o}, and the deviation of the critical angle was 0.9^{o}.

LIST OF REFERENCES

[1] Wu, L., Chu, H. S., Koh, W. S., & Li, E. P. (2010, June 21). Highly sensitive graphene biosensors based on surface plasmon resonance. Optics Express, 14395-14400.

[2] M. Syed, C. Leibs and A. Siahmakoun, "Surface Plasmon Resonance (SPR) Effect in Nanoscale Nichrome Alloy Films," 2008 17th Biennial University/Government/Industry Micro/Nano Symposium, Louisville, KY, 2008, pp. 245-248.doi: 10.1109/UGIM.2008.72

[3] Horvath, A., Roddy, M., Syed, M., & Siahmakoun, A. (2010). Contrast Reversal on Surface Plasmon Resonance Reflectivity in Nickel and Nickel Alloy Films. Proceedings of the SEM Annual Conference. Indianapolis, Indiana: Society for Experimental Mechanics Inc.

[4] Gupta, B. D., & Verma, R. K. (2009). Surface Plasmon Resonance-Based Fiber Optic Sensors: Principle Probe Designs, and Some Applications. Journal of Sensors, 1-12.

[5] Otto, A. (1968). Excitation of Nonradiative Surface Plasma Waves in Silver by the method of Frustrated Total Reflection. Zeitschrift Physik Z. Physik, 398-410.

[6] Simon et al (1975). Surface plasmons in silver films -- a novel undergraduate experiment. Am. J. Phys.,630-636.

[7] Kretschmann, E. H. Raether (1968). Radiative Decay of Non Radiative Surface Plasmons Excited by Light. Notizen, 2135-2136

[8] Krasavin, A. V., K., F. M., & Zheludev, N. I. (2004, October 18). High-contrast modulation of light with light by control of surface plasmon polariton wave coupling. Applied Physics Letters, 85(16).

66

[9] Xiao, F., Li, G., Alameh, K., & Xu, A. (2012, November 15). Fabry-Perot-based surface plasmon resonance sensors. Optics Letters, 37(22), 45824584.

[10] Maier, S. A. (2007). Plasmonics: Fundamentals and Applicaitons. Bath, United Kingdom: Springer Science+Business Media LLC.

[11] Zhang, X., & Stroud, D. (1995, July). Optical and electrical prperties of thin films. Physical Review B, 52(3), 2131-2137.

[12] Rumpf, R. C. (2011, October 18). Improved Formulation of Scattering Matrices for Semi-anallytical Methods that is Consistent with Convention. Progress In Electromagnetics Research B, 35, 241-261.

[13] Anderson, D. R. (2010, March 31). Graphene-based long-wave infrared TM surface plasmon modulator.

[14] Hilfiker, J. N., & Woollam, J. A. (2004). Ellipsometry. In R. D. Guenther, D. G. Steel, & L. Bayvel (Eds.), Encyclopedia of Modern Optics. Oxford.

[15] Hooper, I. R., & Sambles, J. R. (2004, September 1). Sensing using differential surface plasmon ellipsometry. Journal of Applied Physics, 96(5), 3004-3011.

[16] Tompkins, H., & Irene, E. (2005). eds. Handbook of Ellipsometry. William ANdrew Publishing.

[17] Fujiwara, H. (2007). Spectroscopic Ellipsometry Principles and Applications. West Sussex England: John Wiley & Sons.

APPENDICES

68

APPENDIX A.   Silver Sample Step Profiles
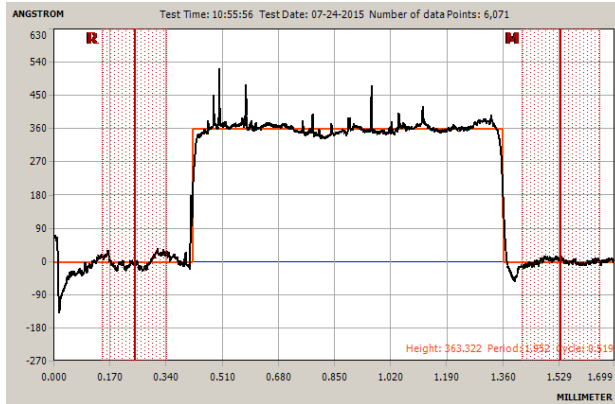
Figure A.1: Profilometer step for a nominally 36.3 nm thick Ag sample
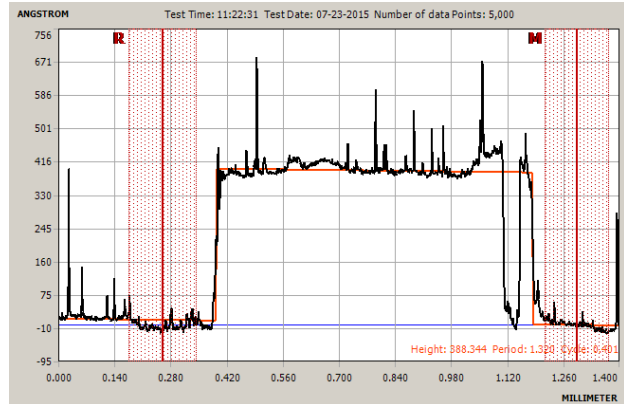
Figure A.2: Profilometer step for a nominally 38.8 nm thick Ag sample
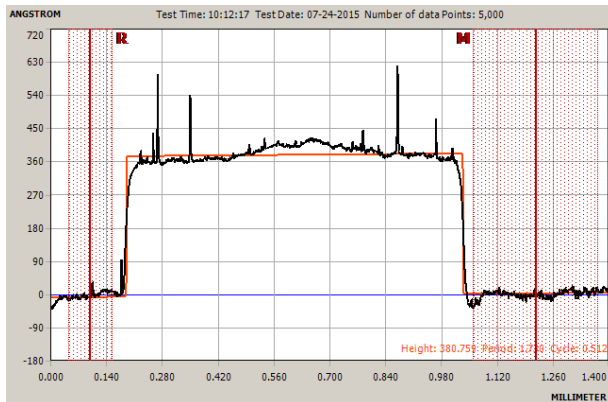
Figure A.3: Profilometer step for a nominally 38.1 nm Ag sample
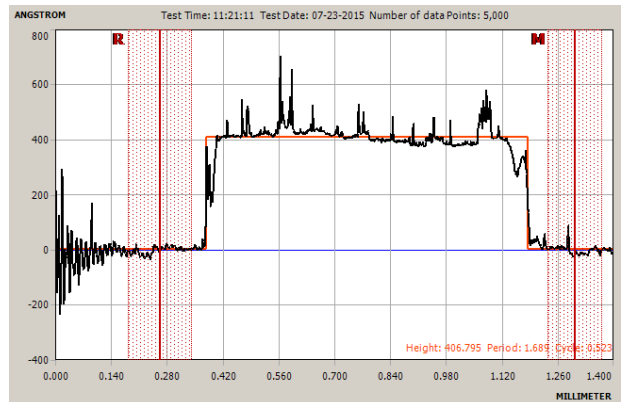
Figure A.4: Profilometer step for a nominally 40.6 nm Ag sample
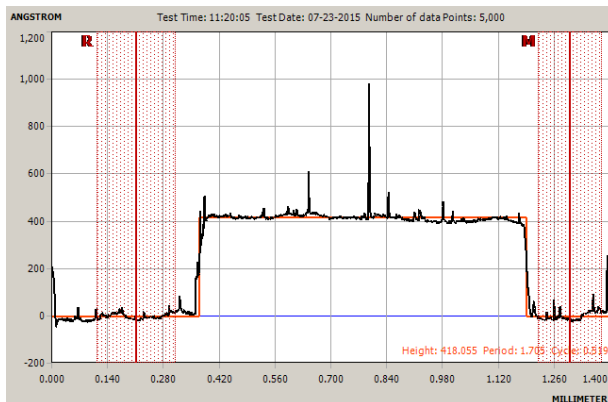
Figure A.5: Profilometer step for a nominally 41.8 nm Ag sample
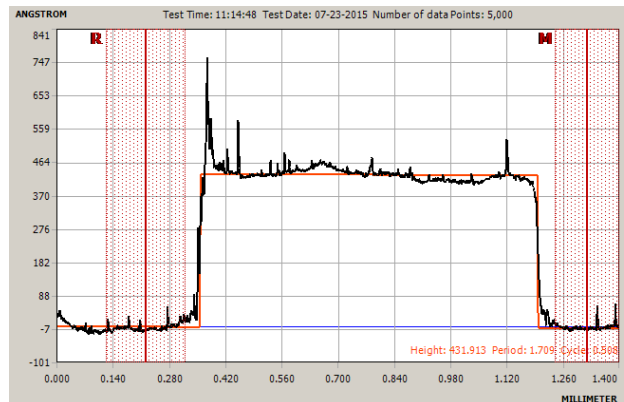
Figure A.6: Profilometer step for a nominally 43.2 nm Ag Ag sample

APPENDIX B.   Silver Sample Dielectric Functions
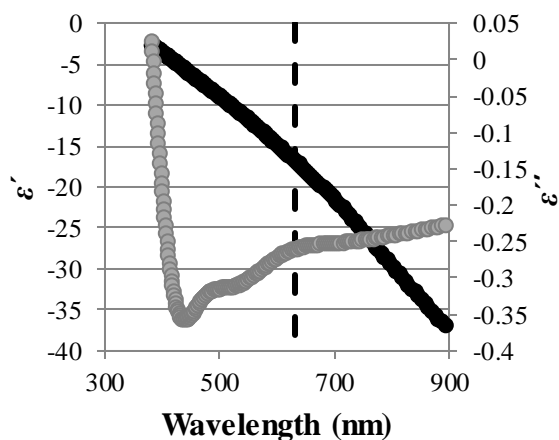
Figure B.1: Measured ellipsometric dielectric curves for 23.5nm Ag
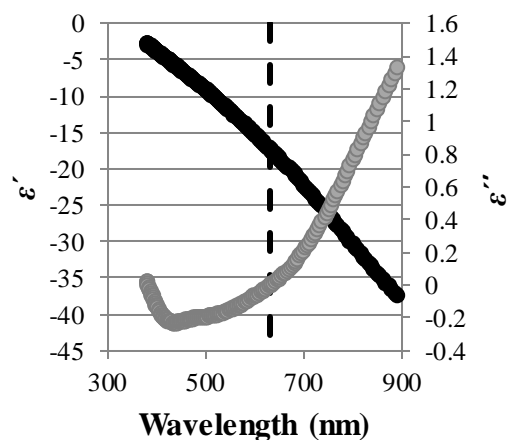
Figure B.2: Measured ellipsometric dielectric curves for 24.4 nm Ag
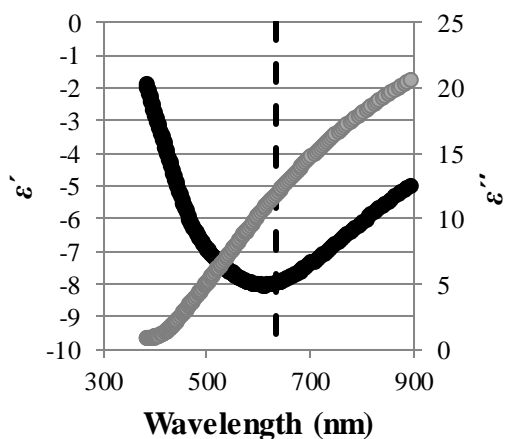
Figure B.3: Measured ellipsometric dielectric curves for 24.6 nm Ag
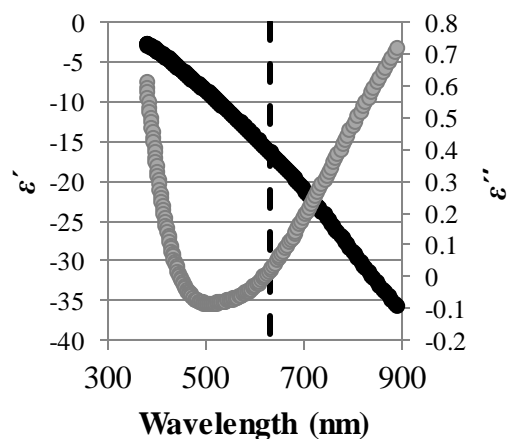
Figure B.4: Measured ellipsometric dielectric curves for 15nm Ag
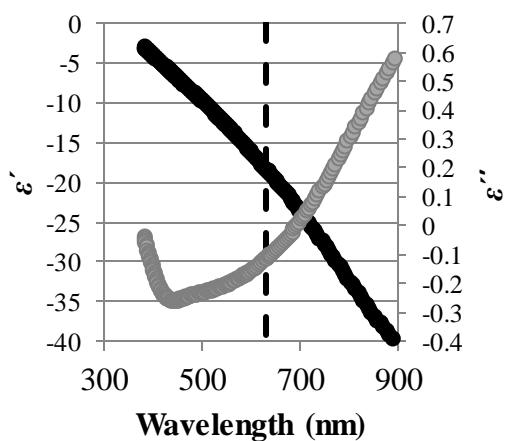
Figure B.5: Measured ellipsometric dielectric curves for 23.9 nm Ag
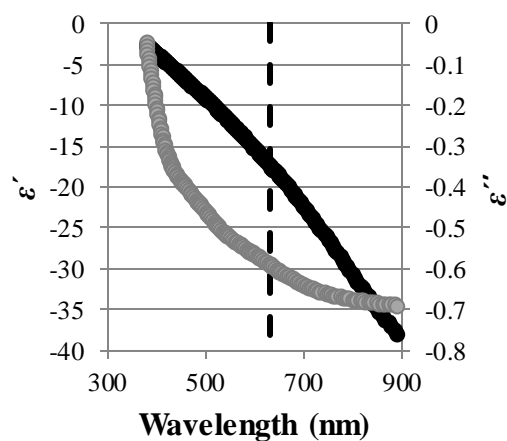
Figure B.6: Measured ellipsometric dielectric curves for 24.7 nm Ag
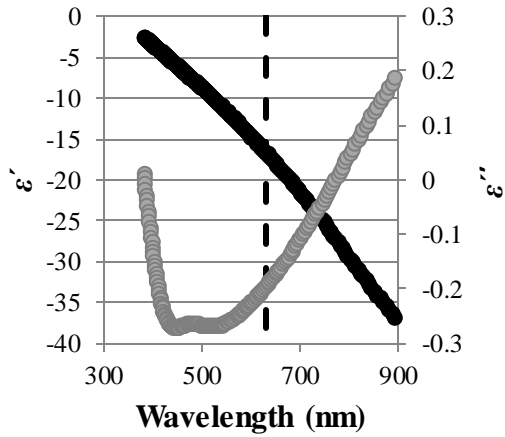
Figure B.7: Measured ellipsometric dielectric curves for 24.7 nm Ag
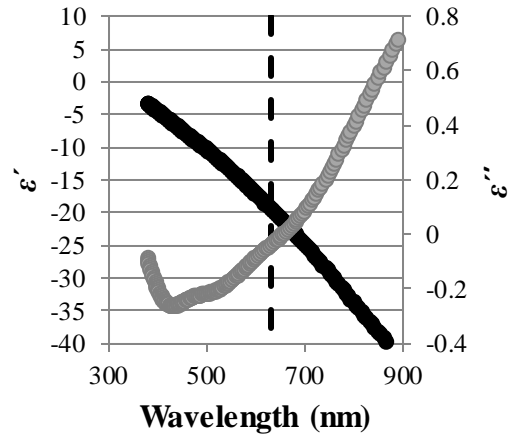
Figure B.8: Measured ellipsometric dielectric curves for 23.4 nm Ag
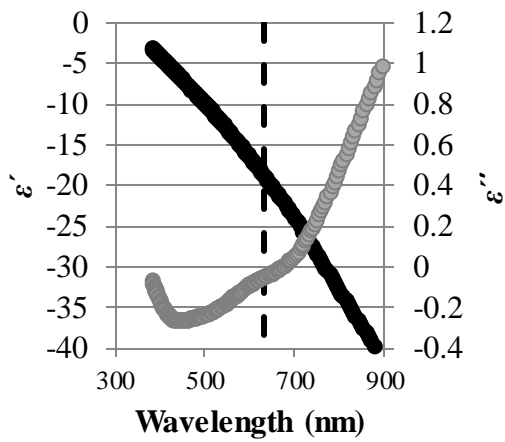
Figure B.9: Measured ellipsometric dielectric curves for 39.6nm Ag
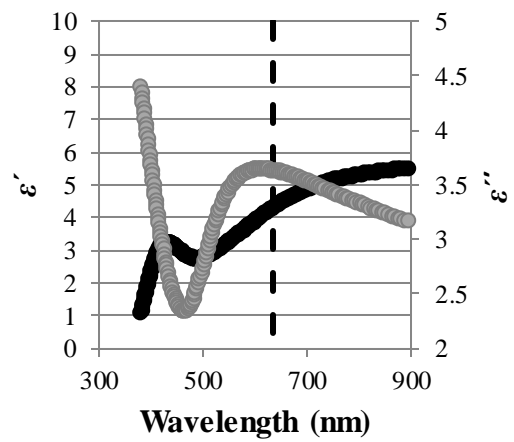
Figure B.10: Measured ellipsometric dielectric curves for 24.5 nm Ag
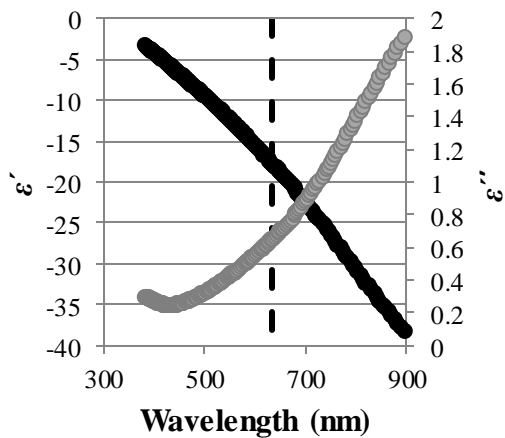
Figure B.11: Measured ellipsometric dielectric curves for 60 nm Ag

APPENDIX C.   NiCr Sample Dielectric Functions
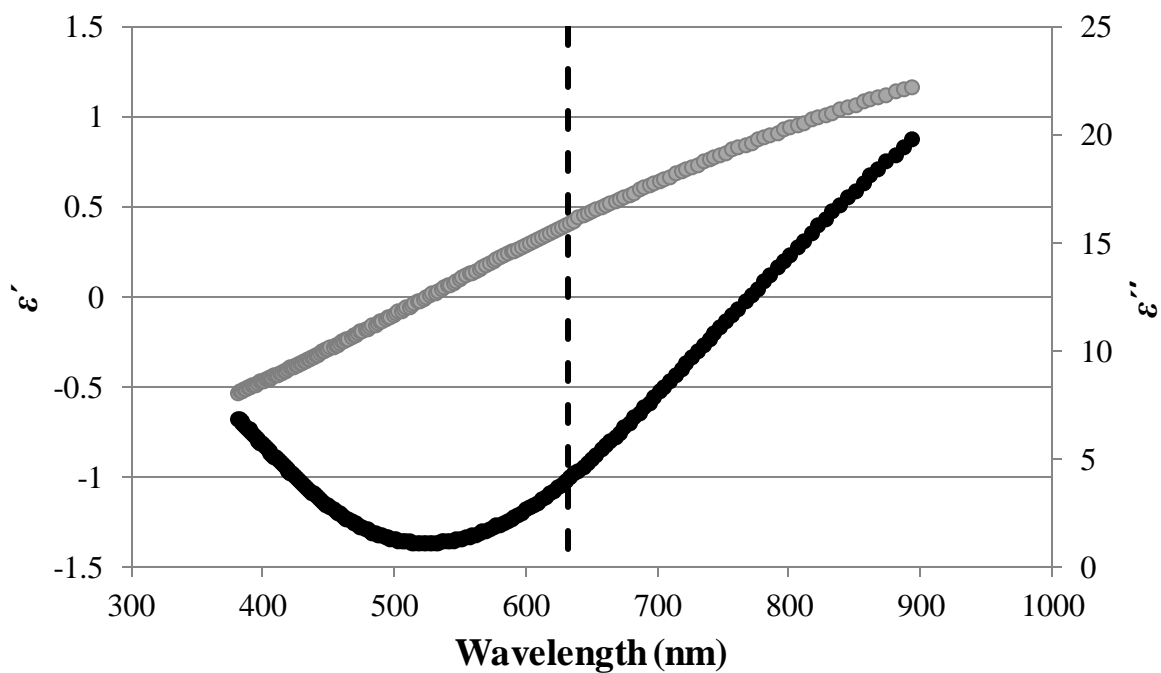
Figure C.1: Measured ellipsometric dielectric curves for 30nm NiCr
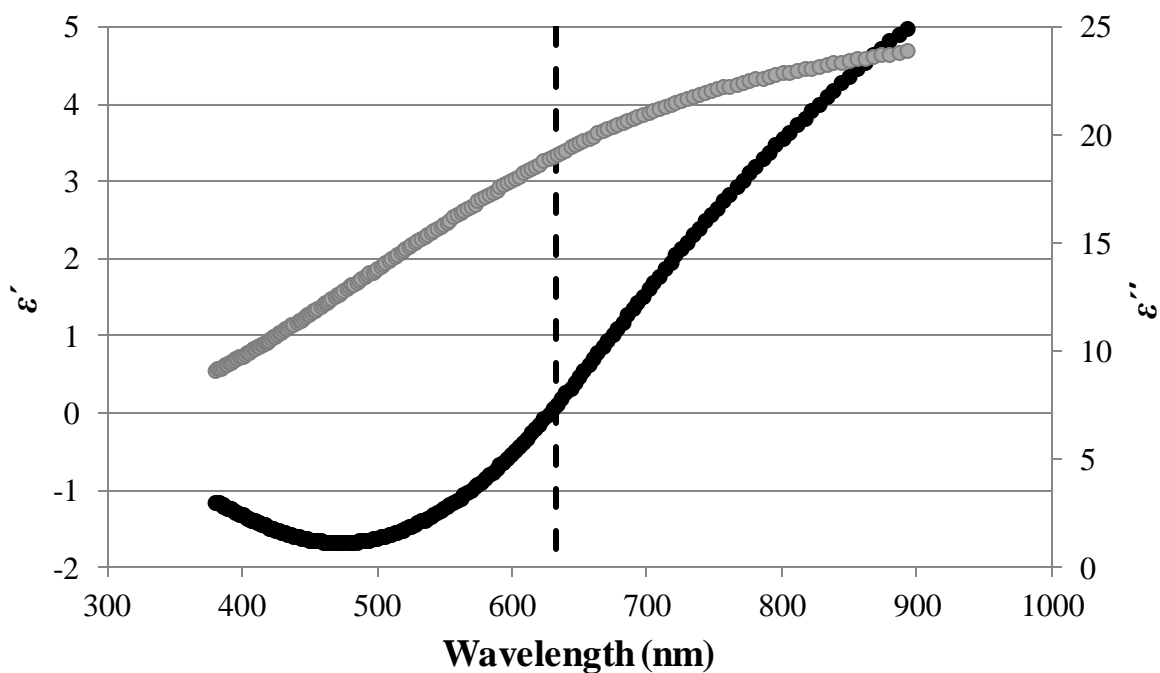
Figure C.2: Measured ellipsometric dielectric curves for 40nm NiCr

APPENDIX D. Calculation of the Semi-Analytical Reflectance Response

```matlab
%This program calculates reflectance according to the model developed in
%Simon's Paper. It incorporates a thin metal film (e1+ie2) sandwiched
%between a dielectric of index n and air
close all
clear variables
clc

%Insert the appropriate wavelength (wl) in angstroms, film thickness (d) in
%angstroms, index of refraction (n), complex dielectric function (ep)
%below.
pi = 3.141592654;
wl = 6328.0;
d = 350;
n = 1.457;
ep = complex(-17,2);
degrees = 180/pi;

%theta1 refers to the angle incident to the prism
%theta2 refers to the refracted angle inside of the prism.
%theta3 refers to the angle incident upon the the thin film.

theta3 = linspace(0.03,1.5510,507);
theta2 = theta3 - (pi/4);
theta1 = asin(n*sin(theta2));

%k is the absorption coefficient for the E filed in the metal.

k = -(j*2*pi/wl)*(ep-n^2*(sin(theta3)).^2).^0.5;

%T2 is the cosine of the angle inside the thin film.
%T3 is the cosin of the angle in the air outside the thin film.


T2 = (1-n^2*(sin(theta3)).^2/ep).^0.5;
T3= (1-n^2*(sin(theta3)).^2).^0.5;

%r12 is reflectivity at the silica - metal interface.
%r23 is reflectivity at the metal - air interface.

r12 = (ep^0.5*cos(theta3)-n*T2)./(ep^0.5*cos(theta3)+n*T2);
r23 = (T2-ep^0.5*T3)./(T2+ep^0.5*T3);

%R is the total reflectivity at the  thin film.


R1= (r12+r23.*(exp(-2*k*d)))./(1+r12.*r23.*(exp(-2*k*d)));
R = R1.*conj(R1);

%Ta is the percentage of light entering the prism
%Tc is the percentage of light exiting the prism.

Ta = 1-((cos(theta2)-n*cos(theta1))/(cos(theta2)+n*cos(theta1)))^2;
```

```
Tc = 1 - ((n*cos(theta1)-cos(theta2))/(n*cos(theta1)+cos(theta2)))^2;

%Rmain is the total reflected light exiting the prism.
Rmain = R;

figure(1)
    plot(theta3*degrees,R)
    axis([theta3(1)*degrees theta3(length(theta3))*degrees 0 1])
    xlabel('\theta3 (degrees)','fontsize',12);
    ylabel('Reflectance', 'fontsize', 12);
      title('Reflectance vs \theta3','fontsize',12)
    fh = figure(1);
    set(fh, 'color', 'white');


xlswrite('plasmonmodel121813',R')

thetap = asin((ep/(ep+1)).^.5/n)
```
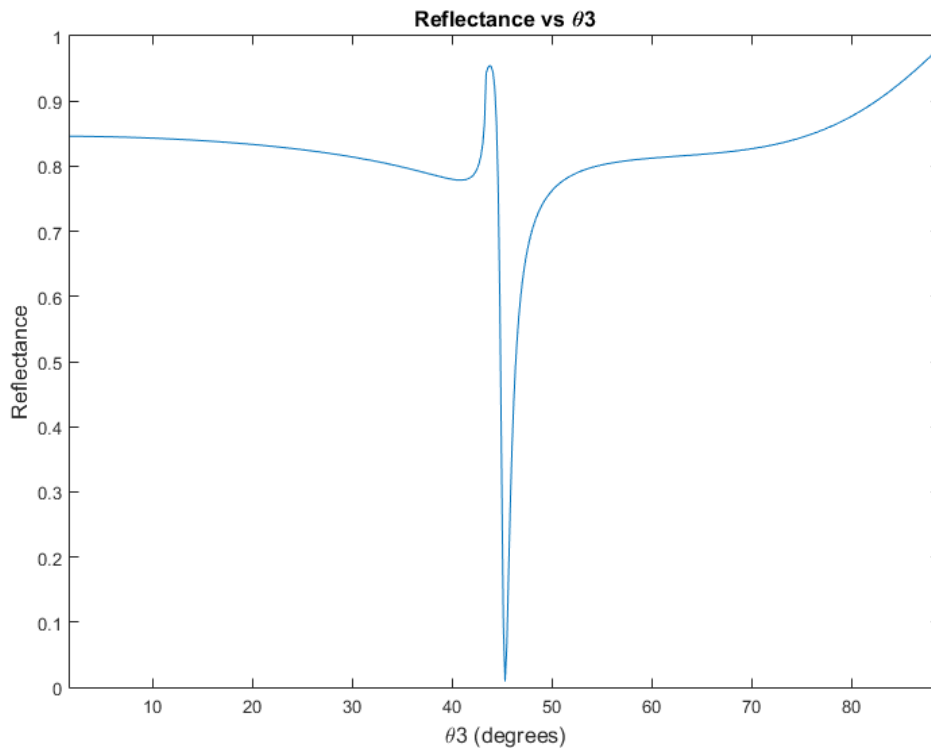

Figure D.1: Theoretical reflectance Profile for MATLAB script

APPENDIX E.   Calculation of the Scattering Matrix Reflectance Response

```matlab
%transfer matrix method; linear, homogeneous, isotropic material
%Based on R.C. Rumpf's Computational CEM Lectures
%Benjamin Hall
%-------------------------------------------------------------------------
----------------------------------
clc;
clear all;
close all;

%source
lam = 4000*1e-9; %wavlength of source in freespace
k0 = 2*pi/lam;
degrees = pi/180; % converts degree input to radians
theta = (20:.01:60)*degrees; %transverse plane; w.r.t. normal; plane of
incidence
phi = (0)*degrees; %sagittal plane; sweeps in x-y plane
normal = [0, 0, -1]; % surface normal

%polarization
delta = 0*degrees; % polarization angle w.r.t. plane of incidence
ptm = cos(delta); %transverse magnetic; p-polarization; parallel to plane of
incidence
pte = sin(delta); %transverse electric; s-polarization;


%external medium parameters
ur1 = complex(1,0); %permiability in incident medium
er1 = complex(2.122849,0.0); %permittivity in incident medium
ur2 = complex(1,0); %permiability in exit medium
er2 = complex(1,0); %permiability in exit medium
ni = real(sqrt(er1*ur1)); % refractive index of incident medium

%layer parameters
MuRelative_real = [1 1];
MuRelative_imaginary = [0 0];
UR = complex(MuRelative_real,MuRelative_imaginary); % relative permiability
array
EpsilonRelative_real = [-18.42 2.56]; % real component of silver dielectric
function
EpsilonRelative_imaginary = [-0.38 0]; % imaginary compnent of silver
dielectric function
ER = complex(EpsilonRelative_real,EpsilonRelative_imaginary); % relative
permittivity array
L = [500 1000].*1e-9; % layer thicknesses array


%empty arrays for reflection and transmission scan
R_scan = zeros(1,length(theta));
T_scan = zeros(1,length(theta));
A_scan = zeros(1,length(theta));

%create array for polarization vectors at each angle
```

```matlab
%for loop for angle theta scanning
for q = 1:length(theta)
%calculate transverse wave vectors
kx = ni*sin(theta(q))*cos(phi); %kx is constant through all layers (LHI)
ky = ni*sin(theta(q))*sin(phi); %ky is constant through all layers (LHI)
kzh = sqrt(1-kx*kx-ky*ky); % free space kz

% free space parameters
Wh = eye(2);
Qh = [kx*ky, 1-kx^2; ky^2-1, -kx*ky];
Omegah = 1i*kzh*eye(2);
lambdah = 1i*kzh*eye(2);
Vh =  -1i*Qh; % Qh/Omegah

% initial global scattering matrix
S12 = eye(2);
S21 = eye(2);
S11 = zeros(2,2);
S22 = zeros(2,2);

% reflection side external region
kz_ref = sqrt(ur1*er1-kx^2-ky^2);
W_ref = eye(2);
Q_ref = (1/ur1)*[kx*ky, ur1*er1-kx*kx; ky*ky-ur1*er1, -kx*ky];
Omega_ref = 1i*kz_ref*eye(2);
V_ref = Q_ref*(Omega_ref^-1);
L_ref = 0;

% scattering matrix for incident medium
A_ref = Wh\W_ref + Vh\V_ref;
B_ref = Wh\W_ref - Vh\V_ref;
S11_ref = -(A_ref^-1)*B_ref;
S12_ref = 2*A_ref^-1;
S21_ref = 0.5*(A_ref-B_ref/A_ref*B_ref);
S22_ref = B_ref/A_ref;

%updating global scattering matrices by Redheffer star product
D = S12_ref/(eye(2)-S11*S22_ref);
F = S21/(eye(2)-S22_ref*S11);
S22 = S22 +F*S22_ref*S12;
S21 = F*S21_ref;
S12 = D*S12;
S11 = S11_ref +D*S11*S21_ref;




% loop calculates and updates the global scattering matrix through device
for i = 1:length(L)

    %Parameters for Layer i
    kz_i = sqrt(UR(i)*ER(i)-kx^2-ky^2);
    Q_i = (1/UR(i))*[kx*ky, UR(i)*ER(i)-kx^2; ky^2-UR(i)*ER(i), -kx*ky];
    Omega_i = 1i*kz_i*eye(2);
```

```matlab
    V_i = Q_i/(Omega_i);


    %Scattering Matrix for Layer N
    A_i = eye(2)+(V_i)\Vh;
    B_i = eye(2)-(V_i)\Vh;
    X_i = diag(exp(-diag(Omega_i)*k0*L(i)));
    S11_i = (A_i-X_i*B_i/A_i*X_i*B_i)\(X_i*B_i/A_i*X_i*A_i-B_i); % also equal
to s22
    S22_i = (A_i-X_i*B_i/A_i*X_i*B_i)\(X_i*B_i/A_i*X_i*A_i-B_i);
    S12_i = (A_i-X_i*B_i/A_i*X_i*B_i)\X_i*(A_i-B_i/A_i*B_i); % also equal to
s21
    S21_i = (A_i-X_i*B_i/A_i*X_i*B_i)\X_i*(A_i-B_i/A_i*B_i);


    %global scattering matrix update using Redheffer Star Product
    D = S12/(eye(2)-S11_i*S22);
    F = S21_i/(eye(2)-S22*S11_i);
    S11 = S11 +D*S11_i*S21;
    S12 = D*S12_i;
    S21 = F*S21;
    S22 = S22_i +F*S22*S12_i;


end

%transmission region
kz_trn = sqrt(ur2*er2-kx^2-ky^2);
W_trn = eye(2);
Q_trn = (1/ur2)*[kx*ky, ur2*er2-(kx*kx); ky*ky-ur2*er2, -kx*ky]; %error here
Omega_trn = 1i*kz_trn*eye(2);
V_trn = Q_trn*(Omega_trn^-1);
L_trn = 0;

%scattering matrix for exit medium
A_trn = Wh\W_trn + Vh\V_trn;
B_trn = Wh\W_trn - Vh\V_trn;
S11_trn = B_trn/A_trn;
S12_trn = 0.5*(A_trn-B_trn/A_trn*B_trn);
S21_trn = 2*A_trn^-1;
S22_trn = -A_trn\B_trn;

%update global scattering matrix for exit medium
D = S12/(eye(2)-S11_trn*S22);
F = S21_trn/(eye(2)-S22*S11_trn);
S11 = S11 + D*S11_trn*S21;
S12 = D*S12_trn;
S21 = F*S21;
S22 = S22_trn + F*S22*S12_trn;



kinc = k0*ni*[sin(theta(q))*cos(phi) sin(theta(q))*sin(phi) cos(theta(q))]; %
incident wave vector
```

```matlab
% condition for theta = 0
if theta(q) == 0
    aTE = [0, 1, 0];
else
    aTE = cross(kinc,normal)/norm(cross(kinc,normal)); % TE unit vector
(theta not equal to zero)
end

% polarization
aTM = cross(aTE,kinc)/norm(cross(aTE,kinc)); % TM unit vector, (in plane of
incidence)
P = pte*aTE+ptm*aTM; % polarization vector
%checkP = norm(P) (should be unity)

%source
Exy_inc = [P(1),P(2)]'; % Applied wave
C_inc = W_ref\Exy_inc; %Mode coefficients

%transmitted and reflected fileds
C_ref = S11*C_inc;
C_trn = S21*C_inc;
Exy_ref = W_ref*C_ref;
Exy_trn = W_trn*C_trn;

%longitudinal field components
Ez_ref = -(dot([kx,ky],Exy_ref'))/kz_ref;
Ez_trn = -(dot([kx,ky],Exy_trn'))/kz_trn;


%transmittance and reflectance
E_ref_squared = abs(Exy_ref(1))^2 + abs(Exy_ref(2))^2 + abs(Ez_ref)^2;
E_inc_squared = abs(P(1))^2 + abs(P(2))^2 + abs(P(3))^2;

R = E_ref_squared/E_inc_squared; % reflectance
R_scan(q) = R; % updates reflectance array

E_trn_squared = abs(Exy_trn(1))^2 + abs(Exy_trn(2))^2 + abs(Ez_trn)^2;

T = (E_trn_squared/E_inc_squared)*real((ur1*kz_trn)/(ur2*kz_ref)); %
transmittance
T_scan(q) = T; %updates transmittance array
R+T; % check for conservation of energy
A = 1-abs(R+T);
A_scan(q) = A;
end
 scale = theta/degrees;

%figure depicting reflectance, transmittance and absorption w.r.t. theta
figure(1)
    plot(scale,R_scan,'b',scale,T_scan,'r',scale,A_scan,'k','linewidth',2);
    axis([theta(1)/degrees theta(length(theta))/degrees 0 1.55])
    xlabel('\theta','fontsize',12);
    ylabel('Reflectance(blue) Transmittance(red) Absorption(black)',
'fontsize', 12);
```

```
    title('Transmittance Reflectance and Absorption','fontsize',12)
  fh = figure(1);
  set(fh, 'color', 'white');

data = [theta'/degrees,R_scan',T_scan',A_scan'];

xlswrite('6.22.15_plasmon_demo.xlsx',data,'Transfer Matrix','A')
```
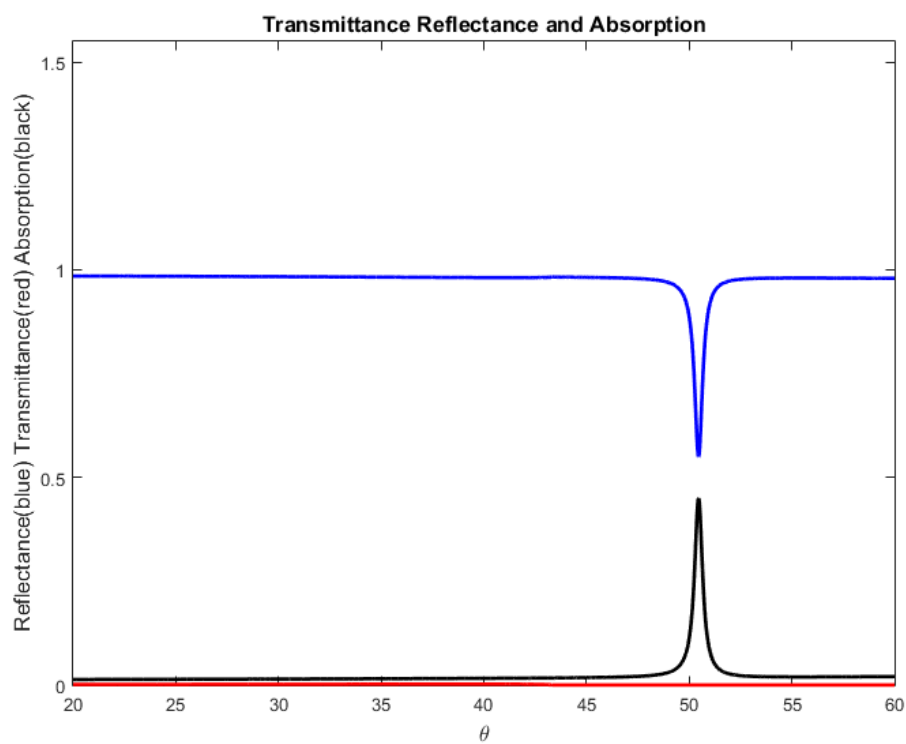

Figure E.1: Theoretical reflectance curve (blue) for scattering matrix MATLAB script

APPENDIX F.   Calculation of reflection response for finite differences in the frequency domain method

```
%Benjamin Hall
% This MATLAB script file implements the FDFD method to model transmission
% and reflection from a grating.
% Based on R.C. Rumpf's CEM Lectures


%-------------------------------------------------------------------------
---------------------------------
% INITIALIZE MATLAB
clc;
clear all;
close all;

%OPEN FIGURE WINDOW
%figure('Color','w');

%UNITS
centimeters = 1;
millimeters = 0.1 * centimeters;
meters      = 100 * centimeters;
degrees     = pi/180;
seconds     = 1;
hertz       = 1/seconds;
gigahertz   = 1e9 * hertz;

% CONSTANTS
c0 = 299792458 * meters/seconds;

%%%%%%%%%%%%%%%%%%%%%%%%%%%%%%%%%%%%%%%%
% DEFINE SIMULATION PARAMETERS
%%%%%%%%%%%%%%%%%%%%%%%%%%%%%%%%%%%%%%%%

% SOURCE PARAMETERS
f0      = 24.0 * gigahertz;                 %operating frequency
lam0    = c0/f0;                            %operating wavelength in fee
space
theta   = 15 * degrees;                     %angle of incidence
MODE    = 'H';                              %electromagnetic mode, 'E' or 'H'
lam0_min = min(lam0);                       %shortest wavelenght in sweep
lam0_max = max(lam0);                       %longest wavelenght in sweep

% GRATING PARAMETERS
fd   = 8.0 * gigahertz;                     %design frequency
lamd = c0/fd;                               %design wavelength
x1   = 0.1040*lamd;                         %width of tooth 1
x2   = 0.0175*lamd;                         %width of slot
x3   = 0.1080*lamd;                         %width of tooth 2
L    = 0.6755*lamd;                         %period of grating
d    = 0.2405*lamd;                         %grating depth
t    = 0.0510*lamd;                         %substrate thickness
```

```
d_array    = [x1,x2,x3,L,d,t];                    %array of structural dimensions
(may need to include t)
er   = 10.0;                                       %dielectric constant of grating
ur   = 1.0;                                        %relative permeability of grating
nr   = real(sqrt(er*ur));                          %refractive index of the grating

%EXTERNAL MATERIALS
er1 = 1.0;                                          %permittivity in the reflection
region
ur1 = 1.0;                                          %permeability in the reflection
region
nref = real(sqrt(er1*ur1));                         %refractive index of
incident/reflection medium
er2 = 1.0;                                          %permittivity in the transmission
region
ur2 = 1.0;                                          %permeability in the transmission
region
ntrn = real(sqrt(er2*ur2));                         %refractive index of
output/transmitted medium

%GRID PARAMETERS
nbuf = 1;
NRES = 40;                                          %grid resolution
NPML = [0 0 20 20 0 0];                             %size of PML at top and bottom of
grid (NYLO and NYHI)
LAMx = L;                                           %size of unit cell in x (grating
period)
LAMy = d + t;                                       %size of unit cell in y

% CALCULATE GRID PARAMETERS
%initial grid resolution
nmax = nr;                                          %maximum refractive index on the
grid
Nlam = 10;                                          %arbitrary starting value of 10
dlam = (lam0_min/nmax)/Nlam;                        %must resolve the minimum
wavelength

dmin = min(d_array);                               %minimum structural dimension
Nd   = 1;                                          %arbitrary value of 1
dd = dmin/Nd;                                       %must resolve minimum structural
dimension

dx = min(dlam,dd);                                 %x-dimension grid resolution
dy = min(dlam,dd);                                 %y-dimension grid resolution
dz = min(dlam,dd);                                 %z-dimension grid resolution
RES = [dx dy dz];                                  %to normalized grid coordinates,
use k0

%SNAP TO CRITICAL DIMENSIONS
%compute the # of cells that compromise the critical dimension
lx = L;                                            %critical dimension in x (by
inspection)
ly = t;                                            %critical dimension in y (by
inspection)
```

```matlab
lz = 0;                                          %critical dimension in z (by
inspection)

Mx = ceil(lx/dx);                                %grid cells needed for lx
My = ceil(ly/dy);                                %grid cells needed for ly
Mz = ceil(lz/dz);                                %grid cells needed for lz

dx = lx/Mx;                                      %adjusts resolution in x
dy = ly/My;                                      %adjusts resolution in y
dz = 0;                                          %adjusts resolution in z

%COMPUTE TOTAL GRID SIZE
%no pml is needed in x for periodic structures
NBUF = ceil(lam0_max/(nbuf*dy)) * [1 1];     %spacer region above and below
grating (convergence will determine the final value)

if rem(ceil(LAMx/dx),2) == 0                     %grid size in x-direction (must
be odd for symmetry of spatial harmonics)
    Nx = ceil(LAMx/dx)+1;
else
    Nx = ceil(LAMx/dx);
end

Ny = ceil(LAMy/dy)+NPML(3)+NPML(4)+NBUF(1)+NBUF(2);   %grid size in y-
direction
Nz = 0;

NGRID = [Nx Ny Nz]; %grid dimension array input to yeeder.m


%COMPUTE WAVE VECTOR TERMS
k0 = 2*pi/lam0;                                   %freespace wavenumber
kinc = k0*nref.*[sin(theta) cos(theta)];         %incident wavevector

m = (-floor(Nx/2):floor(Nx/2))';                 %index array for transverse
wave vector expansion
kxm = zeros(1,length(m));                        %empty array for transverse
wave vectors
kym_ref = zeros(1,length(m));                    %empty array for reflected
longitudinal components
kym_trn = zeros(1,length(m));                    %empty array for transmitted
longitudinal components

for j = 1:length(m)                              % for loop for calculating
wave vector expansions
    kxm(j) = kinc(1) - m(j)*2*pi/LAMx;           %expansion of transverse
wavevectors (result of periodic boundary conditions)
    kym_ref(j) = -sqrt((k0*nref)^2-kxm(j)^2);
    kym_trn(j) = sqrt((k0*ntrn)^2-kxm(j)^2);
end

%introduce the 2x grid
Nx2 = 2*Nx;
dx2 = dx/2;
Ny2 = 2*Ny;
```

```
dy2 = dy/2;
Nz2 = 2*Nz;
dz2 = dz/2;
NGRID2x = [Nx2 Ny2 Nz2]; %grid dimension array input to calcpml3d.m

%BUILD DEVICE (consider dielectric smoothing to improve
%speed)

%additional device geometry in x
nx1 = round(Nx2/2)-round(x2/dx2/2)-round(x1/dx2);
nx2 = nx1+round(x1/dx2)-1;
nx3 = nx2+1;
nx4 = nx2+round(x2/dx2);
nx5 = nx4+1;
nx6 = nx4+round(x3/dx2);

%additional device geometry in y
ny1 = round(Ny2/2)-round(LAMy/dy2);
ny2 = ny1+round(d/dy2)-1;
ny3 = ny2+1;
ny4 = ny2+round(t/dy2);
ny5 = ny4+1;

% device permittivity array
ER2 = er1*ones(Nx2,Ny2); % fill everywhere with er1
ER2(nx1:nx2,ny1:ny2) = er; %add tooth 1
ER2(nx5:nx6,ny1:ny2) = er; %add tooth 2
ER2(:,ny3:ny4) = er; %add substrate
ER2(:,ny5:Ny2) = er2; %fill transmission region

%device permeability array
UR2 = ur1*ones(Nx2,Ny2); % fill everywhere with ur1
UR2(nx1:nx2,ny1:ny2) = ur; %add tooth 1
UR2(nx5:nx6,ny1:ny2) = ur; %add tooth 2
UR2(:,ny3:ny4) = ur; %add substrate
UR2(:,ny5:Ny2) = ur2; %fill transmission region

%boundary conditions
xbc = -2; %should be periodic (-2) requires kinc
ybc = 0; %will include pml
zbc = 0;
BC = [xbc ybc zbc];



%call calcpml3d
[sx,sy,sz] = calcpml3d(NGRID2x,NPML);

%INCORPORATE PML
ERxx = ER2./sx.*sy;
ERyy = ER2.*sx./sy;
ERzz = ER2.*sx.*sy;
URxx = UR2./sx.*sy;
URyy = UR2.*sx./sy;
URzz = UR2.*sx.*sy;
```

```matlab
%OVERLAY MATERIALS ONTO 1X GRID (for 2D currently)
ERxx = ERxx(2:2:Nx2,1:2:Ny2);
ERyy = ERyy(1:2:Nx2,2:2:Ny2);
ERzz = ERzz(1:2:Nx2,1:2:Ny2);               %Ez-mode
URxx = URxx(1:2:Nx2,2:2:Ny2);               %Ez-mode
URyy = URyy(2:2:Nx2,1:2:Ny2);               %Ez-mode
URzz = URzz(2:2:Nx2,2:2:Ny2);


%CONSTRUCT DIAGONAL MATERIALS MATRICES
ERxx = diag(sparse(ERxx(:)));
ERyy = diag(sparse(ERyy(:)));
ERzz = diag(sparse(ERzz(:)));
URxx = diag(sparse(URxx(:)));
URyy = diag(sparse(URyy(:)));
URzz = diag(sparse(URzz(:)));



%CALL YEEDER FUNCTION TO CONSTRUCT DERIVATIVE OPERATORS
[DEX,DEY,DEZ,DHX,DHY,DHZ] = yeeder(NGRID,k0*RES,BC,kinc/k0); %need to write
periodic boundaries


%COMPUTE WAVE MATRIX A
AE = DHX/URyy*DEX + DHY/URxx*DEY + ERzz; %EMode (TM/parallel/p)
AH = DEX/ERyy*DHX + DEY/ERxx*DHY + URzz; %HMode (TE/perpendicular/s)

%COMPUTE THE SOURCE FIELD
%generate X and Y using meshgrid()
[X,Y] = meshgrid((Ny:-1:1),(1:1:Nx));
fsrc1 = exp(1i*(kinc(1)*Y + kinc(2)*X)); %source field; unit amplitude plane
wave; needs to be column vector later
fsrc = reshape(fsrc1,[],1); %column vector source field



%COMPUTE THE SCATTERED-FIELD MASKING MATRIX, Q
scat_rows = NPML(3)+1;        %Number of scattered field rows (1 or 2 greater
than YHI PML)
SF = ones(Nx,scat_rows);
tot_rows = Ny - scat_rows;
TF = zeros(Nx,tot_rows);
Q1 = [SF TF];                 %Scattered-Field Masking Matrix on grid
Q = diag(sparse(Q1(:)));      %Scattered-Field Masking Matrix on diagonal

%COMPUTE THE SOURCE VECTOR, B
bE = (Q*AE - AE*Q)*fsrc;
bH = (Q*AH - AH*Q)*fsrc;
bh = reshape(bH,[Nx,Ny]);


%SOLVE MATRIX EQUATIOIN
fE = AE\bE;
fE = reshape(fE,[Nx,Ny]);


fH = AH\bH;
```

```matlab
fH = reshape(fH,[Nx,Ny]);

%REMOVE THE PHASE TILT


h1 = figure(1);
   set(h1,'Position',[500 100 400 800])
   pcolor(Y,X,real(fH))
   shading interp
   colormap jet
   xlabel('Nx')
   ylabel('Ny')
   zlabel('source')
   %axis([-round(LAMx/2,0) round(LAMx/2,0) 0 LAMy])
   colorbar('eastoutside')
   fH = figure(1);
   grid on

h2 = figure(2);
   set(h2,'Position',[600 100 400 800])
   pcolor(Y,X,real(bh))
   %shading interp
   colormap jet
   xlabel('Nx')
   ylabel('Ny')
   zlabel('source')
   %axis([-round(LAMx/2,0) round(LAMx/2,0) 0 LAMy])
   colorbar('eastoutside')
   fz = figure(2);
   grid on
```

F1. Function for calculating the perfectly matched layer

```matlab
function [sx,sy,sz] = calcpml3d( NGRID,NPML)
%CALCPML3 Calculate the PML parameters on a 2D grid
% [sx,sy,sz] = calcpml3d(NGRID,NPML)
%   This function calcualtes the PML parameters sx and sy to absorb
%   outgoing waves on a 2D grid.

% free space impedence
eta_naught = 376.73;

% reassignment of variables (not efficient)
Nx = NGRID(1);
Ny = NGRID(2);
Nz = NGRID(3);


NXLO = 2*NPML(1); % -x boundary thickness
NXHI = 2*NPML(2); % +x boundary thickness
NYLO = 2*NPML(3); % -y boundary thickness
NYHI = 2*NPML(4); % +y boundary thickness
NZLO = 2*NPML(5); % -z boundary thickness
NZHI = 2*NPML(6); % +z boundary thickness


%initialize pml
```

```
sx = sparse(ones(Nx,Ny));
sy = sparse(ones(Nx,Ny));
sz = sparse(ones(Nx,Ny));

%pml parameters
a_max = 3;
sigma_prime_max = 1;
p = 3;

%for loop for constructing NXLO
if NXLO == 0
    sx;
else
    for nx = 1:NXLO
        ax = 1 + a_max*(nx/NXLO)^p;
        sigma_prime_x = sigma_prime_max*(sin(pi*nx/(2*NXLO)))^2;
        sx(NXLO-nx+1,:) = ax*complex(1,eta_naught*sigma_prime_x);
    end
end

% for loop for construction NXHI
if NXHI == 0
    sx;
else
    for nx = 1:NXHI
        ax = 1 + a_max*(nx/NXHI)^p;
        sigma_prime_x = sigma_prime_max*(sin(pi*nx/(2*NXHI)))^2;
        sx(Nx-NXHI+nx,:) = ax*complex(1,eta_naught*sigma_prime_x);
    end
end

%for loop for constructing NYLO
if NYLO == 0
    sy;
else
    for ny = 1:NYLO
        ay = 1 + a_max*(ny/NYLO)^p;
        sigma_prime_y = sigma_prime_max*(sin(pi*ny/(2*NYLO)))^2;
        sy(:,NYLO-ny+1) = ay*complex(1,eta_naught*sigma_prime_y);
    end
end

% for loop for construction NYHI
if NYHI == 0
    sy;
else
    for ny = 1:NYHI
        ay = 1 + a_max*(ny/NYHI)^p;
        sigma_prime_y = sigma_prime_max*(sin(pi*ny/(2*NYHI)))^2;
        sy(:,Ny-NYHI+ny) = ay*complex(1,eta_naught*sigma_prime_y);
    end
end

%for loop for constructing NZLO
if NZLO == 0
    sz;
```

```matlab
else
    for nz = 1:NZLO
        az = 1 + a_max*(nz/NZLO)^p;
        sigma_prime_z = sigma_prime_max*(sin(pi*nz/(2*NZLO)))^2;
        sz(:,NZLO-nz+1) = az*complex(1,eta_naught*sigma_prime_z);
    end
end

%for loop for constructing NZHI
if NZHI == 0
    sz;
else
    for nz = 1:NZHI
        az = 1 + a_max*(nz/NZHI)^p;
        sigma_prime_z = sigma_prime_max*(sin(pi*nz/(2*NZHI)))^2;
        sz(:,Nz-NZHI+nz) = az*complex(1,eta_naught*sigma_prime_z);
    end
end

end
```

F2. Function for Calculating Derivative Operators on a Yee Grid

```matlab
% Yeeder function
% Based on R.C. Rumpf's CEM lectures
%derivative operators on grid

function [DEX,DEY,DEZ,DHX,DHY,DHZ] = yeeder(NGRID,NRES,BC,kinc)
%yeeder( NGRID,RES,BC,kinc )
Nx = NGRID(1);
Ny = NGRID(2);
Nz = NGRID(3);

dx = NRES(1);
dy = NRES(2);
dz = NRES(3);

xbc = BC(1);
ybc = BC(2);
zbc = BC(3);

LAMx = Nx*dx;
LAMy = Ny*dy;
LAMz = Nz*dz;

xyzdim = prod(nonzeros(NGRID));                  %multiplies nonzero grid
dimensions

if Nz == 0
    xydim = xyzdim;
else
    xydim = xyzdim./Nz;
end
```

```matlab
square = sparse(xyzdim,xyzdim);                    %initialize sparse matrix for
operators
proxy_col = ones(xyzdim,1);                        %column vector of ones
proxy_col_neg = -proxy_col;                        %column vector of negative
ones

neg_identity = spdiags(proxy_col_neg,0,square); %inserts negative ones into
the main diagonal of square

DEX = spdiags(proxy_col,1,neg_identity);       %inserts ones into the first
diagonal of neg_identity to initialize DEX
%FOR LOOP TO APPLY BOUNDARY CONDITIONS TO X
for m = 1:xyzdim
    for n = 1:xyzdim
        if rem(m,Nx)== 0 && rem(n-1,Nx) == 0 && n-m == 1
            if xbc == 0                                        %condition for
Dirichlet
                DEX(m,n) = xbc;
            else
                DEX(m,n) = 0;                                  %application of
periodic
                DEX(m,n-Nx) = exp(1i*kinc(1)*LAMx);
            end
        else
        end

    end
end


DEY = spdiags(proxy_col,Nx,neg_identity);      %inserts ones into the Nxth
diagonal of neg_identity to initialize DEY
%FOR LOOP TO APPLY BOUNDARY CONDITIONS TO y
for m = 1:xyzdim
    for n = 1:xyzdim
        if ybc == 0
            if rem(m-Nx,xydim)== 0 && rem(n-Nx,xydim) == 0 && n-m == 0;
                for g = Nx-1:0
                    DEY(m-g,n-g) = 0;
                end
            else
            end
        else
            if rem(m-Nx,xydim)== 0 && rem(n-Nx,xydim) == 0 && n-m == 0;
                for g = Nx-1:0
                    DEY(m-g,n-g) = 0;
                end
            elseif rem(m,xydim)== 0 && rem(n,xydim) == 0 && n-m == 0;
                for g = 1:Nx
                    DEY(m-Nx+g,n-xydim+g) = exp(1i*kinc(2)*LAMy);
                end
            else
            end
        end
```

```matlab
    end
end

Dimz = spdiags(proxy_col,xydim,neg_identity);   %inserts ones into the
xydimth diagonal of neg_identity to initialize DEZ

DEX = (1./dx).*DEX;
DEY = (1./dy).*DEY;
DEZ = (1./dz).*Dimz;
DHX = -DEX';
DHY = -DEY';
DHZ = -DEZ';
end
```